

## Multi-physical characterization of cellular ceramics for high-temperature applications

Présentée le 7 février 2020

à la Faculté des sciences et techniques de l'ingénieur  
Laboratoire de la science et de l'ingénierie de l'énergie renouvelable  
Programme doctoral en énergie

pour l'obtention du grade de Docteur ès Sciences

par

**Ehsan REZAEI**

Acceptée sur proposition du jury

Prof. K. A. J. Mulleners, présidente du jury  
Prof. S. Haussener, Prof. A. Ortona, directeurs de thèse  
Dr T. Fend, rapporteur  
Prof. P. Colombo, rapporteur  
Prof. J. Botsis, rapporteur





# Acknowledgements

I would like to express my profound gratitude to my advisor Prof. Sophia Haussener, and my co-advisor Prof. Alberto Ortona, for their patience, stimulating discussions, insightful comments, and all the motivation they gave me throughout my Ph.D studies.

I'm also grateful to my colleagues at the Mechanical Engineering and Materials Technology Institute (MEMTI), for all their technical and motivational support and the encouraging atmosphere they have created. I will not forget our morning coffee breaks and all other off-work activities. Individual thanks go especially to my colleagues Giovanni Bianchi and Oscar Santoliquido for their help in the experiments, and to Prof. Maurizio Barbato and his group for the open discussions and sharing their knowledge.

I was lucky to get in contact with great people at the Laboratory of Renewable Energy Science and Engineering (LRESE). I thank my colleagues at LRESE for the fruitful discussions, their support and the great moments we spent together.

A special thanks go to my friends Amin and Sima, for their encouragements throughout my thesis, for the adventures, and for the wonderful memories we had in this period.

Sono fortunato ad avere accanto mia moglie Rowena. Negli ultimi anni, mi hai incoraggiato e mi hai riempito di amore ogni volta che ne avevo bisogno. Grazie per la tua pazienza e il continuo supporto.

وسپاس از خانواده عزیزم؛ از پدر و مادرم، و از مریم و افشین، که با عشق و شکیبایی بی دریغ و بی منت خود، پشتیبان و پناهگاه من  
همیشگی من بوده اند.



# Abstract

Open-cell cellular ceramics are attractive materials for high temperature applications requiring multifunctional capabilities involving: heat absorption, dissipation or insulation, structural load carrying capabilities, fluid flow percolation and enhanced mass transfer. The preferential use of these structures for such purposes is owing to the outstanding characteristics of their substrate material in high-temperatures, namely, their inertness to acidic or base environments, their withstanding in oxidative environments and their relatively high mechanical strength. Given by their porous morphology, they exhibit at the same time high specific surface areas and a percolating fluid phase, making them particularly interesting for applications such as solar receivers, thermal storage systems, heat exchangers, radiant burners and reformers. The recent development of the novel methodologies in additive manufacturing of ceramics has opened new possibilities to directly and indirectly fabricate such ceramics, potentially with tailored morphologies. However, such tailored structures demand new design tools and detailed understanding of their multi-physical transport, mechanic, and oxidation characteristics.

The use of cellular ceramics in enhancing the performance of a high-temperature latent heat thermal energy storage unit was investigated. A detailed design methodology is presented, which consists of a combined analytical-numerical analysis followed by a multi-objective optimization. This optimization indicated that within the selected design space, effectiveness values as large as 0.95 and energy densities as large as  $810 \text{ MJ/m}^3$  could be achieved. Motivated by the results of this study, new porous structures were investigated. As the classical computer aided design tools are not optimized for quick and efficient design of cellular structures with large number of geometrical features, new design approaches were presented: two methods to design structured and unstructured lattices and a Voronoi-based design approach to create structures consisting of different unit-cells combined together.

We then used a combined experimental-numerical approach to investigate the effect of the cell morphology on the heat and mass transport behavior of the porous structures. Different morphologies, namely tetrakaidecahedron, Weaire-Phelan, rotated cube and random foam, were investigated. These structures were designed in cylindrical forms, 3D printed and then manufactured in SiSiC via replica technique followed by silicon reactive infiltration. Permeability and Forchheimer coefficients of the structures were experimentally measured by pressure drop tests at room temperature. The volumetric convective heat transfer coefficients were estimated using temperature measurements and fitting a thermal non-equilibrium heat and fluid flow model to these experiments. It was observed that for the same porosity and cell density the cubic lattice and the random foam exhibited lower pressure drops but also lower heat transfer rates. Undesirable manufacturing anomalies such as pore clogging, was observed for tetrakaidecahedron and Weaire-Phelan structures, which led to a tortuosity larger than calculated, causing additional pressure drop.

Finally, the mechanical and degradation behavior of five SiSiC cellular structures, namely simple cube, rotated cube, tetrakaidecahedron, modified octet-truss and random foam, was experimentally investigated in early stage oxidation conditions at 1400 °C. The samples were oxidized in two different environments: in a radiant burner and inside an electric furnace. The results revealed different mechanisms, namely silicon alloy bead formation and H<sub>2</sub>O/CO<sub>2</sub>-based corrosion, simultaneously degrading the specimens. It is shown that different lattice architectures led to different oxidation behavior on the struts resulting from the changing gas flow paths inside each ceramic architecture.

The effect of the morphology on the elastic behavior of lattice structures was studied in more detail by adapting a numerical approach consisting of a unit-cell model with periodic boundaries. The elastic anisotropies of the lattices were explored by calculating the elastic modulus in different directions. The results revealed that all the studied lattices, and in particular the cubic lattice, have an anisotropic elastic behavior. A new strategy is presented to obtain unit-cells with high elastic modulus and controlled anisotropy.

The studies conducted in this thesis address questions regarding the lattice design, their applications and multi-physical characterization. The mechanical and transport effective properties obtained here, are essential for multi-physics models of processes involving thermal, mechanical and fluid flow within the lattice structures. For a certain application, the choice of the morphology is a trade-off between factors of potential importance such as heat transfer rate, mechanical properties and pressure drop. The design methodology presented for the high-temperature foam-enhanced latent heat thermal energy storage was an example of such processes, demonstrating the tradeoff between heat transfer rate and pressure gradients within the porous medium. The oxidation tests performed here provide essential

understanding of the behavior of cellular ceramic and in particular SiSiC structure in elevated temperatures. They demonstrate the limiting oxidation mechanisms for the use of SiSiC structures and the effect of cell morphology on initiation of oxidation on single struts.

**Keywords:** Cellular ceramics, SiSiC foams, Additive manufacturing, Latent heat thermal energy storage, Design guideline, Lattice design, High temperature oxidation, Convective heat transfer, Pressure drop, Cell morphology, Elastic anisotropy, Elastic modulus, Unit-cell.



# Sommario

I materiali ceramici porosi a celle aperte sono di particolare interesse per applicazioni ad alta temperatura in cui sono richieste caratteristiche multifunzionali tra cui assorbimento di calore, dissipazione o isolamento, capacità di carico strutturale, percolazione del flusso di fluido ed un miglioramento del trasferimento di massa. L'uso preferenziale di queste strutture per tali scopi è dovuto alle eccezionali proprietà ad alta temperatura del materiale di cui sono costituite. In particolare, l'inerzia chimica in ambienti acidi o basici, la resistenza in ambienti ossidativi e la resistenza meccanica relativamente alta costituiscono le principali caratteristiche che rendono questa tipologia di materiali molto attrattiva. Grazie alla morfologia porosa, esse esibiscono allo stesso tempo un'alta area superficiale e una fase fluida percolante, rendendo queste strutture particolarmente interessanti per applicazioni come ricevitori solari, sistemi di stoccaggio termico, scambiatori di calore, bruciatori radianti e *reformers*. Il recente sviluppo delle metodologie per la manifattura additiva di componenti ceramici ha aperto nuove possibilità per la fabbricazione diretta e indiretta di tali componenti, potenzialmente con morfologie appositamente progettate secondo lo scopo finale. Tuttavia, tali strutture complesse richiedono lo sviluppo di nuovi strumenti per il design e la progettazione, abbinati a una comprensione approfondita delle loro caratteristiche di trasporto multi-fisico, delle proprietà meccaniche e dei meccanismi di ossidazione.

Nel presente lavoro, è stato studiato l'impiego di strutture ceramiche cellulari per il miglioramento di un'unità di accumulo di calore termico latente ad alta temperatura. Viene presentata una metodologia di progettazione dettagliata che consiste in un'analisi combinata analitico-numerica seguita da un'ottimizzazione multi-obiettivo. Il risultato dell'ottimizzazione indica che all'interno dello spazio di design selezionato possono essere raggiunti valori di efficacia di 0.95 e densità di energia pari a  $810 \text{ MJ/m}^3$ . Motivati dai risultati promettenti di questo studio, sono state proposte ed analizzate nuove strutture porose. Poiché i classici strumenti di progettazione assistita dal computer non sono ottimizzati per la progettazione rapida ed efficiente di strutture cellulari con un gran numero di complicazioni

geometriche, sono stati sviluppati nuovi approcci progettuali, consistenti in due metodi per generare reticoli strutturati e non, oltre ad un metodo basato sulla tassellazione di Voronoi, per creare strutture composte da differenti celle unitarie combinate.

È stato poi utilizzato un approccio combinato sperimentale-numerico per studiare l'effetto della morfologia delle celle sul comportamento di trasporto di calore e di massa delle strutture porose. Sono state studiate diverse morfologie, in particolare il tetrakaidecaedro, il Weaire-Phelan, il cubo ruotato e la schiuma casuale. Queste strutture sono state progettate con una forma cilindrica, stampate in 3D ed infine prodotte in SiSiC tramite tecnica di replica seguita da infiltrazione reattiva al silicio. I coefficienti di permeabilità e di Forchheimer delle strutture sono stati misurati sperimentalmente mediante prove di caduta di pressione a temperatura ambiente. I coefficienti volumetrici di scambio termico convettivo sono stati stimati utilizzando le misurazioni di temperatura ed approssimando questi punti sperimentali con un modello fluidodinamico e termico di non-equilibrio. È stato osservato che, a parità di porosità e densità cellulare, il reticolo cubico e la schiuma casuale portano a una minore caduta di pressione ma anche a minori velocità di trasferimento di calore. Alcuni difetti di fabbricazione come l'occlusione dei pori sono stati osservati per le strutture tetrakaidecaedro e Weaire-Phelan, portando ad una tortuosità superiore a quella calcolata e causando un ulteriore calo di pressione.

Infine, il comportamento meccanico e di degradazione di cinque strutture cellulari SiSiC, ossia cubo semplice, cubo ruotato, tetrakaidecaedro, otteetto modificato e schiuma casuale, è stato studiato sperimentalmente in condizioni di ossidazione nella fase iniziale a 1400 °C. I campioni sono stati ossidati in due ambienti diversi: in un bruciatore radiante e all'interno di un forno elettrico. Ossidando simultaneamente i provini, sono stati osservati diversi meccanismi di degradazione, in particolare la formazione di gocce di lega di silicio sulla superficie e la corrosione causata dalla presenza di  $H_2O/CO_2$ . È stato dimostrato che diverse architetture reticolari hanno portato ad un differente comportamento di ossidazione sugli *struts* a causa del diverso percorso del flusso di gas all'interno delle strutture ceramiche.

L'effetto della morfologia sul comportamento elastico delle strutture reticolari è stato studiato in modo più dettagliato adattando un approccio numerico costituito da un modello basato su una cella unitaria con condizioni al contorno periodiche. Le anisotropie elastiche dei reticoli sono state investigate calcolando il modulo di Young in diverse direzioni. I risultati hanno rivelato che tutti i reticoli studiati, ed in maggior misura il reticolo cubico, hanno un comportamento elastico anisotropico. Da questo risultato è stata poi presentata una nuova strategia per ottenere celle unitarie con alto modulo elastico ed anisotropia controllata.

Gli studi condotti nella tesi riguardano questioni legate alla progettazione di reticoli, le loro applicazioni e la caratterizzazione multi-fisica. Le proprietà meccaniche e di trasporto effettive



ottenute sono essenziali per la modellazione di processi che coinvolgono il flusso termico, le caratteristiche meccaniche ed il flusso fluido all'interno delle strutture reticolari. Per una determinata applicazione, la scelta della morfologia è un compromesso tra fattori come la velocità di trasferimento del calore, le proprietà meccaniche e la caduta di pressione. La metodologia di progettazione presentata per l'accumulo di energia termica latente ad alta temperatura mediante una struttura ceramica è un esempio di tale processo, dimostrando il compromesso ottenuto tra velocità di trasferimento di calore e gradienti di pressione all'interno del mezzo poroso. I test di ossidazione eseguiti forniscono una comprensione essenziale del comportamento di strutture ceramiche cellulari, nello specifico reticoli in SiSiC a temperature elevate. Questo ha comprovato i meccanismi di ossidazione che limitano l'uso delle strutture SiSiC e l'effetto della morfologia cellulare all'iniziazione dell'ossidazione sui singoli *struts*.

**Parole chiave:** Ceramica cellulare, schiume SiSiC, manifattura additiva, accumulo di energia termica latente, linee guida progettuali, design di reticoli, ossidazione ad alta temperatura, trasferimento di calore convettivo, caduta di pressione, morfologia cellulare, anisotropia elastica, modulo elastico, cella unitaria.



# Table of Contents

<b>Acknowledgements</b>	<b>i</b>
<b>Abstract</b>	<b>iii</b>
<b>Table of Contents</b>	<b>xi</b>
<b>List of Figures</b>	<b>xv</b>
<b>List of Tables</b>	<b>xxi</b>
<b>List of Symbols</b>	<b>xxiii</b>
<b>1 Introduction</b>	<b>1</b>
<b>2 Design and optimization of a high-temperature latent heat storage unit</b>	<b>11</b>
2.1 Introduction	11
2.2 LHTES unit presentation and performance metrics	12
2.2.1 Configuration and materials	12
2.2.2 Performance metrics	13
2.3 Modeling and design approach	15
2.3.1 General assumptions	17
2.3.2 Preliminary analytical calculations	18
2.3.3 Axis-symmetric FE model	19
2.3.4 Design of experiments and optimization	23
2.4 Results and discussion	24
2.4.1 FEM results	24
2.4.2 Polynomial meta-model	29

## Table of Contents

---

2.4.3 Optimization	30
2.5 Conclusions	34
2.6 References	36
<b>3 Geometric design of cellular solids</b>	<b>39</b>
3.1 Introduction	39
3.2 Structured lattice design	40
3.3 Unstructured lattice design	42
3.4 Voronoi-based design	45
3.5 Conclusions	49
3.6 References	50
<b>4 Characterization of pressure drop and convective heat transfer</b>	<b>53</b>
4.1 Introduction	53
4.2 Samples and the experimental set-up	55
4.2.1 Fabrication and characterization of the porous specimens	55
4.2.2 Experimental set-up	58
4.3 Calculation procedure	59
4.3.1 Pressure drops coefficients	59
4.3.2 Volumetric heat transfer coefficients	60
4.3.3 Computational heat transfer and fluid flow model	60
4.3.4 Numerical procedure	61
4.3.5 Uncertainty analysis	64
4.4 Results and discussion	65
4.4.1 Measured pressure drop	65
4.4.2 Literature comparison for pressure drop	68
4.4.3 Predicted convective heat transfer coefficients	70
4.4.4 Literature comparison for heat transfer	72
4.5 Conclusions	75
4.6 References	76
<b>5 Early-stage oxidation</b>	<b>81</b>

5.1 Introduction	81
5.2 Experimental procedure	83
5.2.1 Material and sample preparation	83
5.2.2 Oxidation tests and characterization	84
5.3 Results and discussion	87
5.3.1 Oxidation behavior	87
5.3.2 Mechanical strength	92
5.4 Conclusions	94
5.5 References	95
<b>6 Anisotropic elastic properties</b>	<b>99</b>
6.1 Introduction	99
6.2 Methodology for the mechanical Characterization	101
6.2.1 Periodic boundary conditions	101
6.2.2 Unit-cells and the methodology	103
6.3 Results and discussion	106
6.3.1 Numerical calculations of the elastic constants	106
6.3.2 Directional dependency of the elastic constants	109
6.4 Conclusions	115
6.5 Reference	117
6.6 Appendix	120
<b>7 Conclusions and prospects</b>	<b>123</b>
<b>Curriculum Vitae</b>	<b>129</b>



# List of Figures

Figure 2.1. The parallel assembly of the LHTES system and a single unit (right). The red cylinder is the encapsulation containing the PCM, which is surrounded by the porous medium displayed in gray color. ....	13
Figure 2.2. Flow diagram of the approach used for the design and optimization of the LHTES unit. ....	16
Figure 2.3. The axis-symmetric model domain of the LHTES unit and corresponding boundary conditions. ....	17
Figure 2.4. Flow chart of the analytical model calculations in order to obtain $u_{in}$ and $A_{fc}$ that were then fed to the FE model. ....	19
Figure 2.5. Total effectiveness of an LHTES units with empty flow channels (without porous medium) for different encapsulation sizes. The black dots are the simulated points; the contours were linearly interpolated. ....	24
Figure 2.6. Constant solid temperature contour at $T_s = 1219$ K for different time steps and for different $d_{enc}$ until the outlet temperature fell below $T_{stop} = 1209$ K. The mass flow rate and the flow channel thickness are calculated in the preliminary analytical calculations as a function of the design factors ( $d_{enc}$ , $L_{enc}$ , $d_p$ ) for each model. The PCM domain is on the left side of each case, the porous media filled domain is to the right side. For these five cases, $L_{enc}$ and $d_p$ are constant and equal to 1000 mm and 5 mm, respectively. ....	25
Figure 2.7. The HTF outlet temperature (blue) and the solid fraction of the PCM (orange) plotted versus time for one typical example ( $d_{enc} = 20$ mm, $L_{enc} = 1000$ mm and $d_p = 5$ mm). ....	26

## List of Figures

---

Figure 2.8. From left to right: the sensible, latent and the total effectiveness for the LHTES units for different encapsulation sizes with $d_p = 2.5$ mm. The black dots are the simulated points, the contours were linearly interpolated. ....	27
Figure 2.9. The packing factor for all simulated LHTES units. The blue, green and red zones, respectively, show the results for $d_p = 1.25, 2.5$ and $5$ mm. ....	28
Figure 2.10. The energy density for LHTES units with varying $d_{enc}$ and $L_{enc}$ at constant $d_p = 2.5$ mm. The black dots are the simulated points, the contours were linearly interpolated. ....	28
Figure 2.11. Pareto frontier (red line), numerical data points obtained by the FE model (colored circles) and calculated points from the regression model utilizing the meta-models (black dots). The predicted optimization points for case 1* and 2 are shown in filled black squares. ....	31
Figure 2.12. The overlay contour plots for a) $d_p = 1.25$ mm, b) $d_p = 2.5$ mm, and c) $d_p = 5$ mm. The isolines of total effectiveness are shown in solid lines and the isolines of the energy density $[MJ/m^3]$ in dashed lines. ....	33
Figure 3.1. (a) Tetrakaidecahedron with open struts at the boundary, (b) Tetrakaidecahedron, (c) Weaire-Phelan and (d) rotated cubic lattice with closed struts at the boundary. In the picture, the cells are filled with yellow spheres for better visibility of the structure. ....	41
Figure 3.2. Unit cells with cubic symmetry: cube, body centered cube, octet-truss and tetrakaidecahedron. ....	43
Figure 3.3. From left to right: hexahedral mesh with a radial growth rate of 1.5, used as the input for the code, generated CAD model with octet-truss unit-cells, and generated CAD model with tetrakaidecahedron unit-cells. ....	43
Figure 3.4. 3D unstructured lattices in the form of an airfoil and variable cell sizes with (a) cubic, (b) tetrakaidecahedron and (c) octet-truss unit-cells. (d) Isometric view of the CAD model of the airfoil with cubic unit-cells and variable strut diameters. ....	44
Figure 3.5. 2D representation of the generation of a Voronoi from different input seed points. From left to right: random, quad, hexagonal and rotated quad lattices. ....	45
Figure 3.6. 2D representation of a multi-lattice structure consisting of random Voronoi, quad, hexagonal and rotated quad cells. ....	46
Figure 3.7. Different views of a Voronoi-based structure as a combination of hexahedral, cubic, rotated cube and random cells (shown in red) attached to a hexahedral honeycomb. ....	47
Figure 3.8. The Grasshopper flowchart for creating multi-lattice structures. ....	48



Figure 4.1. Front and top view of cylindrically shaped SiSiC structures (diameter of 20 mm and length of 100 mm). From left to right: RC, TK, WPh lattices, and random foam. The presence of closed cell walls were observed in the manufactured samples, especially in the TK and WPh. Some of these closed cell walls are shown in the magnified section. An example of the closed cells in these two lattices are shown with the red circles in the magnified section. ....	57
Figure 4.2. Scheme of the test set-up for measurements of pressure drop and convective heat transfer. The cylindrical porous samples are embedded in a cylindrical tube, which is heated in the temperature-controlled electric furnace. The pressure drop sensors (purple lines), the thermocouples placed on the solid parts (blue lines), and the thermocouples to measure the air stream inlet and outlet temperatures (red lines) are shown. The magnified region shows the two U-shaped heating elements that are placed around the tube, and the thermocouples used to measure the temperature of the air stream and the porous specimens, which are placed inside the tube. ....	59
Figure 4.3. Schematic of the numerical domain used when solving the coupled Eqs 4.4 and 4.5. The red rectangle shows the submodel used for the determination of the volumetric convective heat transfer coefficients. The inlet boundary condition of the submodel (red surface) is obtained from the global model solution. ....	64
Figure 4.4. Measured pressure drops per length for the four specimens for 10 different velocities, corresponding to Re in the range of 40 to 940. The regression lines are obtained only using the data points with $Re < 250$ . ....	67
Figure 4.5. Measured dimensionless pressure gradient as a function of Reynolds number. The error bar indicates the calculated uncertainty of each data point. The black and red dotted-lines, respectively, represent the best line fits for mean and their standard errors. ....	67
Figure 4.6. Comparison of our experimental friction factor of WPh and TK lattices with the numerical results in the literature. The values of Wu et al. were obtained by extrapolation of their results for a TK lattice with $d_c = 4.75$ mm. ....	69
Figure 4.7. Comparison of experimental (points) and the numerical (lines) air temperatures at the porous sample outlet for a RC sample at three different velocities. Gravitational force is in the direction from right to left. ....	71
Figure 4.8. The predicted Nusselt number as a function of Reynolds number for the porous specimens. The uncertainty of the results, calculated according to Eq. 12, is indicated with error bars. ....	71
Figure 4.9. (a) Comparison of the predicted Nusselt values for the foam in the present study with correlations listed in Table 4.5. All correlations are plotted for a 5 PPI foam with $\phi =$	

## List of Figures

---

0.843. (b) Comparison between the Nusselt values of the numerical results from the literature with the values obtained in the current study for TK and WPh. ....	74
Figure 5.1. Front view of the five SiSiC lattices produced by replica technique.....	84
Figure 5.2. Schematic representation of the test set up with the porous burner and three cubic samples placed on it.....	85
Figure 5.3. XRD analysis of a pulverized strut from cubic lattice after thermal tests of group I, showing the formation of cristobalite and tridymite. ....	87
Figure 5.4. (a) Rotated cubic sample of group I after thermal oxidation. The cavities inside the struts oxidized in a lower oxygen partial pressure. That can result in formation of silica whiskers (white features). An exuded silicon alloy bead is also evident inside the strut. (b) Silicon alloy bead on the surface of a cubic lattice belonging to group I. White features correspond to heavier elements (Fe, Cr). In the dashed areas, beads coalescing in larger ones. ....	88
Figure 5.5. Five different lattices of group II after thermal tests in porous burner. The dashed lines mark out the surface at the maximum temperature 1400°C. ....	89
Figure 5.6. (a) A strut of octet samples of group II after tests. The topside of the strut is the windward side, which had a thicker silica scale. Silicon depleted regions are shown in the dashed rectangle. (b) SEM image of the surface (the hot zone) of octet specimen of group II after the tests. The swelled region corresponds to an exuded bead after severe oxidation. A cross section of it can be seen also in the rectangle in (a). (c) Bubble and craters formed in process of silica formation. Craters are filled with silica after the gas explosion. The silica surface is full of cracks made in thermal cycles due to large difference of its thermal expansion with substrate. (d) Formation of two stripes of silica on a strut of a cubic sample of group II. The white arrow shows the gas flow direction.....	90
Figure 5.7. XRD analysis of a pulverized strut of a cubic lattice in group II. ....	91
Figure 5.8. Schematic representation of the mechanism of formation of silica on a single strut. (a) The very first SiO <sub>2</sub> points are formed in stagnation point of the flow. (b) The layer grows in both directions on the strut along the flow stream. (c) and (d) The gradual growth is much faster along the gas flow.....	92
Figure 5.9. Stress-strain curves for three lattices with cubic structures from each of the three groups. Under compression loading, the struts were gradually breaking until the final catastrophic failure of the samples. ....	93
Figure 5.10. Compression test results of three sets of lattices before and after thermal tests. The maximum, minimum and the average values are displayed for lattices in each group. While	

strength values of group II specimens did not differ from the as-produced ones, samples of group I showed a decreased retained strength. ....	94
Figure 6.1. Examples of simple polyhedral cells. The polygons that can form stretching-dominated structures are labeled with yes [7]. ....	100
Figure 6.2. (a) simple cube, (b) tetrakaidecahedron, (c) octet-truss and (d) modified octet-truss unit-cells used in this study. ....	103
Figure 6.3. Variation of the strut diameter and the specific surface area for the studied unit-cells. ....	106
Figure 6.4. The normalized stresses and deformations (with a scale factor of 70) of the octet-truss unit-cell with a porosity of 0.9 for the two cases: (a) pure tensile in $z$ -direction, and (b) pure shear in $y$ -direction. ....	107
Figure 6.5. Calculated effective elastic moduli for the four unit-cells as a function of solid volume fraction. For the modified octet-truss, two values in different directions are reported due to its tetragonal symmetry. ....	108
Figure 6.6. Calculated shear moduli and Poisson's ratio for the four unit-cells as a function of solid volume fraction. For the modified octet-truss, two values in different directions are reported due to its tetragonal symmetry. ....	108
Figure 6.7. Directional dependence of the effective elastic modulus for (a) cubic, (b) tetrakaidecahedron, (c) octet-truss and (d) for lattices, all with 0.9 porosity. ....	110
Figure 6.8. Directional dependence of the effective elastic modulus for the cubic unit-cells with (a) 0.95, (b) 0.9, (c) 0.85, (d) 0.8, (e) 0.75 and (f) 0.7 porosities. ....	111
Figure 6.9. The COTC unit-cell created based on assembling a simple cubic structure with the octet-truss unit-cell. ....	112
Figure 6.10. Directional surface plot of the effective elastic modulus for the COTC unit-cell with a porosity of 0.9 and (a) $d_{\text{cube}}/d_{\text{octet}} = 1$ , (b) $d_{\text{cube}}/d_{\text{octet}} = 1.5$ and, (c) $d_{\text{cube}}/d_{\text{octet}} = 2$ . ....	113
Figure 6.11. Directional dependence of the effective elastic modulus for the COTC unit-cells with $d_{\text{cube}}/d_{\text{octet}} = 1.208$ , and a porosity of (a) 0.95, (b) 0.9, (c) 0.85, (d) 0.8, (e) 0.75 and (f) 0.7. ....	113
Figure 6.12. Left: the effective elastic moduli for all the analyzed unit-cells in this work. Right: the Zener anisotropy ratio for all the unit-cells with cubic symmetry. ....	114
Figure 6.13. The example used for the figures in this section. A tube filled with porous media, radiated on the top and with a cold fluid flowing within the porous domain. The porous	

## List of Figures

---

medium has a simple representative unit-cell, which is a cube with a spherical void in the middle. ....120

Figure 6.14. Flowchart of the proposed procedure for coupling fluid flow, heat transfer and solid mechanics and creation of a submodel in the zone of interest. ....121

Figure 6.15. (a) Temperature distribution obtained from the continuum thermo-fluid model, (b) the temperature distribution mapped on the discrete model, (c) the deformations obtained from the continuum stress model and, (d and f) the stress results from the discrete submodel on the red surface at the end of the tube. ....122

## List of Tables

Table 2.1. Thermodynamic characteristics of the materials used for this study. ....	13
Table 2.2. Correlations used to calculate the convective heat transfer and mass transport, and radiative transport parameters.....	21
Table 2.3. The parameters used in the analytical and numerical models.....	21
Table 2.4. Design variables and their values used in the parametric study. ....	24
Table 2.5. $R^2$ value and adequacy parameters for the calculated regression models. ....	30
Table 2.6. Mathematical representation of the optimization cases and their results.....	32
Table 2.7. Validation of the optimization results and the comparison with simulations.....	32
Table 4.1. Microstructural properties of the four investigated specimens.....	56
Table 4.2. Permeability and form coefficients and their uncertainties for the four porous specimens. ....	66
Table 4.3. Permeability and form coefficients reported in literature for 5 PPI foams with different porosities .....	68
Table 4.4. Coefficients of the proposed Nusselt correlations (Eq. 4.33) for each of the samples with $R^2$ values of the fitting. The correlations are valid for $70 < Re < 250$ .....	72
Table 4.5. Literature correlations based on experimental studies of foams with various porosities and pore densities. ....	73
Table 5.1. Produced specimens and their distribution into three test groups.....	85
Table 5.2. Thermal tests of each of the three groups of specimens. ....	86

## List of Tables

---

Table 6.1. Macroscopic strain cases used for determination of the elastic properties. ....	104
Table 6.2. Calculated regression models for the effective elastic modulus of the lattices in the principal directions.....	109
Table 6.3. Calculated regression models for the effective shear modulus of the lattices in the principal directions.....	109

# List of Symbols

## Latin symbols

$A$	area	$[m^2]$
$C$	form coefficient	$[m^{-1}]$
$\mathbf{C}$	stiffness matrix	$[Pa]$
$c_p$	specific heat capacity	$[J.kg^{-1}.K^{-1}]$
$D$	desirability function	$[-]$
$d$	diameter	$[m]$
$e$	specific exergy	$[J.m^{-3}]$
$E$	elastic modulus	$[Pa]$
$f$	friction factor	$[-]$
$G$	incident radiation	$[W.m^2]$
$G$	shear modulus	$[Pa]$
$g$	gravity constant	$[m.s^{-2}]$
$h$	specific enthalpy	$[J.m^{-3}]$
$h_{sf}$	interfacial heat transfer coefficient	$[W.m^{-2}.K^{-1}]$
$h_v$	volumetric convective heat transfer coefficient	$[W.m^{-3}.K^{-1}]$
$I$	radiation intensity traveling in a certain direction	$[W.m^{-2}.sr^{-1}]$
$I_b$	Blackbody radiative intensity	$[W.m^{-2}.sr^{-1}]$
$K$	permeability coefficient	$[m^2]$
$L$	sample length	$[m]$
$m$	mass	$[kg]$
$\dot{m}$	mass flow rate	$[kg.s^{-1}]$
$p$	pressure	$[Pa]$

## List of Symbols

---

<b>q</b>	heat flux	[W.m <sup>-2</sup> ]
$r_i$	importance factor	[-]
$S$	sensitivity	[-]
<b>S</b>	compliance matrix	[Pa <sup>-1</sup> ]
$S_v$	specific surface area	[m <sup>-1</sup> ]
$T$	temperature	[K]
$t$	time	[s]
$U$	internal energy	[J.kg <sup>-1</sup> ]
$u$	displacement	[m]
$u$	superficial velocity	[m.s <sup>-1</sup> ]
$w$	energy density	[J.m <sup>-3</sup> ]
$w_i$	weight factor	[-]
<b>x, y, z</b>	Cartesian coordinate directions	[m]
<b>r, z</b>	Cylindrical coordinate system	[m]

## Greek symbols

$\alpha$	scattering albedo	[-]
$\alpha_m$	mass fraction	[-]
$\beta$	extinction coefficient	[m <sup>-1</sup> ]
$\delta$	thickness	[m]
$\epsilon$	effectiveness	[-]
$\epsilon$	strain	[-]
$\eta$	efficiency	[-]
$\theta$	phase fraction	[-]
$\kappa$	absorption coefficient	[m <sup>-1</sup> ]
$\lambda$	thermal conductivity	[W.m <sup>-1</sup> .K <sup>-1</sup> ]
$\mu$	dynamic viscosity	[Pa.s]
$\nu$	Poisson's ratio	[-]
$\xi$	exergy	[J]
$\rho$	density	[kg.m <sup>-3</sup> ]
$\sigma$	stress	[Pa]
$\sigma$	uncertainty	[-]
$\phi$	porosity	[-]



### Subscripts

b	black
c	cell
des	desired
dis	discharging
enc	encapsulation
exp	experimental
f	fluid
fc	flow channel
h	hydraulic
in	inlet
init	initial
l	liquid
lat	latent
num	numerical
m	median
out	outlet
p	pore
s	solid
st	strut
su	storage unit
w	window

### Acronyms

CAD	computer-aided design
CVD	chemical vapor deposition
FE	finite element
HTF	heat transfer fluid
LHTES	latent heat thermal energy storage
LTNE	local thermal non-equilibrium
PCM	phase changing material
PF	packing factor
Pr	Prandtl number
PPI	pores per inch
RC	rotated-cube

## List of Symbols

---

RPC	reticulated porous material
RUC	representative unit-cell
SEM	scanning electron microscopy
SiSiC	silicon-infiltrated silicon carbide
TK	tetrakaidecahedron
WPh	Weaire-Phelan
XRD	X-ray diffraction
EDS	Energy-dispersive spectroscopy

### Definitions

$f_{DW} = \frac{\Delta p}{L} \cdot \frac{2 d_c}{\rho_f u_f^2}$	Darcy–Weisbach friction factor
$Nu_v = \frac{h_v d_c^2}{\lambda_f}$	Mean Nusselt number
$\Pi = \frac{\Delta p}{L} \cdot \frac{d_c^2}{\mu_f u_f}$	Dimensionless pressure gradient
$Re = \frac{\rho_f u_f d_c}{\mu_f}$	Reynolds number
$Re_{pipe} = \frac{\rho_f u_f d_{pipe}}{\mu_f}$	Reynolds number in the pipe

# 1 Introduction

Open-cell cellular structures are assemblies of edges (called struts) and faces that form individual cells connected together through open faces. They naturally exist in different forms such as marine sponges and cancellous bones [1]. Mimicking nature, polymeric, metallic and ceramic foams have been industrially produced by different methods. Among the three classes, ceramic foams are the first choice for high-temperature applications that require multifunctional capabilities such as: heat absorption, insulation or dissipation, structural load bearing, fluid flow percolation and enhanced mass transfer. The use of these structures for such applications is a result of their outstanding properties in elevated temperatures, such as withstanding harsh environments (acidic, base or oxidative), and their superior mechanical properties (modulus, hardness, strength). Additionally, due to their porous nature, they exhibit high specific surface area and a percolating fluid phase, making them particularly interesting for applications such as solar receivers, thermal storage systems, heat exchangers, radiant burners and reformers [2]–[4].

Ceramic foams are traditionally manufactured by methods such as fugitive pore forming, direct foaming, and replication of polymeric or natural foams [5], [6]. In the literature, there is a large amount of work published on the characterization of cellular materials. Different studies have been conducted particularly on the characterization of ceramic foams. Most of these studies are experimental and focus on porosity and pore density characterization of foams manufactured by traditional replication methods. Gibson and Ashby [7] presented one of the first detailed reviews on the behavior of the cellular solids suggesting simple correlations for prediction of the effective mechanical and thermal properties of the solid foams as a function of their relative density. These material-independent correlations gave predictions for ceramic foams as well, for which there were fewer data [8]. Further experimental studies were later carried out on the mechanical behavior of ceramic foams,

reporting their effective elastic properties and fracture mechanisms [9]–[12]. The pressure-drop within the ceramic foams has also been well studied due to the simplicity and low cost of the measurement procedure [13]–[16]. A review of the correlations reported in the literature is published by Edouard et al. [17]. The heat transfer from the solid to the fluid passing through the foam is often characterized by convective heat transfer coefficient, which is commonly calculated in a combined numerical-experimental approach [18]. Several correlations are proposed based on foams with different porosity, cell density and material [19]–[22].

Beside the experimental studies, pore-level numerical analysis of the foams is also essential for better understanding of their behavior. However, this analysis is a difficult task due to the complex geometry of these structures. Several studies have considered unit-cells such as tetrakaidecahedron and Weaire-Phelan as the representative geometry of the foam, reporting pressure-drop characteristics [23], conductive [24] and convective heat transfer coefficients [23], and mechanical properties (elastic modulus, strength and fracture toughness) [25], [26]. In practice the shape of the structure can change due to manufacturing anomalies, or the constraints of the manufacturing technique. Advances in computational power have also allowed numerical characterization of porous structures utilizing their exact microstructures (obtained, for example, by computed tomography and subsequent digitalization through various segmentation approaches) in pore-level simulations [27], [28].

Recent developments in additive manufacturing of ceramics have enabled the production of pieces with tailored micro-scale geometrical features. Several groups are developing additive manufacturing methods for ceramics with micro-scale details such as: vat polymerization, powder bed fusion and binder jetting [29]–[32]. Detailed discussion of the advantages and disadvantages of these methods can be found in review articles [33], [34]. These techniques can be directly and indirectly used to produce customized cellular ceramics with tailored morphologies. As a result, researchers have been working on manufacturing and characterization of ceramic structures with repetitive unit-cells. Compared to traditional random foams, lattice structures are reproducible and offer more design parameters, which can result in structures with enhanced properties and novel functionalities. While there is a large body of literature on the behavior of ceramic random foams, there are fewer studies on lattices. Perhaps the most important analytical work on mechanical properties of lattices has been conducted by Deshpande et al. [35]. They classified the cellular solids in two groups, namely, stretching-dominated structure, which deform by uniaxial tension or compression of their struts, and bending-dominated structures (such as random foams), which deform by bending of their struts. It was demonstrated that stretching-dominated structures possess superior mechanical properties. These analytical studies, while being informative, are limited to highly porous structures, where the struts can be assumed as slender beams. Apart from

the numerical studies, mentioned earlier, that consider lattices as a representative model for the foams [23]–[26], there are other numerical as well as experimental investigations, mainly focused on development of the manufacturing techniques, mechanical behavior and permeability of different lattices [36]–[41].

This thesis aims at a comprehensive investigation on ceramic structures with a focus on their generation, characterization (heat and mass transport, and mechanical properties), and their use in novel applications. The experiments are focused on SiSiC ceramics produced by rapid prototyping and replication process, as described by Ortona et al. [29]. The choice of SiSiC was due to its interesting characteristics at high-temperatures, such as its inertness to acidic or base environments, its ability to withstand oxidative environments and its relatively enhanced mechanical and thermal properties and, consequently, high thermal shock resistance. All these properties make SiSiC an attractive candidate for high-temperature ( $>1000^{\circ}\text{C}$ ) applications involving large thermal fluxes ( $\sim 1000\text{ kW/m}^2$ ) [3]. Currently, SiC-based foams are widely used in different applications. This is due to their well-known behavior, which is reported in several studies [3], [28], [42], [43], [20]. The economic production of lattices enables throughout investigations of their behavior as well. These studies are of great importance as they provide the knowledge on the response of each lattice type, and therefore facilitate the use of ceramic lattices in the potential applications.

In *chapter 2*, as an application of ceramic foams, a medium size high-temperature latent heat thermal energy storage is considered, with porous ceramics as heat transfer enhancing fin structures. The detailed design methodology is described and the results are presented in the form of different system performance metrics. A multi-objective optimization is employed to obtain the optimal sizing of the storage system and the foam morphology.

*Chapter 3* presents alternative approaches to design porous parts with various unit-cell morphologies. Three possible methods are presented with several examples to better illustrate the ideas. These approaches were used to develop the tools used for designing the samples for this thesis as well as some other project [44]–[48].

The pressure-drop and heat transfer rates of porous structures with various unit-cells are studied in *chapter 4*. Four different structures, namely tetrakaidecahedron, Weaire-Phelan and rotated cube lattices and commercial random foam, are considered. The lattices are designed in cylindrical forms, 3D printed and then manufactured in SiSiC via replica technique followed by silicon reactive infiltration. The manufactured specimens had different shapes but similar geometrical parameters (porosity and cell size). An experimental approach is used to obtain the permeability and Forchheimer coefficients. The volumetric convective heat transfer coefficients for different velocities are obtained by a combined experimental-numerical approach.

## Introduction

---

In *chapter 5*, the early stage oxidation behavior of SiSiC cellular ceramics is presented. Five different structures, namely cube, rotated cube, tetrakaidecahedron, modified octet-truss and random foam are studied. The experiments are performed in two different environments in 1400 °C: a porous burner and an electric furnace with stagnant air. After the oxidation tests, SEM imaging and compression tests are used to ascertain integrity of the specimens. This chapter gives an overview on the bounds and limits of the use of SiSiC structures in high temperature oxidative environments and reveals the mechanisms of initiation of oxidation on a single strut.

*Chapter 6* is dedicated to the numerical assessment of the effect of morphology on the mechanical properties of lattice structures. Four different unit-cells, namely cube, tetrakaidecahedron, octet-truss and modified octet-truss are considered. The elastic properties of each lattice are obtained by considering unit-cells with periodic boundary conditions. The isotropy of each unit-cell is discussed and a design strategy is adopted to obtain a unit-cell with enhanced elastic properties and controlled isotropy.

## References

- [1] G. Mayer and M. Sarikaya, “Rigid biological composite materials: Structural examples for biomimetic design,” *Exp. Mech.*, vol. 42, no. 4, pp. 395–403, Dec. 2002.
- [2] T. Fend, “High porosity materials as volumetric receivers for solar energetics,” *Opt Appl*, vol. 11, no. 2, pp. 271–284, 2010.
- [3] S. Gianella, D. Gaia, and A. Ortona, “High Temperature Applications of SiSiC Cellular Ceramics,” *Adv. Eng. Mater.*, vol. 14, no. 12, pp. 1074–1081, 2012.
- [4] Y. S. Montenegro Camacho *et al.*, “Development of a robust and efficient biogas processor for hydrogen production. Part 2: Experimental campaign,” *Int. J. Hydrog. Energy*, vol. 43, no. 1, pp. 161–177, Jan. 2018.
- [5] A. R. Studart, U. T. Gonzenbach, E. Tervoort, and L. J. Gauckler, “Processing Routes to Macroporous Ceramics: A Review,” *J. Am. Ceram. Soc.*, vol. 89, no. 6, pp. 1771–1789, Jun. 2006.
- [6] Y. Conde *et al.*, “Replication Processing of Highly Porous Materials,” *Adv. Eng. Mater.*, vol. 8, no. 9, pp. 795–803, Sep. 2006.
- [7] L. J. Gibson and M. F. Ashby, *Cellular Solids: Structure and Properties*. Cambridge University Press, 1999.
- [8] M. Scheffler and P. Colombo, *Cellular ceramics: structure, manufacturing, properties and applications*. John Wiley & Sons, 2006.
- [9] R. Brezny and D. J. Green, “Fracture Behavior of Open-Cell Ceramics,” *J. Am. Ceram. Soc.*, vol. 72, no. 7, pp. 1145–1152, Jul. 1989.
- [10] R. Brezny and D. J. Green, “The effect of cell size on the mechanical behavior of cellular materials,” *Acta Metall. Mater.*, vol. 38, no. 12, pp. 2517–2526, Dec. 1990.
- [11] R. Brezny and D. J. Green, “Uniaxial Strength Behavior of Brittle Cellular Materials,” *J. Am. Ceram. Soc.*, vol. 76, no. 9, pp. 2185–2192, Sep. 1993.
- [12] A. A. Wereszczak, E. Liu, V. Heng, T. P. Kirkland, and M. K. Ferber, “The high temperature compressive strength of non-oxide ceramic foams,” *Mater. Sci. Eng. A*, vol. 219, no. 1, pp. 224–228, Nov. 1996.
- [13] J. T. Richardson, Y. Peng, and D. Remue, “Properties of ceramic foam catalyst supports: pressure drop,” *Appl. Catal. Gen.*, vol. 204, no. 1, pp. 19–32, Nov. 2000.

- [14] A. Bhattacharya, V. V. Calmidi, and R. L. Mahajan, “Thermophysical properties of high porosity metal foams,” *Int. J. Heat Mass Transf.*, vol. 45, no. 5, pp. 1017–1031, Feb. 2002.
- [15] A. Inayat, J. Schwerdtfeger, H. Freund, C. Körner, R. F. Singer, and W. Schwieger, “Periodic open-cell foams: Pressure drop measurements and modeling of an ideal tetrakaidecahedra packing,” *Chem. Eng. Sci.*, vol. 66, no. 12, pp. 2758–2763, Jun. 2011.
- [16] B. Dietrich, “Pressure drop correlation for ceramic and metal sponges,” *Chem. Eng. Sci.*, vol. 74, no. Supplement C, pp. 192–199, May 2012.
- [17] D. Edouard, M. Lacroix, C. P. Huu, and F. Luck, “Pressure drop modeling on solid foam: State-of-the art correlation,” *Chem. Eng. J.*, vol. 144, no. 2, pp. 299–311, Oct. 2008.
- [18] A. J. Fuller, T. Kim, H. P. Hodson, and T. J. Lu, “Measurement and interpretation of the heat transfer coefficients of metal foams,” *Proc. Inst. Mech. Eng. J. Mech. Eng. Sci. Part C Lond.*, vol. 219, no. 2, pp. 183–191, Feb. 2005.
- [19] L. B. Younis and R. Viskanta, “Experimental determination of the volumetric heat transfer coefficient between stream of air and ceramic foam,” *Int. J. Heat Mass Transf.*, vol. 36, no. 6, pp. 1425–1434, Jan. 1993.
- [20] T. Fend, B. Hoffschmidt, R. Pitz-Paal, O. Reutter, and P. Rietbrock, “Porous materials as open volumetric solar receivers: Experimental determination of thermophysical and heat transfer properties,” *Energy*, vol. 29, no. 5–6, pp. 823–833, Apr. 2004.
- [21] K. Kamiuto and S. S. Yee, “Heat transfer correlations for open-cellular porous materials,” *Int. Commun. Heat Mass Transf.*, vol. 32, no. 7, pp. 947–953, Jul. 2005.
- [22] B. Dietrich, “Heat transfer coefficients for solid ceramic sponges – Experimental results and correlation,” *Int. J. Heat Mass Transf.*, vol. 61, pp. 627–637, Jun. 2013.
- [23] S. Cunsolo, M. Iasiello, M. Oliviero, N. Bianco, W. K. Chiu, and V. Naso, “Lord Kelvin and Weaire–Phelan Foam Models: Heat Transfer and Pressure Drop,” *J. Heat Transf.*, vol. 138, no. 2, p. 022601, 2016.
- [24] W. Xu, H. Zhang, Z. Yang, and J. Zhang, “The effective thermal conductivity of three-dimensional reticulated foam materials,” *J. Porous Mater.*, vol. 16, no. 1, pp. 65–71, Feb. 2009.
- [25] P. Thiyyagasundaram, J. Wang, B. V. Sankar, and N. K. Arakere, “Fracture toughness of foams with tetrakaidecahedral unit cells using finite element based micromechanics,” *Eng. Fract. Mech.*, vol. 78, no. 6, pp. 1277–1288, Apr. 2011.



- [26] W.-Y. Jang, S. Kyriakides, and A. M. Kraynik, “On the compressive strength of open-cell metal foams with Kelvin and random cell structures,” *Int. J. Solids Struct.*, vol. 47, no. 21, pp. 2872–2883, Oct. 2010.
- [27] J. Petrasch, F. Meier, H. Friess, and A. Steinfeld, “Tomography based determination of permeability, Dupuit–Forchheimer coefficient, and interfacial heat transfer coefficient in reticulate porous ceramics,” *Int. J. Heat Fluid Flow*, vol. 29, no. 1, pp. 315–326, Feb. 2008.
- [28] S. Haussener, P. Coray, W. Lipiński, P. Wyss, and A. Steinfeld, “Tomography-Based Heat and Mass Transfer Characterization of Reticulate Porous Ceramics for High-Temperature Processing,” *J. Heat Transf.*, vol. 132, no. 2, pp. 023305–023305, Dec. 2009.
- [29] A. Ortona, C. D’Angelo, S. Gianella, and D. Gaia, “Cellular ceramics produced by rapid prototyping and replication,” *Mater. Lett.*, vol. 80, pp. 95–98, Aug. 2012.
- [30] L. Schlier, W. Zhang, N. Travitzky, P. Greil, J. Cypris, and M. Weclas, “Macro-Cellular Silicon carbide Reactors for Nonstationary Combustion Under Piston Engine-Like Conditions,” *Int. J. Appl. Ceram. Technol.*, vol. 8, no. 5, pp. 1237–1245, 2011.
- [31] S. Bose, S. Vahabzadeh, and A. Bandyopadhyay, “Bone tissue engineering using 3D printing,” *Mater. Today*, vol. 16, no. 12, pp. 496–504, Dec. 2013.
- [32] M. Mott and J. R. G. Evans, “Solid Freeforming of Silicon Carbide by Inkjet Printing Using a Polymeric Precursor,” *J. Am. Ceram. Soc.*, vol. 84, no. 2, pp. 307–13, 2001.
- [33] J. W. Halloran, “Ceramic Stereolithography: Additive Manufacturing for Ceramics by Photopolymerization,” *Annu. Rev. Mater. Res.*, vol. 46, no. 1, pp. 19–40, 2016.
- [34] A. Zocca, P. Colombo, C. M. Gomes, and J. Günster, “Additive Manufacturing of Ceramics: Issues, Potentialities, and Opportunities,” *J. Am. Ceram. Soc.*, vol. 98, no. 7, pp. 1983–2001, 2015.
- [35] V. S. Deshpande, M. F. Ashby, and N. A. Fleck, “Foam topology: bending versus stretching dominated architectures,” *Acta Mater.*, vol. 49, no. 6, pp. 1035–1040, Apr. 2001.
- [36] S. Truscello, G. Kerckhofs, S. Van Bael, G. Pyka, J. Schrooten, and H. Van Oosterwyck, “Prediction of permeability of regular scaffolds for skeletal tissue engineering: A combined computational and experimental study,” *Acta Biomater.*, vol. 8, no. 4, pp. 1648–1658, Apr. 2012.

- [37] Z. C. Eckel, C. Zhou, J. H. Martin, A. J. Jacobsen, W. B. Carter, and T. A. Schaedler, “Additive manufacturing of polymer-derived ceramics,” *Science*, vol. 351, no. 6268, pp. 58–62, Jan. 2016.
- [38] J. T. Muth, P. G. Dixon, L. Woish, L. J. Gibson, and J. A. Lewis, “Architected cellular ceramics with tailored stiffness via direct foam writing,” *Proc. Natl. Acad. Sci.*, p. 219, Feb. 2017.
- [39] D. Ali and S. Sen, “Finite element analysis of mechanical behavior, permeability and fluid induced wall shear stress of high porosity scaffolds with gyroid and lattice-based architectures,” *J. Mech. Behav. Biomed. Mater.*, vol. 75, pp. 262–270, Nov. 2017.
- [40] P. F. Egan, V. C. Gonella, M. Engelsperger, S. J. Ferguson, and K. Shea, “Computationally designed lattices with tuned properties for tissue engineering using 3D printing,” *PLOS ONE*, vol. 12, no. 8, p. e0182902, Aug. 2017.
- [41] H. Cui, R. Hensleigh, H. Chen, and X. Zheng, “Additive Manufacturing and size-dependent mechanical properties of three-dimensional microarchitected, high-temperature ceramic metamaterials,” *J. Mater. Res.*, vol. 33, no. 3, pp. 360–371, Feb. 2018.
- [42] S. P. A Ortona, “Aging of reticulated Si-SiC foams in porous burners,” *Adv. Appl. Ceram.*, vol. 109, no. 4, pp. 246–251, 2010.
- [43] E. Rezaei, G. Bianchi, S. Gianella, and A. Ortona, “On the nonlinear mechanical behavior of macroporous cellular ceramics under bending,” *J. Eur. Ceram. Soc.*, vol. 34, no. 10, pp. 2133–2141, Sep. 2014.
- [44] A. Szczurek *et al.*, “Carbon periodic cellular architectures,” *Carbon*, vol. 88, pp. 70–85, Jul. 2015.
- [45] M. Aronovici *et al.*, “Heat and Mass Transfer in Ceramic Lattices During High-Temperature Oxidation,” *J. Am. Ceram. Soc.*, vol. 98, no. 8, pp. 2625–2633, Aug. 2015.
- [46] Y. S. Montenegro Camacho *et al.*, “Development of a robust and efficient biogas processor for hydrogen production. Part 1: Modelling and simulation,” *Int. J. Hydrog. Energy*, vol. 42, no. 36, pp. 22841–22855, Sep. 2017.
- [47] M. Pelanconi, M. Barbato, S. Zavattoni, G. L. Vignoles, and A. Ortona, “Thermal design, optimization and additive manufacturing of ceramic regular structures to maximize the radiative heat transfer,” *Mater. Des.*, vol. 163, p. 107539, Feb. 2019.

- [48] G. Bianchi, S. Gianella, and A. Ortona, “Design and Additive Manufacturing of Periodic Ceramic Architectures,” no. 01, 2017.



## 2 Design and optimization of a high-temperature latent heat storage unit

*The content of this chapter is used for an article by Ehsan Rezaei, Maurizio Barbato, Alberto Ortona and Sophia Haussener, submitted, Sep. 2019.*

### 2.1 Introduction

Latent heat thermal energy storage (LHTES) systems have the potential to achieve high energy density, given by the large latent heat of phase change materials. This benefit becomes even more relevant at high temperatures, as latent heat generally increases with increasing temperature [1]. LHTES systems can therefore provide a pathway for compact storage units, that, additionally, supply large amounts of thermal energy in a well-specified temperature range. Most developed LHTES systems are based on encapsulating a phase changing material (PCM) in spherical or cylindrical capsules and are designed to work at low temperatures (25-120°C) [2]. These PCMs have relatively low heat of fusion, limiting the energy density of the system, and low thermal conductivities, delaying the response of the storage system and decreasing its effectiveness [3]. Different strategies are suggested to reduce their thermal resistance, namely the addition of conducting meshes, microencapsulation of the PCM, or the addition of a highly conductive material to the PCM composition [3]–[5]. These approaches reduce the energy density of the system while also increasing the complexity and cost. A direct solution to this problem is the use of high temperature ( $> 120^{\circ}\text{C}$ ) PCMs with high conductivities. High temperature metal-based PCMs have larger thermal conductivity and heat of fusion than salts or organic PCMs [1], [6]. Such high-temperature LHTES can be used for various applications, including concentrating solar power plants, recuperator applications in ceramic and metal industry, heat storage for advanced adiabatic

compressed air energy storage, and heat recovery from burning biogas, natural gas or waste [1], [4], [7], [8].

The overall performance of an LHTES system is determined by two main modes of heat transfer: the convective heat transfer between the solid walls and the heat transfer fluid (HTF) and the conductive heat transfer within PCM and solid parts. For a high-temperature LHTES system, higher HTF mass flow rates are needed due to the larger energy densities of the systems. Therefore, a PCM (and encapsulation) with high thermal conductivity and large convective heat transfer coefficients are required. A common way to increase the convection consists in increasing the heat exchange surface area. This can be done by microencapsulation of PCM. However, microencapsulation of PCM for high temperatures is difficult and expensive [9]. A more practical approach is to increase the surface area by adding extended surfaces in the form of plates, fins, porous media, or similar [6], [10], [11].

The aim of this work is to present a design methodology for proper sizing, component choice, and operation of a high-temperature LHTES unit. The analysis is focused on the discharging process because of its relevance for many applications such as in a solar thermal power plant, where charging happens during an extended time period but a fast discharging is required [12]. The detailed design methodology is described and the results are presented in the form of different system performance metrics, namely its energy density and the storage effectiveness. A multi-objective optimization is then employed to find the appropriate design of the storage unit, given practicability constraints and performance requirements.

## 2.2 LHTES unit presentation and performance metrics

### 2.2.1 Configuration and materials

The configuration of the storage system used in this work is shown in Figure 2.1. The PCM is encapsulated in cylindrical tubes with the working fluid moving along the axial direction of the encapsulation. In some cases, the flow passage is filled with porous media to enhance the heat transfer between the encapsulated PCM and the HTF. A key benefit of such a configuration is its scalability by the in-series or parallel addition of multiple units. The eutectic Si-Mg (wt.% 56-44) material mixture is used as PCM, which has a high thermal conductivity (26 W/m/k at 1219 K for solid and liquid phases) and heat of fusion (757 kJ/kg at 1219 K) [13]. Air is chosen as the working fluid and SiSiC for the encapsulation and the porous heat transfer enhancing medium. SiSiC was selected based on its favorable properties at high temperatures, i.e. its ability to withstand oxidative environments, its relatively large thermal conductivity, and its enhanced mechanical properties [14], [15]. The thermodynamic properties of SiSiC and Si-Mg are given in Table 2.1.

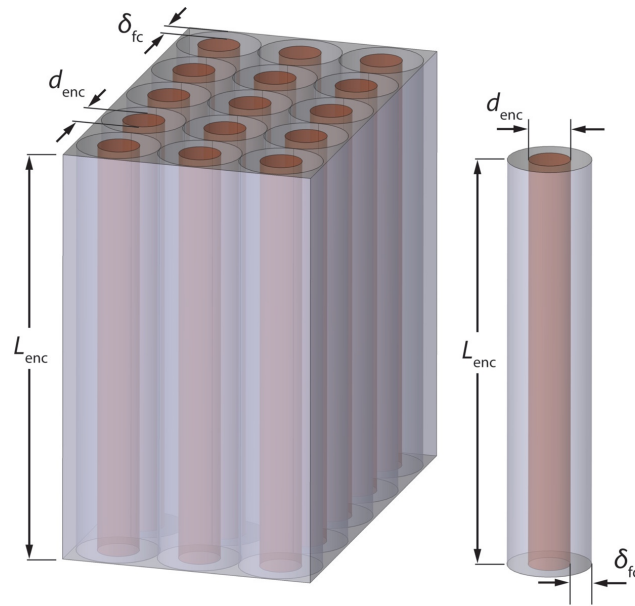


Figure 2.1. The parallel assembly of the LHTES system and a single unit (right). The red cylinder is the encapsulation containing the PCM, which is surrounded by the porous medium displayed in gray color.

Table 2.1. Thermodynamic characteristics of the materials used for this study.

Material	Composition [wt%]	Fusion temperature [K]	Heat of fusion [kJ/kg]	Density [kg/m <sup>3</sup> ]	Heat capacity [J/kg/K]	Thermal conductivity [W/m/K]	Ref.
SiSiC	30/70	1687/3003	-	2900	1350	43	[15]
Si-Mg	56/44	1219	757	1900	790	26	[13]

## 2.2.2 Performance metrics

We defined four different performance parameters of the LHTES unit: packing factor, energy density, storage effectiveness, and discharge exergy efficiency. As the study is focused on the discharging process only, the exergy efficiency is defined for discharging. The packing factor (PF) was defined as the ratio of the PCM volume to the total volume of the storage unit. The energy density,  $\eta$ , was defined as the heat extracted during discharging per storage unit volume. The effectiveness of the storage system,  $\epsilon$ , was defined as the fraction of the actual heat extracted from the system during the discharging time,  $Q_{dis}$ , to the theoretical possible heat that can be discharged. This parameter was evaluated considering a combination

of sensible effectiveness, latent effectiveness and total effectiveness of the storage system. Considering its definition, the total effectiveness is equal to unity when the storage is fully discharged and reaches the HTF inlet temperature.  $\epsilon$  can be calculated as:

$$\epsilon = \frac{Q_{\text{dis}}}{Q_{\text{theoretical}}} = \frac{\int_{V_{\text{su}}} \rho_{\text{su}} h_{\text{su}}(T) dV \Big|_{t=0}^{t=t_{\text{dis}}}}{U_{\text{su}}(T_{\text{in}}) - U_{\text{su}}(T_{\text{init}})}, \quad (2.1)$$

where the subscript **su** stands for the storage unit (i.e. PCM, encapsulation and the porous medium),  $\rho_{\text{su}}$  and  $h_{\text{su}}$  are the density and specific enthalpy, and  $U_{\text{su}}$  is the internal energy of the storage unit at a specified temperature. The discharging exergy efficiency,  $\eta_{\text{dis}}$ , was defined as [16]:

$$\eta_{\text{dis}} = \frac{\xi_{\text{dis}} - \xi_{\text{pump}}}{\xi_{\text{su}}}, \quad (2.2)$$

where  $\xi_{\text{dis}}$  is the net discharging exergy output by the HTF,  $\xi_{\text{pump}}$  is the equivalent thermal exergy for pumping, and  $\xi_{\text{su}}$  is the exergy released by the storage unit (both sensible and latent). The net discharging exergy output was defined as:

$$\xi_{\text{dis}} = \xi_{\text{f,out}} - \xi_{\text{f,in}} = \int_0^{t_{\text{dis}}} \left[ \int_{A_{\text{out}}} \rho_{\text{f}} u_z e_{\text{f}}(T) dA - \int_{A_{\text{in}}} \rho_{\text{f}} u_z e_{\text{f}}(T) dA \right] dt. \quad (2.3)$$

$u_z$  is the HTF superficial velocity in the  $z$ -direction (direction of the flow), and  $e_{\text{f}}$  is the specific exergy of the fluid. The exergy released by the storage unit is calculated as:

$$\xi_{\text{su}} = \int_{V_{\text{su}}} \rho_{\text{su}} e_{\text{su}}(T) dV \Big|_{t=0}^{t=t_{\text{dis}}}. \quad (2.4)$$

The specific exergy,  $e_{\text{su}}$ , was calculated as a function of temperature, neglecting the entropy generation due to pressure changes and considering the reference temperature,  $T_0$ , as 25 °C. Assuming that the energy needed for pumping is generated in a Rankine cycle and that the



fraction of electricity required for pumping is the same as the fraction of thermal exergy required for pumping, the equivalent thermal exergy for pumping can be calculated as [17]:

$$\xi_{\text{pump}} = - \int_0^{t_{\text{dis}}} \left[ \int_{V_{\text{fc}}} u_z \frac{dp}{dz} dV \right] dt \cdot \frac{1}{\eta_{\text{Rankine}} \eta_{\text{fan}}} \cdot \frac{\xi_{\text{dis}}}{Q_{\text{dis}}} . \quad (2.5)$$

The subscript, fc, stands for the flow channel domain and  $dp/dz$  is the pressure drop. The efficiency of the fan and the Rankine cycle were, respectively, assumed as 0.95 and 0.35 [17].

### 2.3 Modeling and design approach

We focus on discharging of the storage units, considering porous media in the channel for an enhanced heat transfer. For comparison, the analysis was also performed on units without porous media. The detailed analysis of the LHTES unit requires several input parameters: 1) the geometry of the storage system (number of storage units, encapsulation diameter, length and thickness and the fluid passage area), 2) the morphology of the porous medium (pore diameter and porosity), 3) the operation conditions (mass flow rate, inlet fluid temperature and the required outlet temperature), and 4) the initial conditions.

Typically in the LHTES design procedure, two main system specifications are known: the desired charging/discharging time and the energy or power of the system. In a parallel configuration, as shown in Figure 2.1, the power and energy of the system can be increased by the addition of LHTES units, thus these two parameters are excluded from the design process of the LHTES single unit. The discharging time of the LHTES system can also be incrementally increased by the addition of additional units in a series configuration. High exergy efficiency (greater than 0.95) are required for the TES [18]. We set the desired discharging time to one hour ( $t_{\text{dis,des}} = 1\text{h}$ ) and the desired exergy efficiency to 0.95 ( $\eta_{\text{dis,des}} = 0.95$ ).

The design procedure started with a preliminary step consisting of calculating the HTF mass flow rate,  $\dot{m}_f$ , and flow channel area,  $A_{\text{fc}}$ , as a function of the chosen encapsulation diameter and length,  $d_{\text{enc}}$  and  $L_{\text{enc}}$ , and the average pore diameter,  $d_p$ , in order to fulfill the desired performance metrics (discharging time and exergy efficiency). These parameters were then used in the axis-symmetric computational model (solved via finite element (FE) method) to simulate the detailed discharging process, starting from the initial conditions ( $T_{\text{init}} = 1229\text{ K}$ ) until the time at which the average HTF outlet temperature fell below  $T_{\text{stop}} = 1209\text{ K}$ . This

was done to ensure a small variation of the discharging HTF temperature (i.e. in the range of 1209-1229K).

The FE model was solved for different combinations of the design factors ( $d_{enc}$ ,  $L_{enc}$ ,  $d_p$ ). The optimization process was then performed in order to find the optimal sizing of the LHTES unit, maximizing the targeted performance metrics (energy density and total effectiveness). For this aim, meta-models were built as surrogates for the time consuming FE models. These models were then used to calculate the optimum design sizing of the LHTES unit using a multi-objective optimization approach. Figure 2.2 describes the procedure used to design the LHTES unit.

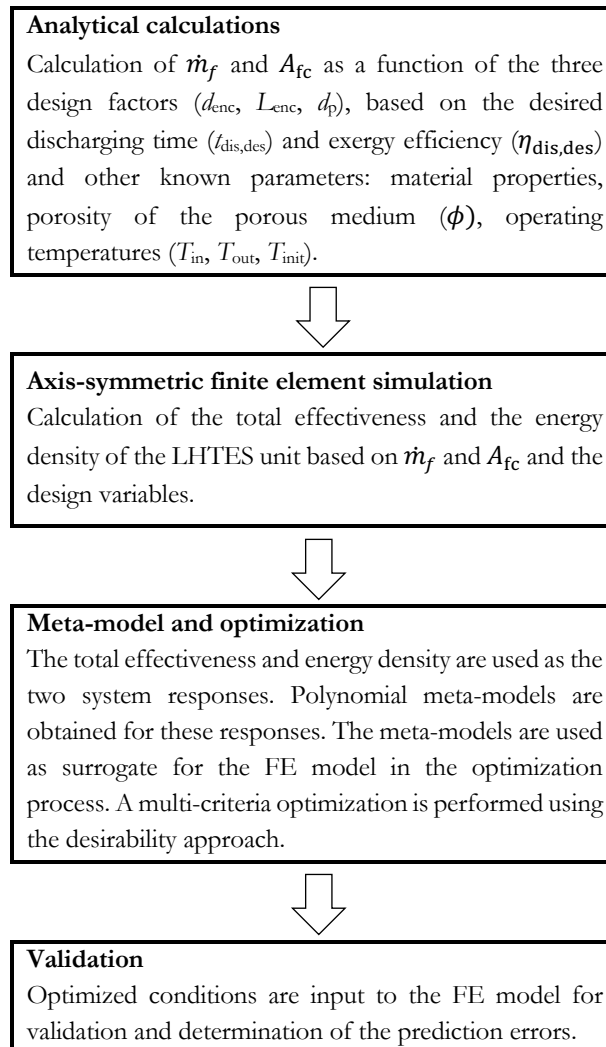


Figure 2.2. Flow diagram of the approach used for the design and optimization of the LHTES unit.

### 2.3.1 General assumptions

A schematic of the latent heat storage unit model is shown in Figure 2.3. The geometry of the model is built for each set of the design variables. Considering geometry of the available SiC tubes in the market (thickness of about 3-5 mm for tubes with internal diameters 20-100 mm), the encapsulation thickness was given as  $\delta_{enc} = \frac{d_{enc}+0.1}{40}$ . The mathematical model of the storage unit accounts for fluid flow and heat transfer. The following simplifications and assumptions were made for the numerical model: 1) the porous medium consists of two homogenous phases and it is assumed isotropic, 2) the solid and fluid phases in the porous medium are in local thermal non-equilibrium (LTNE), 3) phase change takes place at a distinct temperature within 4 K, 4) the porous domain is an optically thick medium, 5) the storage system is completely insulated, therefore there is no heat loss to the ambient, and 6) natural convection is considered in the HTF but not in the PCM, because the solidification of metal PCMs is a conduction-dominated process [19].

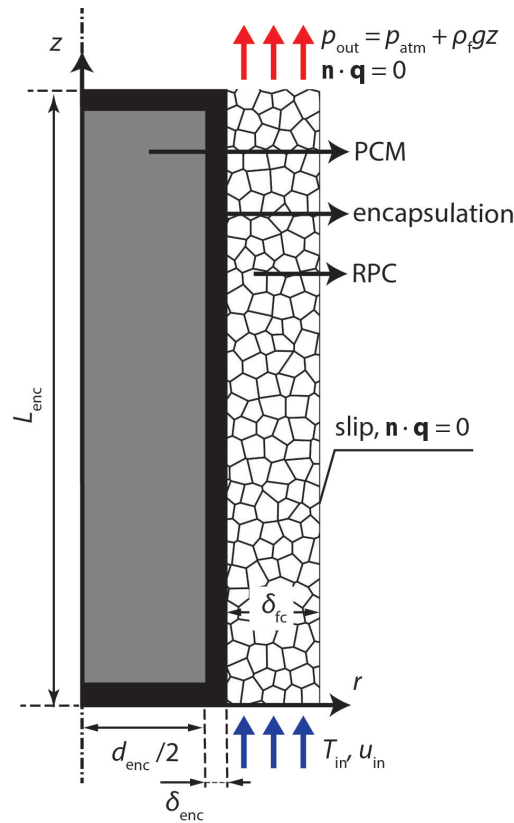


Figure 2.3. The axis-symmetric model domain of the LHTES unit and corresponding boundary conditions.

### 2.3.2 Preliminary analytical calculations

The analytical calculations were done in order to calculate the HTF mass flow rate and flow channel area as a function of the design variables ( $d_{\text{enc}}$ ,  $L_{\text{enc}}$ ,  $d_p$ ). In addition to the general assumptions, the following simplifications were made: 1) the HTF outlet temperature is constant during discharging,  $T_{\text{out}} = T_{\text{PCM}}$ , 2) the HTF properties are obtained at an average temperature equal to  $T_m = \frac{T_{\text{in}} + T_{\text{out}}}{2}$ , 3) the storage discharges completely ( $\epsilon = 1$ ), therefore at the end of the discharging time (at  $t_{\text{dis}} = t_{\text{dis,des}}$ )  $T_{\text{LHTES}} = T_{\text{in}}$ , and 4) the calculations of the pressure drop are based on the average velocity  $u_m = \frac{u_{\text{in}} + u_{\text{out}}}{2}$  in a 1D channel utilizing the Darcy-Forchheimer correlation (Table 2.2) for the channels filled with the porous medium. The pressure drop in the configurations without porous medium (empty channels) is calculated from a correlation for concentric annular ducts [20]:

$$\frac{\Delta p}{L_{\text{enc}}} = \frac{2\rho_f u_m^2 f}{D_h}, \quad (2.6)$$

where  $D_h$  is the hydraulic diameter of the flow channel, and  $f$  is the friction factor calculated as:

$$f = \frac{16(1 - r_1)^2}{1 + r_1^2 - 2r_2^2} \left( \frac{\mu_f}{\rho_f u_m D_h} \right), \quad (2.7)$$

where:

$$r_1 = \frac{d_{\text{enc}} + 2\delta_{\text{enc}}}{d_{\text{enc}} + 2\delta_{\text{enc}} + 2\delta_{\text{fc}}}, \quad (2.8)$$

$$r_2 = \left( \frac{1 - r_1^2}{2 \ln\left(\frac{1}{r_1}\right)} \right)^{0.5} \quad (2.9)$$

$\delta_{\text{enc}}$  and  $\delta_{\text{fc}}$  are the thicknesses of the encapsulation and the flow channel (see Figure 2.3) . The analytical calculations were performed using Matlab symbolic toolbox. Knowing the desired time to discharge the total energy of the LHTES unit and the desired discharging exergy efficiency (for a system with an effectiveness equal to unity), the mass flow rate and

the flow passage area were calculated for each set of the design variables. The mass flow rate and flow passage area were then fed into the FE model for a detailed analysis of the discharging process. The flowchart of the analytical calculations is shown in Figure 2.4.

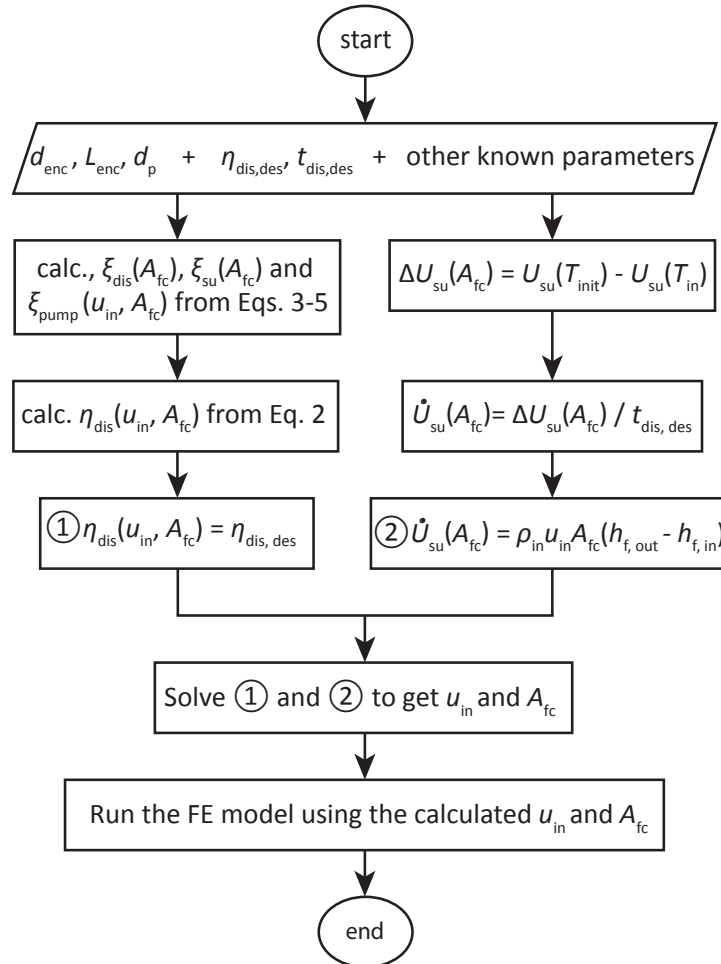


Figure 2.4. Flow chart of the analytical model calculations in order to obtain  $u_{in}$  and  $A_{fc}$  that were then fed to the FE model.

### 2.3.3 Axis-symmetric FE model

The continuity and Brinkman equations with Forchheimer corrections for a weakly compressible flow were employed for the fluid flow in the porous medium [21]:

$$\frac{\partial \phi \rho_f}{\partial t} + \mathbf{u}_f \cdot \nabla \rho_f = 0 \quad (2.10)$$

$$\begin{aligned} \frac{\rho_f}{\phi} \frac{\partial \mathbf{u}_f}{\partial t} + \frac{\rho_f}{\phi^2} (\mathbf{u}_f \cdot \nabla) \mathbf{u}_f \\ = -\nabla p \\ + \nabla \cdot \left[ \frac{\mu_f}{\phi} (\nabla \mathbf{u}_f + (\nabla \mathbf{u}_f)^T) - \frac{2}{3} \frac{\mu_f}{\phi} (\nabla \cdot \mathbf{u}_f) \mathbf{I} \right] - \left[ \frac{\mu_f}{K} + \rho_f C |\mathbf{u}_f| \right] \mathbf{u}_f \\ + \rho_f \mathbf{g} \end{aligned} \quad (2.11)$$

The LTNE energy equations were used for the two phases of the porous medium:

$$\phi \rho_f c_{p,f} \frac{\partial T_f}{\partial t} + \rho_f c_{p,f} \mathbf{u}_f \cdot \nabla T_f - \nabla \cdot (\phi \lambda_f \nabla T_f) = h_v (T_s - T_f), \quad (2.12)$$

$$(1 - \phi) \rho_s c_{p,s} \frac{\partial T_s}{\partial t} - \nabla \cdot [(1 - \phi) \lambda_s \nabla T_s] = h_v (T_f - T_s) + Q_{\text{rad}}, \quad (2.13)$$

where  $Q_{\text{rad}}$  is the radiation source term, which is accounted for using the P1 approximation [22] by solving the following diffusion equation:

$$-\nabla \cdot \left( \frac{1}{3\beta} \nabla G \right) + \kappa (G - 4\pi I_b) = 0, \quad (2.14)$$

$$G = \int_{4\pi} I(\Omega) d\Omega. \quad (2.15)$$

$G$  is the incident radiation function, which is the total radiation intensity affecting on a point from all directions and  $I(\Omega)$  is the radiative intensity traveling in certain direction,  $\Omega$ . The absorption coefficient can be calculated as a function of the extinction coefficient and the scattering albedo. The radiative source term in Eq. 2.13 can be then calculated as:

$$Q_{\text{rad}} = \kappa (G - 4\pi I_b) \quad (2.16)$$

Radiation was assumed gray. The correlations used to calculate the transport and radiation properties in the porous medium are summarized in Table 2.2. The radiation properties and other known parameters, used in the analytical and detailed mathematical models are given in Table 2.3.

Table 2.2. Correlations used to calculate the convective heat transfer and mass transport, and radiative transport parameters.

Correlations	References
$\frac{h_v d_h}{\lambda_f S_v} = 0.31 \left( 110 \frac{\rho_f u_f d_h}{\mu_f} + 1.45 \left( \frac{\rho_f u_f d_h}{\mu_f} \right)^2 \right)^{\frac{1}{3}} \text{Pr}^{\frac{1}{3}}$	[23], [24]
$\frac{\Delta p}{L_{\text{enc}}} = \frac{\mu_f}{K_{\text{Di}}} u_m + \rho_f C_{\text{Di}} u_m^2$ $K = \frac{\phi d_h^2}{110} \quad \text{and} \quad C = \frac{1.45}{d_h \phi^2}$	
$d_h = \frac{4\phi}{S_v} \quad \text{and} \quad S_v = 2.87 \frac{(1 - \phi)^{0.25}}{d_p}$	
$\beta = \frac{5.5173(1 - \phi)}{d_p}$	[25]

Table 2.3. The parameters used in the analytical and numerical models.

Parameter	Value
$t_{\text{dis,des}}$ [h]	1
$\eta_{\text{dis,des}}$ [-]	0.95
$T_{\text{init}}$ [-]	1229
$T_{\text{HTF,in}}$ [-]	1119
$\Delta T_{\text{lat}}$ [-]	4
$T_{\text{stop}}$ [K]	1209
$\alpha_{\text{SiSiC}}$ [-]	0.1
$\phi$ [-]	0.9

To account for the heat transfer in the phase changing domain, the standard energy equation for solids with the apparent heat capacity formulation was considered [26], which assumes that the phase change occurs within a certain temperature range around the PCM's melting temperature. The specific heat capacity of the PCM in the phase changing range was calculated as a function of the solid phase fraction,  $\theta_s$ :

$$c_{p,PCM} = \frac{1}{\rho_{PCM}} (\theta_s \rho_s c_{p,s} + (1 - \theta_s) \rho_l c_{p,l}) + Q_{lat} \frac{\partial \alpha_m}{\partial T} = c_{p,s} + Q_{lat} \frac{\partial \alpha_m}{\partial T} \quad (2.17)$$

$$\alpha_m = \frac{1}{2} \frac{\theta_l \rho_l - \theta_s \rho_s}{\theta_l \rho_l + \theta_s \rho_s} = \frac{1 - 2\theta_s}{2} \quad (2.18)$$

For the free fluid flow inside the channels and heat transfer in the fluid and solid domains, the standard Navier-Stokes and energy equations were used. The HTF was assumed an ideal gas and its properties were calculated as a function of the local temperature.

The initial values and the boundary conditions were:

- Constant HTF velocity and temperature at the HTF inlet.
- No conductive and radiative heat flux at the HTF outlet.
- Atmospheric pressure plus hydrostatic pressure at the HTF outlet.
- No slip condition at the wall between encapsulation and RPC.
- Slip boundary with no viscous effects at the outer wall of the HTF channel.
- Initial constant temperature in all domains.
- Adiabatic conditions for the rest of the solid boundaries.
- Symmetry at the outer wall of the HTF channel.

In order to avoid conflicting boundary conditions between the solid and fluid physics at the entry domain, a 5 mm inlet channel was added to the inlet. The fluid inlet temperature was given as a smooth function of time, changing from  $T_{init}$  to  $T_{in}$  in 5 seconds. The input parameters are summarized in Table 3.

An axis-symmetric model was developed based on the abovementioned equations and boundary conditions in Comsol Multiphysics package® (ver. 5.3) interlinked with Matlab. The model was solved in a time range from zero to a point where the average  $T_{HTF,out}$  reached  $T_{stop}$ . The fully coupled set of equations was computed using the direct solver PARADISO. A second order Lagrange discretization was chosen for the two temperature variables. A first



order discretization scheme was used for the rest of the dependent variables. For the time integration, backward differentiation formula with variable order of accuracy (maximum 2<sup>nd</sup> order) was selected. The choice of the relative tolerance was based on evaluating the overall energy balance of the system in the entire discharging time. It was observed that setting the relative tolerance as  $10^{-6}$ , the transient energy balance errors for all the models were less than 1.05%. The flow channel domain was meshed by quadratic elements with variable element sizes (largest element size equals  $0.1 d_{enc}$ ) in order to have finer elements near the inlet. The encapsulation and PCM domains were meshed using triangular elements. The smallest and largest geometries were chosen for the mesh convergence analysis. The mesh convergence was done by doubling the grid size and comparing the temperatures, velocity and the discharging time, which varied by less than 0.42%.

### **2.3.4 Design of experiments and optimization**

$d_{enc}$ ,  $L_{enc}$  and  $d_p$ , were used as the input variables for the parametric study. All the combinations of these factors with different levels (5 levels for  $d_{enc}$  and  $L_{enc}$ , 3 levels for  $d_p$ ) were tested to form a full factorial model consisting of 75 runs (Table 2.4). The choice of these foam morphologies was based on commercial foams available (for example the SiC-based foams produced by EngiCer SA, Switzerland, or Foseco International Ltd).

The optimization was based on the effectiveness and energy density, two system performance responses. We fit a meta-model, in a polynomial shape, that best approximated the FE model's response results. For complete description of the responses, a sufficiently high order polynomial had to be considered. The terms of the model were selected via an exhaustive search process in which all possible models with various terms were created and the model with the minimum number of terms that satisfied the adjusted- $R^2 > 0.99$  was selected.

The surrogate models were then used for the optimization process. A desirability method was employed, where the objective goals were included in a single cost objective function (the desirability function). In the desirability method, weight and importance factors can be used to define the shape of the desirability function for each goal and the importance of one goal relative to the others. The optimization starts by choosing a random point and following the steepest slope to achieve a local maximum. A total of 1000 starting points were used to ensure that the optimized point within the full design space is reached. The data analysis and optimization were all carried out using the commercially available software Design Expert 11.0 (Stat-Ease, Inc., MN, USA) and Matlab optimization toolbox. The Pareto frontier was obtained using Matlab's multi-objective genetic algorithm, using "gamultiobj" solver with a population size of 1000 and a Pareto fraction of 0.35.

Table 2.4. Design variables and their values used in the parametric study.

Design variable	Levels	Values
<b>A:</b> $d_{\text{enc}}$ [m]	5	0.02, 0.04, 0.06, 0.08, 0.1
<b>B:</b> $L_{\text{enc}}$ [m]	5	0.2, 0.4, 0.6, 0.8, 1
<b>C:</b> $d_p$ [m]	3	0.00125, 0.0025, 0.005
<b>Total runs</b>	5X5X3	75

## 2.4 Results and discussion

### 2.4.1 FEM results

For the performance comparison of a LHTES unit without porous media, i.e. empty flow channels, were also solved for encapsulation sizes of  $d_{\text{enc}} = 5\text{-}40$  mm and  $L_{\text{enc}} = 200\text{-}1000$  mm. As  $d_{\text{enc}}$  increased, the total effectiveness of the system abruptly decreases from 0.9 at  $d_{\text{enc}} = 5$  mm to almost zero at  $d_{\text{enc}} = 40$  mm (Figure 2.5) ). This resulted from the larger amount of energy that needed to be discharged when increasing the encapsulation diameter. A larger heat exchange between the encapsulation and HTF was required at larger encapsulation sizes. As a solution, an extended surface area in the flow channel was proposed in order to boost the convective heat transfer rate, done by the addition of porous medium in the flow channels.

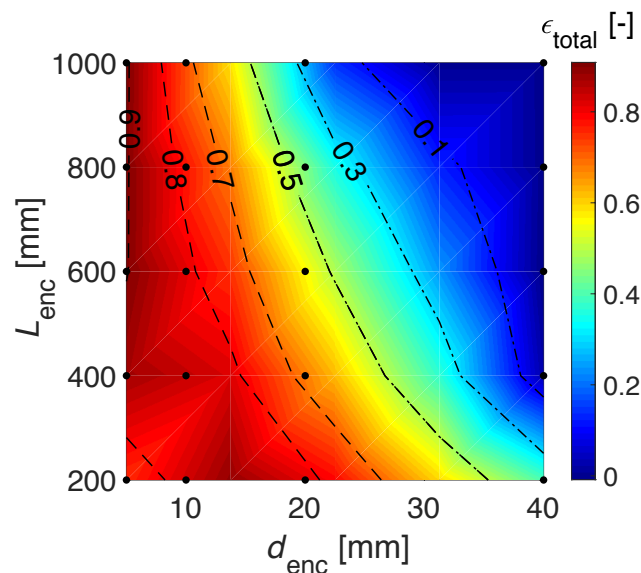


Figure 2.5. Total effectiveness of an LHTES units with empty flow channels (without porous medium) for different encapsulation sizes. The black dots are the simulated points; the contours were linearly interpolated.

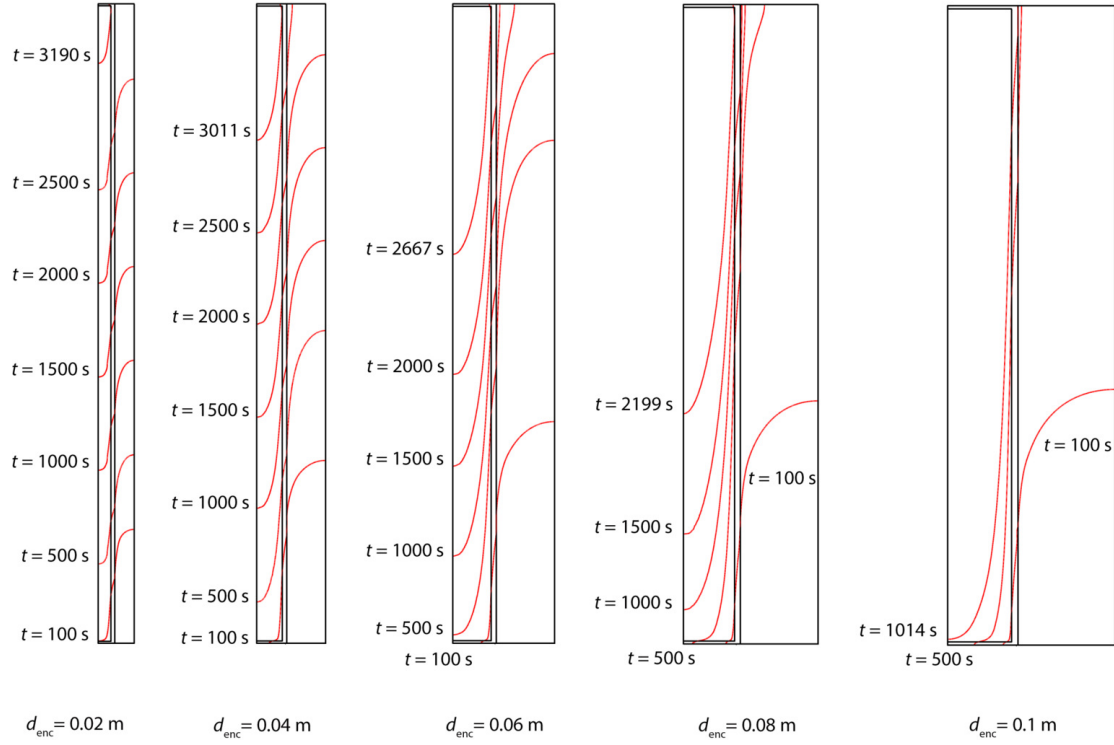


Figure 2.6. Constant solid temperature contour at  $T_s = 1219$  K for different time steps and for different  $d_{enc}$  until the outlet temperature fell below  $T_{stop} = 1209$  K. The mass flow rate and the flow channel thickness are calculated in the preliminary analytical calculations as a function of the design factors ( $d_{enc}$ ,  $L_{enc}$ ,  $d_p$ ) for each model. The PCM domain is on the left side of each case, the porous media filled domain is to the right side. For these five cases,  $L_{enc}$  and  $d_p$  are constant and equal to 1000 mm and 5 mm, respectively.

The parametric model was solved for different encapsulation sizes ( $d_{enc}$ ,  $L_{enc}$ ) and porous morphologies. The average exergy efficiency of the solved models was  $0.945 \pm 0.003$ , showing that the assumptions for calculation of the exergy efficiency in the preliminary step were reasonable. Figure 2.6 exemplifies typical solidification of the PCM in several geometries with different  $d_{enc}$  at discharging times. These graphs show the position of the liquid-solid interface in the PCM domain. The PCM solidifies from bottom to top with a U-shaped melt front. At  $d_{enc} = 100$  mm, the solidification started along the encapsulation wall, while the internal part remained liquid. Therefore as  $d_{enc}$  increases, the contours become much larger and tend to be vertical showing that the solidification is faster in the axial direction than that in the radial direction. For larger diameters, the convective heat transferred within the porous medium is enhanced and, therefore, the conduction resistance in PCM and also in the porous medium controls the performance of the system. The simulations were stopped as soon as the outlet

average temperature fell below  $T_{\text{stop}}$ . For  $d_{\text{enc}} = 20$  mm, most of the latent heat was discharged and the process stopped at  $t_{\text{dis}} = 3190$  s. Increasing  $d_{\text{enc}}$  resulted in lower  $t_{\text{dis}}$ , as low as 1014 s for  $d_{\text{enc}} = 100$  mm.

An example of the HTF outlet average temperature during discharging is plotted in Figure 2.7. Three zones were distinguishable: 1) a decrease in the outlet temperature from the initial temperature due to discharging of the sensible heat above the melting point, 2) a quasi-constant outlet temperature due to the latent heat discharge, and 3) a rapid decreasing from the melting point in the discharge temperature due to the discharge of the sensible heat.

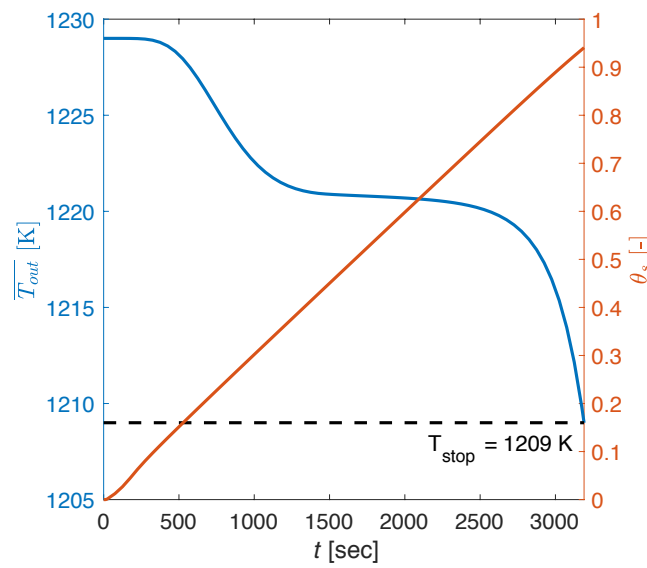


Figure 2.7. The HTF outlet temperature (blue) and the solid fraction of the PCM (orange) plotted versus time for one typical example ( $d_{\text{enc}} = 20$  mm,  $L_{\text{enc}} = 1000$  mm and  $d_p = 5$  mm).

Figure 2.8 displays the sensible, latent and the total effectiveness for a LHTES with a porous foam with  $d_p = 2.5$  mm. The effectiveness (as defined by Eq. 2.1) indicates the effectiveness of the storage unit discharging process. The latent heat effectiveness is equal to the solid fraction of the PCM at the discharging time. At a given  $L_{\text{enc}}$ , the effectiveness (sensible, latent and the total) decreases when increasing  $d_{\text{enc}}$ . One exception was observed for pore diameters of 1.25 mm (not shown) and 2.5 mm (shown in Figure 2.8) at larger  $L_{\text{enc}}$  (800, 1000 mm), where by increasing  $d_{\text{enc}}$ , the sensible effectiveness initially decreased and then increased again. This was a result of the very large flow passage area at those points and thus, almost all the discharged energy was the sensible heat of the porous medium and not the latent part. Compared to a LHTES unit without porous media (Figure 2.5), the addition of porous media

enables a larger design space at which a total effectiveness above 0.9 can be maintained. All the systems with  $d_{enc} = 20\text{-}40$  mm had a total effectiveness ranging between 0.54-0.94 (compared to values ranging 0-0.81 in the case without porous media).

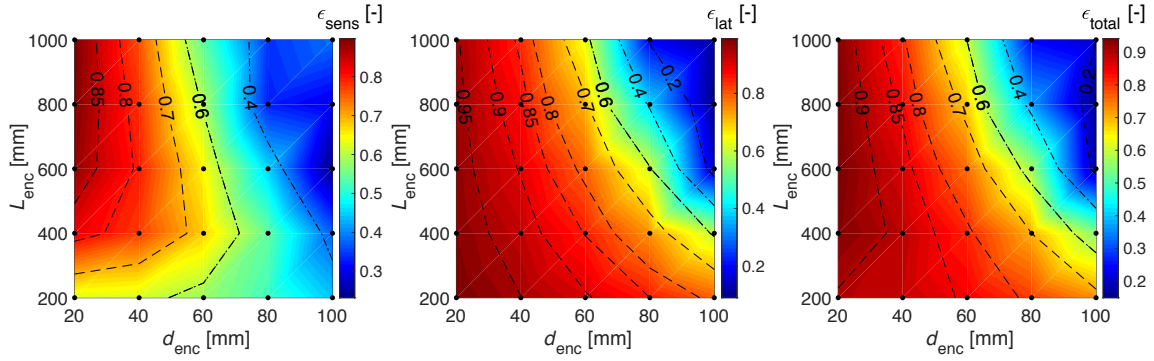


Figure 2.8. From left to right: the sensible, latent and the total effectiveness for the LHTES units for different encapsulation sizes with  $d_p = 2.5$  mm. The black dots are the simulated points, the contours were linearly interpolated.

PF in the range of 0.02-0.59 were achieved for the different cases simulated (Figure 2.9). Given the desired discharge time of 1 hour and desired exergy efficiency of 0.95, an increase in the encapsulation length  $L_{enc}$  resulted in decreased PF as a larger amount of heat needed be discharged, requiring larger mass flow rates and, as a result, requiring an increased flow channel area as to compensate for the decrease in the HTF pumping work (and keep the exergy efficiency as desired). On the other side, increasing  $d_{enc}$  (especially at lower  $L_{enc}$  and larger  $d_p$ ) resulted in a larger PCM/unit volume ratio, which increased PF. Decreasing  $d_p$  also increased the HTF pumping work and required compensation by increasing the flow channel area, decreasing PF. Typical calculated energy densities of the LHTES units are presented in Figure 2.10. For all the simulated cases, the values varied in the range of 33-752 MJ/m<sup>3</sup>. The energy density depended on the variation of PF and effectiveness. The former indicates the available latent heat per unit volume, the latter represents the available energy that can be discharged. Increasing  $L_{enc}$  resulted in a considerable decrease of PF and, thus, decrease in the energy density. Increasing  $d_{enc}$  resulted in a considerable decrease in the effectiveness (especially for larger lengths) and, thus, decreased the energy density. A trade-off between these two factors resulted in an optimal condition at  $d_{enc} = 40$  mm and  $L_{enc} = 200$  mm. For small  $d_{enc}$ , increasing  $L_{enc}$  increased the effectiveness but at the expense of a significant decrease in the PF of the unit. From a practical point of view, larger unit sizes are desired.

Therefore, proper sizing of the LHTES unit is a trade-off between performance and other requirements such as manufacturability and practicability.

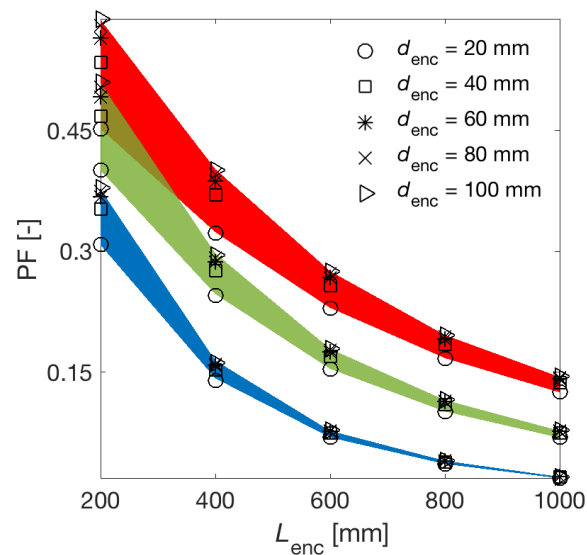


Figure 2.9. The packing factor for all simulated LHTES units. The blue, green and red zones, respectively, show the results for  $d_p = 1.25$ ,  $2.5$  and  $5$  mm.

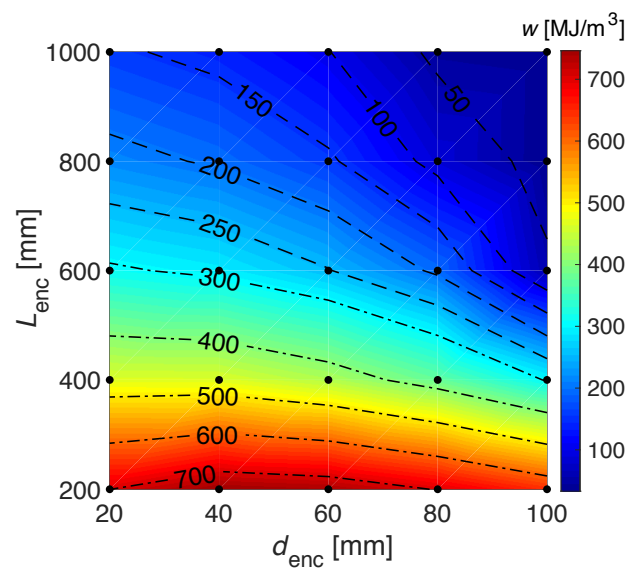


Figure 2.10. The energy density for LHTES units with varying  $d_{enc}$  and  $L_{enc}$  at constant  $d_p = 2.5$  mm. The black dots are the simulated points, the contours were linearly interpolated.

Page | 28

### 2.4.2 Polynomial meta-model

For the creation of the meta-model used for the optimization process, the data points with  $\epsilon < 0.5$  were ignored. Most of the neglected cases were related to cases with large  $d_{enc}$  (80 and 100 mm) and not particularly interesting in a final application. Therefore, the predictions of the polynomial model in those regions might be less accurate. Furthermore, preliminary calculations showed that certain input parameter (especially for points within  $d_p = 5$  mm,  $d_{enc} \leq 60$ , and  $L_{enc} \leq 400$ ) resulted in small flow channel thicknesses, which contradicts the assumptions of the volume averaging models used for this study. We kept those data points when creating the meta-models but carefully interpreted the results in that region.

The coefficients of the polynomial models were obtained using an ordinary least square fitting. The least square assumptions were evaluated using diagnostics plots to make sure that the residuals were normally and independently distributed with constant variance. Normal probability plots of the residuals were checked to ensure that there was no outlier and the residuals followed a normal distribution. In addition, the residuals were plotted versus the predicted values to ensure that the residuals were randomly distributed with constant variations.

High coefficient of determination ( $R^2$ ) showed that the models fit the data very well (Table 2.5). The high values of the predicted  $R^2$  (0.983 and 0.989) showed that the model predictions were accurate within the design space. A reasonable agreement between the predicted and adjusted- $R^2$  values was observed. Their values were within 0.01 of each other, which suggests a model with stable predictions. The adequacy precision, which measures the ratio of the signal to noise, was higher than 64.48 (suggested to be more than 4). Therefore, the two polynomial meta-models were considered valid within the design space:

$$\begin{aligned}
 \epsilon = & 8.89 \times 10^{-1} + 4.02 d_{enc} + 3.51 \times 10^{-1} L_{enc} - 1.39 \times 10 d_p \\
 & - 1.71 \times 10 d_{enc} L_{enc} - 2.05 \times 10^3 d_{enc} d_p - 1.35 \times 10^2 L_{enc} d_p \\
 & - 6.88 d_{enc}^2 - 5.98 \times 10^{-2} L_{enc}^2 + 3.46 \times 10^3 d_p^2 \\
 & + 1.45 \times 10^4 d_{enc} L_{enc} d_p - 2.11 \times 10^2 d_{enc}^2 L_{enc} \\
 & + 5.73 \times 10^3 d_{enc}^2 d_p - 4.42 d_{enc} L_{enc}^2 + 1.31 \times 10^4 d_{enc} d_p^2 \\
 & + 1.65 \times 10^4 L_{enc} d_p^2 + 2.64 \times 10^4 d_{enc}^2 L_{enc} d_p \\
 & - 1.79 \times 10^6 d_{enc} L_{enc} d_p^2
 \end{aligned} \tag{2.19}$$

$$\begin{aligned}
 w = & 7.63 \times 10^2 + 7.72 \times 10^2 d_{\text{enc}} - 2.94 \times 10^3 L_{\text{enc}} + 2.86 \times 10^5 d_p \\
 & + 6.61 \times 10^3 L_{\text{enc}} d_p - 2.14 \times 10^4 d_{\text{enc}}^2 + 2.96 \times 10^3 L_{\text{enc}}^2 \\
 & - 4.56 \times 10^7 d_p^2 - 2.15 \times 10^5 L_{\text{enc}}^2 d_p + 4.01 \times 10^7 L_{\text{enc}} d_p^2 \\
 & - 7.99 \times 10^2 L_{\text{enc}}^3
 \end{aligned} \tag{2.20}$$

Table 2.5.  $R^2$  value and adequacy parameters for the calculated regression models.

	Effectiveness	Energy density
<b><math>R^2</math></b>	0.994	0.993
<b>Adjusted <math>R^2</math></b>	0.991	0.992
<b>Predicted <math>R^2</math></b>	0.983	0.989
<b>Adequacy precision</b>	64.48	83.92

### 2.4.3 Optimization

The meta-models were used as surrogates for the FE model in order to find the best design parameters through a multi-criteria optimization process. The aim of the optimization can be different depending on the design constraints and requirements. In this study we optimized the model for two independent cases:

- 1- A general case where the response outputs (effectiveness and energy density) were maximized within the upper and lower bounds of the design factors.
- 2- A specific case favoring manufacturability and practicability of the system where the encapsulation size ( $d_{\text{enc}}$  and  $L_{\text{enc}}$ ) and energy density were maximized while  $\epsilon > 0.9$ .

A general overview of the optimization problem was achieved by calculating the Pareto frontier of the response variables Figure 2.11. These data points are a set of non-inferior solutions; i.e., an increase in one of the objectives requires a decrease in the other objective. The Pareto frontier reveals the limitations of the process for each objective. In the chosen design variable space, a maximum of 0.95 and 810 MJ/m<sup>3</sup> was achieved for the effectiveness and the energy density, respectively.



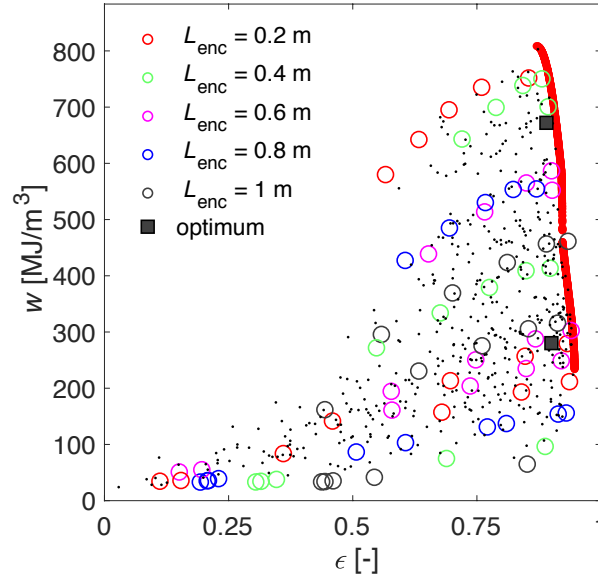


Figure 2.11. Pareto frontier (red line), numerical data points obtained by the FE model (colored circles) and calculated points from the regression model utilizing the meta-models (black dots). The predicted optimization points for case 1\* and 2 are shown in filled black squares.

The desirability method was used to solve the multi-criteria optimization problems. The mathematical representation of the optimization problems and their results are summarized in Table 2.6. The weight and importance factors ( $w_i$  and  $r_i$ ) in the desirability functions were set to 1 and 3, respectively. It was observed that for case 1 the optimal model parameters resulted in an LHTES unit with a small flow channel thickness, too small for the porous media modeling assumptions to be valid. Therefore, we added an additional constraint, namely  $\frac{\delta_{fc}}{d_p} \geq 3.5$  [27], to find the maximum desirability for case 1. In Table 2.6, these data points are shown with a black star. As expected, the optimization results are very close to the Pareto frontier (Figure 2.11) but not exactly on the frontier line. The difference between the optimized results and the Pareto frontier are caused by the additional constraints (manufacturability and modeling assumptions), which are not given on the Pareto frontier.

In order to evaluate the accuracy of the predicted values, the FE model were solved using the same design variables as in the optimized points. The results and comparisons are shown in Table 2.7. The meta-models were able to predict the optimized sizing of the system with an error below 6.4%. While this accuracy is sufficient in our case, better accuracy could be achieved by performing an iterative optimization including the predicted points to create new meta-models.

Table 2.6. Mathematical representation of the optimization cases and their results.

Case 1:

$$\left\{ \begin{array}{l} \text{maximize} \quad D_1 = \left( \prod_{i=1}^2 d_{Y_i}^{r_i} \right)^{1/\sum r_i} \\ 0.02 < d_{\text{enc}} < 0.1 \\ 0.2 < L_{\text{enc}} < 1 \\ 0.00125 < d_p < 0.005 \end{array} \right.$$

where

$$d_{Y_i} = \left( \frac{Y_i - Y_i^l}{Y_i^u - Y_i^l} \right)^{w_i}, \quad (Y_1 = \epsilon \text{ \& } Y_2 = w)$$

Results:

$d_{\text{enc}}$ [mm]	20.0	40.0*
$L_{\text{enc}}$ [mm]	200.0	200.0*
$d_p$ [mm]	3.45	1.87*
$\epsilon$ [-]	0.876	0.890*
$w$ [MJ]/m <sup>3</sup>	806.3	672.1*
$D_1$	0.840	0.842*

\* The results including the additional constraint as:  $\frac{\delta_{\text{fc}}}{d_p} \geq 3.5$

---

Case 2:

$$\left\{ \begin{array}{l} \text{maximize} \quad D_2 = \left( \prod_{i=1}^4 d_{Y_i}^{r_i} \right)^{1/\sum r_i} \\ 0.02 < d_{\text{enc}} < 0.1 \\ 0.2 < L_{\text{enc}} < 1 \\ 0.00125 < d_p < 0.005 \end{array} \right.$$

where

$$d_{Y_i} = \left( \frac{Y_i - Y_i^l}{Y_i^u - Y_i^l} \right)^{w_i}, \quad (Y_1 = w \text{ \& } Y_2 = d_{\text{enc}} \text{ \& } Y_3 = L_{\text{enc}})$$

$$d_{Y_4} = \begin{cases} 0 & \epsilon < 0.9 \\ 1 & \epsilon \geq 0.9 \end{cases}$$

Results:

$d_{\text{enc}}$ [mm]	45.8
$L_{\text{enc}}$ [mm]	795.5
$d_p$ [mm]	3.93
$\epsilon$ [-]	0.900
$w$ [MJ]/m <sup>3</sup>	280.2
$D_2$	0.509

Table 2.7. Validation of the optimization results and the comparison with simulations.

	<b>Case 1</b>		<b>Case 2</b>	
	$\epsilon$ [-]	$w$ [MJ]/m <sup>3</sup>	$\epsilon$ [-]	$w$ [MJ]/m <sup>3</sup>
<b>Prediction</b>	0.890	672.1	0.900	280.2
<b>Simulation</b>	0.903	706.0	0.842	268.1
<b>Error (%)</b>	1.5	5.0	6.4	4.3

A graphical understanding of the optimization problems is given by an overlay contour graph of the unit performance metrics (Figure 2.12). The pore diameter is fixed for each subfigure and the contours of the effectiveness and energy density are superimposed. These plots give a simple and quick overview of the variation of the two responses in different parts of the design space. They represent design guidelines for the LHTES unit. Increasing  $d_p$ , the energy density in each point of the design space is increased. For  $d_p = 1.25$  mm, almost half of the design space has an energy density less than  $100 \text{ MJ/m}^3$ . In general, units with  $d_p = 5$  mm showed larger effectiveness (almost all cases above 0.5). However, selecting  $d_p = 2.5$  mm offered more options for a storage unit with an effectiveness above 0.9. Generally, the energy density was less sensitive with respect to  $d_{enc}$  while the total effectiveness was less sensitive with respect to  $L_{enc}$ .

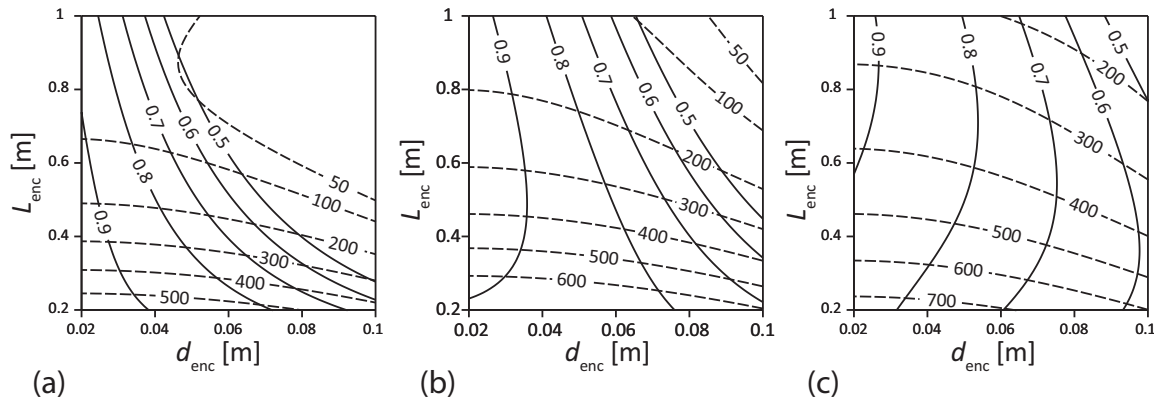


Figure 2.12. The overlay contour plots for a)  $d_p = 1.25$  mm, b)  $d_p = 2.5$  mm, and c)  $d_p = 5$  mm. The isolines of total effectiveness are shown in solid lines and the isolines of the energy density  $[\text{MJ}/\text{m}^3]$  in dashed lines.

In our study, the selection of the operating conditions (such as HTF mass flow rate and the inlet temperature) were excluded from the design optimization since the former was calculated as a function of the design variables ( $d_{enc}$ ,  $L_{enc}$ ,  $d_p$ ), and the latter was kept constant. In general, the selection of the optimum LHTES design depends on the constraints of the designer. Storage units with large effectiveness and energy densities can be achieved by the selection of a small encapsulation size. However from a practical point of view, this is not the best choice; a longer encapsulation may be preferred for storage systems with parallel configuration (Figure 2.1) in order to minimize the installation's surface area. Manufacturing encapsulations with larger diameter also simplifies the storage system design as it reduces the number of units in the LHTES configuration. Finally, the LHTES system can be scaled by in-series or parallel

addition of multiple units. A progressive increase in the discharging time and net power of the LHTES can be achieved by addition of a storage unit, respectively, in a series or parallel configuration.

### 2.5 Conclusions

We present a methodology to design optimized high-temperature latent heat thermal energy storage (LHTES) units, employing foams as a means to enhance the convective heat transfer between the phase change medium (PCM) and the heat transfer fluid (HTF). A parallel configuration of the encapsulated PCM and the HTF channel was chosen, where the flow channel area was filled with ceramic foam. The design procedure was based on three performance metrics, 1) an exergetic efficiency targeting of 0.95, 2) a required discharging time of 1 h, and 3) an LHTES unit sizing with maximized energy density and effectiveness.

A systematic parametric study was conducted using three input design variables: encapsulation length and diameter, and pore diameter of the foam. The behavior of the storage units was assessed in an analytical-numerical procedure and the energy density and effectiveness of the system were obtained as the output responses. It was demonstrated that for storage units without porous medium, effectiveness values as large as 0.9 could be achieved in units with small encapsulation diameters ( $\sim 5\text{-}10\text{mm}$ ). However as the encapsulation size increased, larger amount of heat was required to be discharged and the effectiveness decreased, indicating a need for enhanced heat transfer by, for example, porous structures. The study then focused on foam-enhanced storage units with larger encapsulation diameters (ranging between 20-100 mm). Such dimensions are more practical and easier to manufacture. The results confirmed that the use of enhanced surfaces in the form of porous foam (fin-equivalent) enabled the design of practical LHTES units with effectiveness as large as 0.95 and energy densities as large as  $810\text{ MJ/m}^3$ . Increasing the encapsulation diameter diminished the energy density and the effectiveness, while increasing the encapsulation length or decreasing the foam's pore diameter decreased the LHTES unit's packing factor ( $\text{PF} = \text{ratio of the PCM volume to the total volume of the storage unit}$ ). Therefore, a trade-off between performance specifications (energy density, effectiveness, PF) and manufacturability of the LHTES unit is required.

We suggested two optimization cases to provide guidance for optimal LHTES sizing. Each optimization case accounted for specified constraints and requirements. A multi-criteria optimization study was performed using surrogate models, which were developed based on the solution of the FE models. The optimization resulted in the following unit and porous media dimensions and resulting performances:

1.  $d_{\text{enc}}=40.0$  mm,  $L_{\text{enc}}=200.0$  mm,  $d_p=1.87$  mm resulting in  $\epsilon = 0.89$  and  $w = 672.1$  [MJ]/m<sup>3</sup>
2.  $d_{\text{enc}}=45.8$  mm,  $L_{\text{enc}}=795.5$  mm,  $d_p=3.93$  mm resulting in  $\epsilon = 0.90$  and  $w = 280.2$  [MJ]/m<sup>3</sup>

where case 1 optimized for performance only, while case 2 accounted for manufacturability limitations. The optimal cases indicated that the proposed approach allows for the design of LHTES units with competitive energy density and large effectiveness [28], [29]. A validation of the optimization results was done by performing FE simulations of the models with the predicted design factors. For these models, the comparison between predictions and FE simulations showed a maximum deviation of 6.4%, indicating that the proposed approach is accurate to guide the design of LHTES units. The in-series or in-parallel arrangement of multiple, optimized LHTES units into a complete LHTES system provides a straightforward way to achieve desired discharging times and system power.

### 2.6 References

- [1] M. Medrano, A. Gil, I. Martorell, X. Potau, and L. F. Cabeza, “State of the art on high-temperature thermal energy storage for power generation. Part 2—Case studies,” *Renew. Sustain. Energy Rev.*, vol. 14, no. 1, pp. 56–72, Jan. 2010.
- [2] S. D. Sharma and K. Sagara, “Latent Heat Storage Materials and Systems: A Review,” *Int. J. Green Energy*, vol. 2, no. 1, pp. 1–56, Jan. 2005.
- [3] S. Almsater, W. Saman, and F. Bruno, “Performance enhancement of high temperature latent heat thermal storage systems using heat pipes with and without fins for concentrating solar thermal power plants,” *Renew. Energy*, vol. 89, pp. 36–50, Apr. 2016.
- [4] M. Johnson, J. Vogel, M. Hempel, A. Dengel, M. Seitz, and B. Hachmann, “High Temperature Latent Heat Thermal Energy Storage Integration in a Co-gen Plant,” *Energy Procedia*, vol. 73, pp. 281–288, Jun. 2015.
- [5] L. Fan and J. M. Khodadadi, “Thermal conductivity enhancement of phase change materials for thermal energy storage: A review,” *Renew. Sustain. Energy Rev.*, vol. 15, no. 1, pp. 24–46, Jan. 2011.
- [6] F. Agyenim, N. Hewitt, P. Eames, and M. Smyth, “A review of materials, heat transfer and phase change problem formulation for latent heat thermal energy storage systems (LHTESS),” *Renew. Sustain. Energy Rev.*, vol. 14, no. 2, pp. 615–628, Feb. 2010.
- [7] S. Kuravi, J. Trahan, D. Y. Goswami, M. M. Rahman, and E. K. Stefanakos, “Thermal energy storage technologies and systems for concentrating solar power plants,” *Prog. Energy Combust. Sci.*, vol. 39, no. 4, pp. 285–319, Aug. 2013.
- [8] N. Maruoka and T. Akiyama, “Exergy recovery from steelmaking off-gas by latent heat storage for methanol production,” *Energy*, vol. 31, no. 10, pp. 1632–1642, Aug. 2006.
- [9] T. Nomura *et al.*, “Microencapsulated phase change materials with high heat capacity and high cyclic durability for high-temperature thermal energy storage and transportation,” *Appl. Energy*, vol. 188, pp. 9–18, Feb. 2017.
- [10] B. Cárdenas and N. León, “High temperature latent heat thermal energy storage: Phase change materials, design considerations and performance enhancement techniques,” *Renew. Sustain. Energy Rev.*, vol. 27, pp. 724–737, Nov. 2013.
- [11] K. Nithyanandam and R. Pitchumani, “Computational Studies on Metal Foam and Heat Pipe Enhanced Latent Thermal Energy Storage,” *J. Heat Transf.*, vol. 136, no. 5, pp. 051503–051503–10, Feb. 2014.

- [12] R. M. Montañés, J. Windahl, J. Pålsson, and M. Thern, “Dynamic Modeling of a Parabolic Trough Solar Thermal Power Plant with Thermal Storage Using Modelica,” *Heat Transf. Eng.*, vol. 39, no. 3, pp. 277–292, Feb. 2018.
- [13] D. Farkas and C. E. Birchenall, “New eutectic alloys and their heats of transformation,” *Metall. Trans. A*, vol. 16, no. 3, pp. 323–328, Mar. 1985.
- [14] E. Rezaei, S. Haussener, S. Gianella, and A. Ortona, “Early-stage oxidation behavior at high temperatures of SiSiC cellular architectures in a porous burner,” *Ceram. Int.*, vol. 42, no. 14, pp. 16255–16261, Nov. 2016.
- [15] A. Ortona *et al.*, “SiSiC Heat Exchangers for Recuperative Gas Burners with Highly Structured Surface Elements,” *Int. J. Appl. Ceram. Technol.*, vol. 11, no. 5, pp. 927–937, Sep. 2014.
- [16] İ. Dinçer and M. Rosen, *Thermal energy storage: systems and applications*, 2nd ed. Hoboken, N.J.: Wiley, 2011.
- [17] L. Geissbühler, M. Kolman, G. Zanganeh, A. Haselbacher, and A. Steinfeld, “Analysis of industrial-scale high-temperature combined sensible/latent thermal energy storage,” *Appl. Therm. Eng.*, vol. 101, pp. 657–668, May 2016.
- [18] “SunShot vision study.” February 2012. SunShot, Energy Efficiency and Renewable Energy, U.S. Department of Energy; 2012. NREL Report No. BK5200e47927; DOE/GO-102012-3037, <http://www.solar.energy.gov/pdfs/47927.pdf> [accessed July 2019].
- [19] M. K. Rathod and J. Banerjee, “Thermal performance enhancement of shell and tube Latent Heat Storage Unit using longitudinal fins,” *Appl. Therm. Eng.*, vol. 75, pp. 1084–1092, Jan. 2015.
- [20] R. K. Shah and A. L. London, *Laminar flow forced convection in ducts: a source book for compact heat exchanger analytical data*. New York: Academic Press, 1978.
- [21] A. Bejan, “Convection in Porous Media,” in *Convection Heat Transfer*, John Wiley & Sons, Inc., 2013, pp. 537–605.
- [22] M. F. Modest, *Radiative Heat Transfer*, 3 edition. New York: Academic Press, 2013.
- [23] B. Dietrich, “Pressure drop correlation for ceramic and metal sponges,” *Chem. Eng. Sci.*, vol. 74, no. Supplement C, pp. 192–199, May 2012.
- [24] B. Dietrich, “Heat transfer coefficients for solid ceramic sponges – Experimental results and correlation,” *Int. J. Heat Mass Transf.*, vol. 61, pp. 627–637, Jun. 2013.

- [25] A. Akolkar and J. Petrasch, “Tomography based pore-level optimization of radiative transfer in porous media,” *Int. J. Heat Mass Transf.*, vol. 54, no. 23–24, pp. 4775–4783, Nov. 2011.
- [26] C. Bonacina, G. Comini, A. Fasano, and M. Primicerio, “Numerical solution of phase-change problems,” *Int. J. Heat Mass Transf.*, vol. 16, no. 10, pp. 1825–1832, Oct. 1973.
- [27] S. Haussener, “Tomography-based determination of effective heat and mass transport properties of complex multi-phase media,” Diss., Eidgenössische Technische Hochschule ETH Zürich, Nr. 19365, 2010, 2010.
- [28] H. Chen, T. N. Cong, W. Yang, C. Tan, Y. Li, and Y. Ding, “Progress in electrical energy storage system: A critical review,” *Prog. Nat. Sci.*, vol. 19, no. 3, pp. 291–312, Mar. 2009.
- [29] X. Luo, J. Wang, M. Dooner, and J. Clarke, “Overview of current development in electrical energy storage technologies and the application potential in power system operation,” *Appl. Energy*, vol. 137, pp. 511–536, Jan. 2015.



## 3 Geometric design of cellular solids

### 3.1 Introduction<sup>1</sup>

Cellular structures exist in different forms in the nature [2]. Mimicking their morphology, nowadays polymeric, metallic and ceramic foams are widely used for different applications. Manufacturing technologies, emerged in the last decade, have enabled the production of structures with designed morphologies [3]–[5]. 3D printing has made it possible to fabricate complex shapes via a more economic procedure than the traditional approaches such as machining and molding. Therefore, the idea of using engineered structures became more feasible. The design of porous structures was further developed, motivated from the idea of fabricating pieces with adjustable effective properties, directly from computer-aided design (CAD) models.

The idea of using lattice structures became more popular thanks to the model of Ashby and Gibson [6]. They simplified the structure of random foams by assuming that each cell of the foam has a cubic unit-cell. Lattice structures, in particular cube cells, were initially introduced in literature to explain the complicated behavior of the foams, by analytical characterization of their pressure drop, heat and mass transfer, and stiffness [7]–[9]. Open-cell foams were later described mainly by more representative unit-cells such as tetrakaidecahedron and Weaire-Phelan's [10]. By further development of additive manufacturing techniques in the last years, the cellular solids with engineered morphologies have received considerable attention. It is shown that proper design of the morphology can results in structures with tailored properties for specific applications [11]–[13].

Such specifically designed structures contain large numbers of geometrical details, which is not foreseen in the commercial CAD packages that use the classical design approaches [14].

---

<sup>1</sup> The content of this section has been partly published by Alberto Ortona and Ehsan Rezaei in *Advances in Science and Technology* (2014) [1]

Therefore, the classical CAD tools are not well adopted for quick and efficient design of the lattice structures. New methodologies and tools are required. In this chapter, we propose alternative approaches to design porous parts with various unit-cell morphologies and a fast turnover.

### 3.2 Structured lattice design

There are various unit-cells with periodic boundaries that can be packed to fill the space and form a lattice structure. The lattice can be made of a polyhedron of choice (such as cubic, dodecahedron, etc.) or a combination of them (such as Weaire-Phelan and octet-truss). In the simplest form, a unit-cell can be described by the position of its nodes and the strut connections. Replicating the unit-cell in different directions can then generate a lattice structure.

An in-house 3D numerical tool was developed in Matlab, which contained a library of several unit-cells, namely cube, rotated cube, hexagonal, Octet-truss, tetrakaidecahedron and Weaire-Phelan. The desired lattice is selected and replicated in the space, forming datasets containing positions of the nodes and the connections between them (the struts). It is then possible to cut the produced lattice (which is in the form of a block) into the desired shape. A drawback of this approach is the emergence of free struts on the boundaries after cutting the lattice (Figure 3.1 (a)), which can be undesirable for manufacturing and handling of the samples. These free struts were closed by further development of the design tool. Each set of points belonging to a clipped unit-cell on the boundaries (at the end of the free struts) were identified and connected to each other by finding a convex hull containing those points. Figure 3.1 (b-d) depicts three lattice structures generated by this approach with closed boundary struts. The freeware gnuplot [15] and POV-Ray ray tracing tool [16] were used for the visualization of the generated lattices.

The produced nodes and struts matrices were then converted into a step file. The step file contained a set of spheres (for each node) and cylinders (for each strut) with diameters that could be adjusted individually. Such a step file can be easily imported in to a commercial CAD software for numerical simulations or production of the lattices.

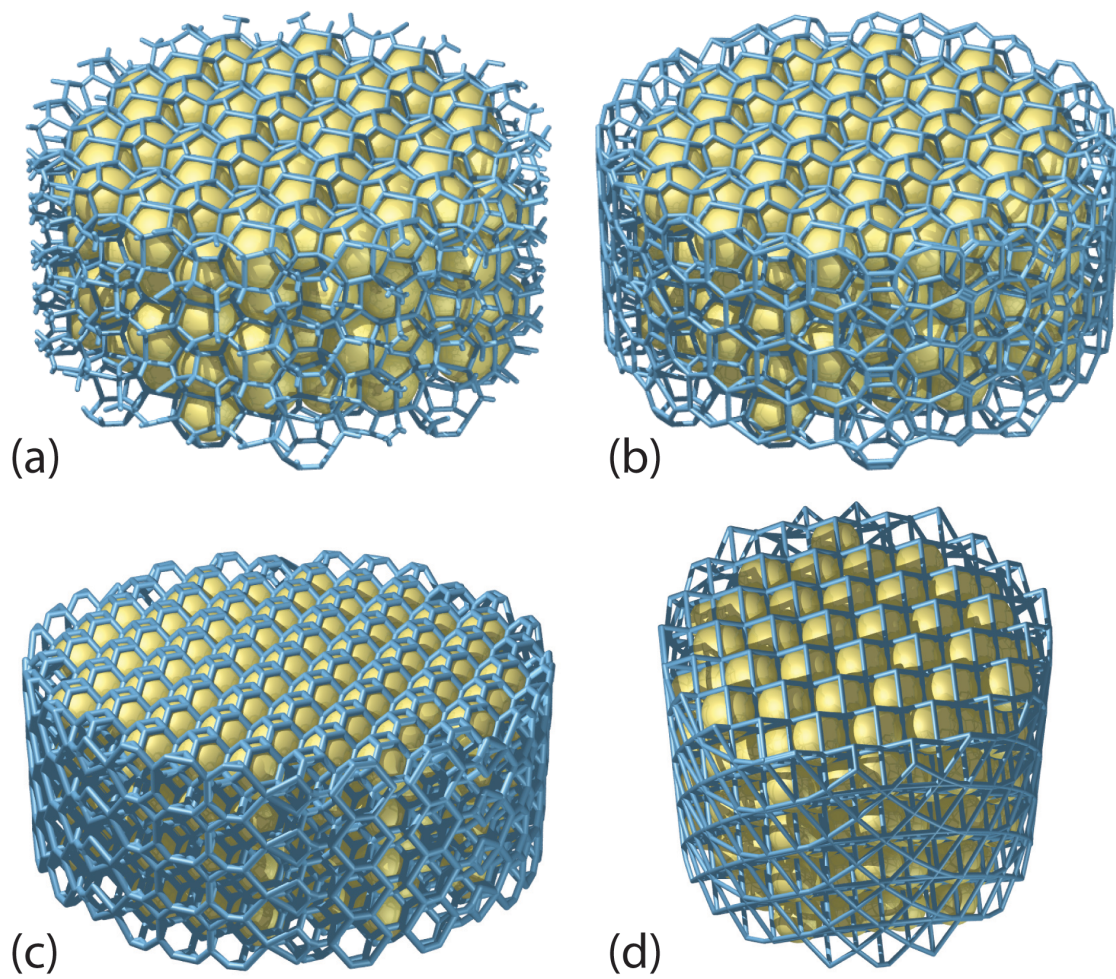


Figure 3.1. (a) Tetrakaidecahedron with open struts at the boundary, (b) Tetrakaidecahedron, (c) Weaire-Phelan and (d) rotated cubic lattice with closed struts at the boundary. In the picture, the cells are filled with yellow spheres for better visibility of the structure.

### 3.3 Unstructured lattice design

In many cases, an unstructured arrangement of the unit-cells is preferred in order to design lattices with heterogeneities such as variable cell size and orientation. Traditionally hexahedral and tetrahedral mesh elements have been used for discretization of numerical domains in computer simulations [17]. Extracting the edges from an unstructured mesh can result in an equivalent unstructured lattice in a simple cubic or tetrahedral form. Extending this approach, one can extract the nodes and element connections from an unstructured hexahedral mesh and map a desired periodic unit cell into each mesh element. Any unit-cell with a cubic symmetry can be employed by this approach. Figure 3.2 shows some examples of the unit-cells with cubic symmetry.

Following this idea, an in-house 3D Matlab tool was developed to receive a mesh file as the input and generate unstructured lattice structures with a certain unit cell as the output. A hexahedral mesh of the part (which can be generated by a commercial software) can be used, onto which the scaled unit cell is mapped. Each strut diameter can be adjusted individually and different unit cells may be used, even for a single part. This allows generating unstructured lattices with variable unit cells and variable strut diameters.

Figure 3.3 demonstrates a simple example of a ring mesh with hexahedral elements, which is fed to the developed design tool as the input. Octet-truss and tetrakaidecahedron structures are synthesized and the results are converted into a step file containing spheres in place of each nodal point and cylinders presenting the struts of the lattice. The output step file can be then easily used for computer simulations or converted to an STL format for the 3D printing. An example of creation of lattices in complex forms with variable strut diameters is presented in Figure 3.4. The generated cubic, tetrakaidecahedron and octet-truss lattice structures in Matlab are shown in Figure 3.4 (a-c). These structures were then imported into Rhinoceros (McNeel, Seattle, US) with the Grasshopper plug-in. The final geometries with variable strut diameters are made of triangular meshes, created using Cocoon add-on, which uses a direct implementation of the Marching Cubes algorithm [18].

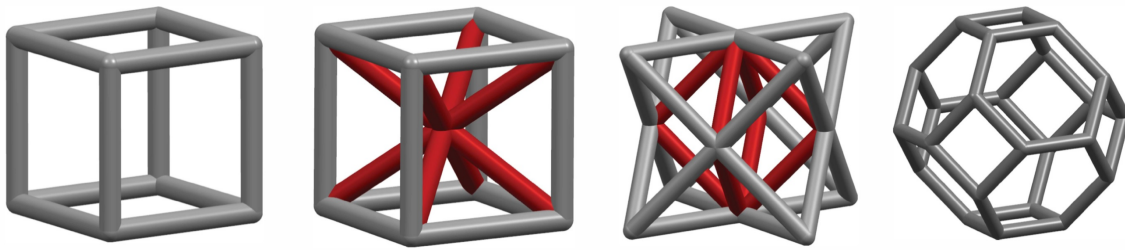


Figure 3.2. Unit cells with cubic symmetry: cube, body centered cube, octet-truss and tetrakaidecahedron.

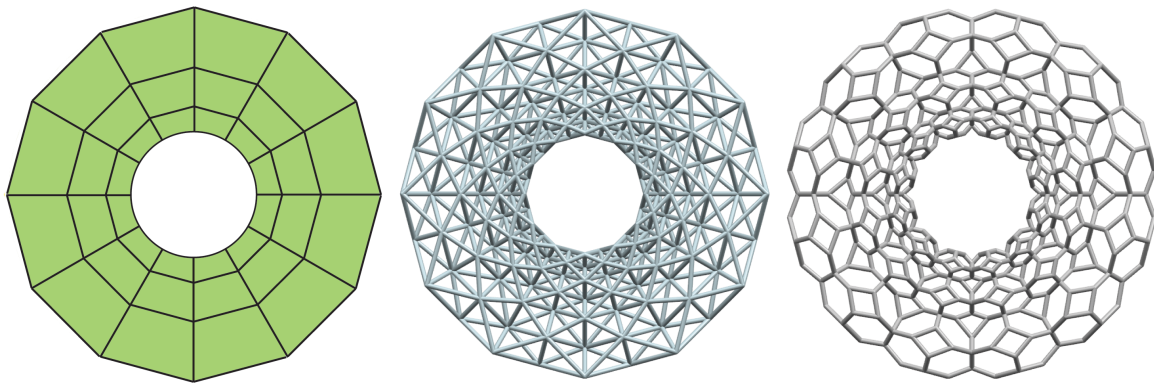


Figure 3.3. From left to right: hexahedral mesh with a radial growth rate of 1.5, used as the input for the code, generated CAD model with octet-truss unit-cells, and generated CAD model with tetrakaidecahedron unit-cells.

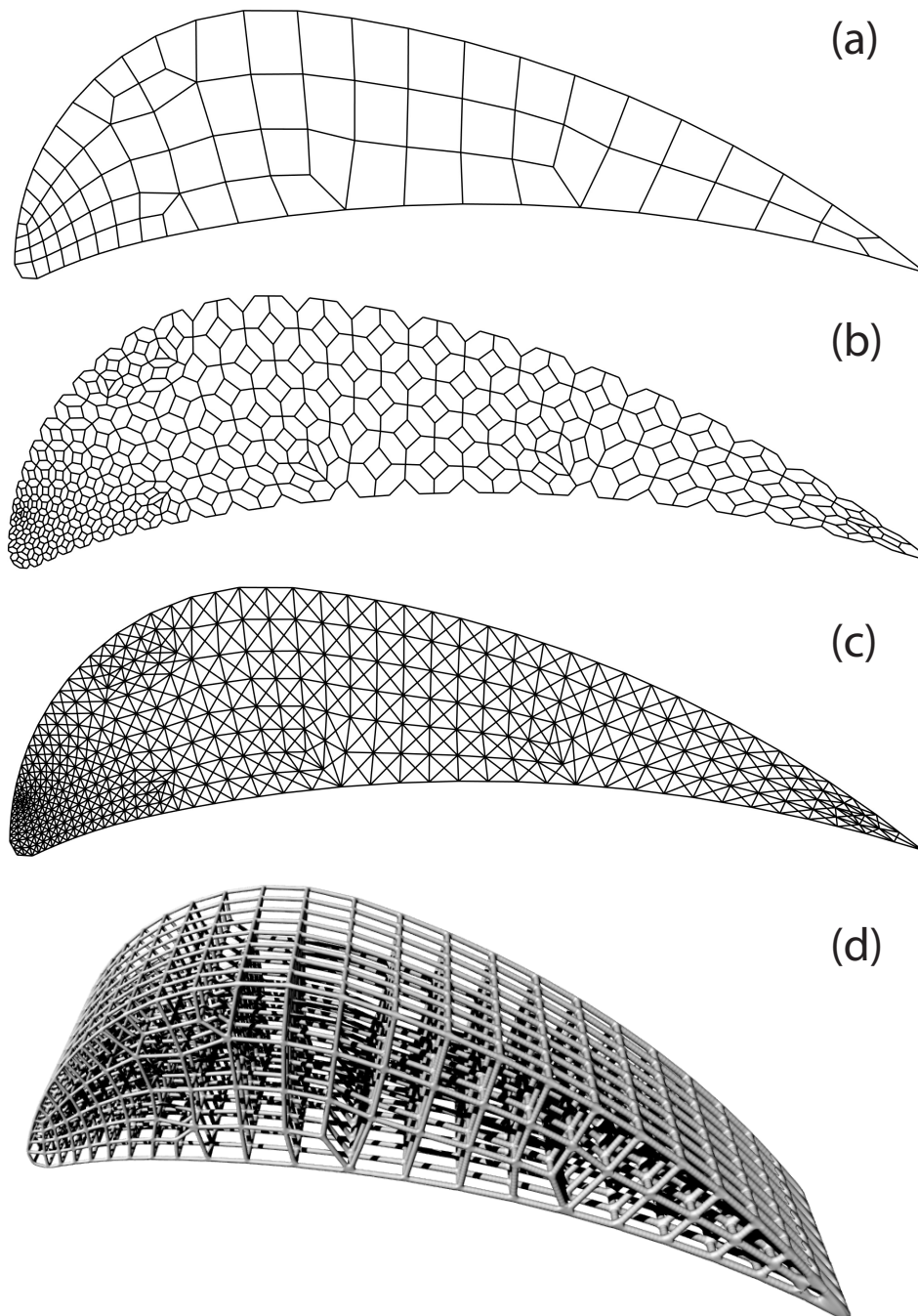


Figure 3.4. 3D unstructured lattices in the form of an airfoil and variable cell sizes with (a) cubic, (b) tetrakaidecahedron and (c) octet-truss unit-cells. (d) Isometric view of the CAD model of the airfoil with cubic unit-cells and variable strut diameters.

### 3.4 Voronoi-based design

Voronoi structures are obtained by partitioning space into zones based on distance to a specific set of points. There are several algorithms to obtain Voronoi diagrams [19]–[21]. In order to create a Voronoi tessellation, a set of seed points are first populated within the desired enclosure. Based on these points, the space is then partitioned into small cells. Each cell contains the space around a seed point that is closer to that seed than any other one. Voronoi tessellations are widely used to describe the morphology of the cellular structures. If they are created based on random seed points, they can represent the microstructural variability and irregularities in the open cell foams. In this section, we used Rhinoceros with grasshopper plug-in, for the implementation of Voronoi tessellations.

The polyhedral structure generated by Voronoi depends on the locations of the seed points. Repetitive seed points can result in repetitive lattice structures. This can be a basis to generate structures using Voronoi algorithms. Figure 3.5 displays some possible lattice structures created with different input seeds. The flexibility of Voronoi tessellation can be employed to obtain regular lattices in complex shapes or even as a means to combine different structures together. Figure 3.6 shows a 2D representation of a multi-lattice produced by this idea. The lattice contains a random Voronoi attached to quad, hexagonal and rotated quad lattice.

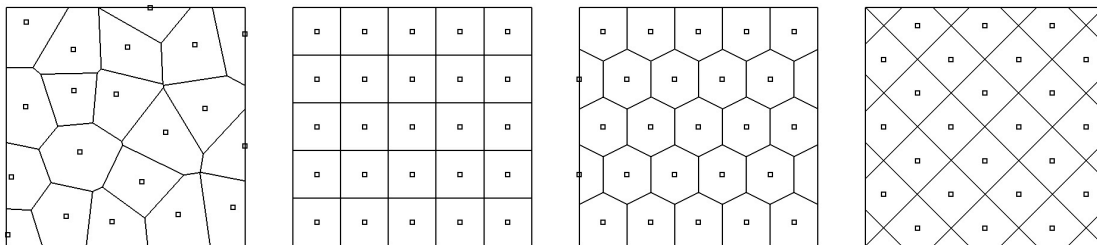


Figure 3.5. 2D representation of the generation of a Voronoi from different input seed points. From left to right: random, quad, hexagonal and rotated quad lattices.



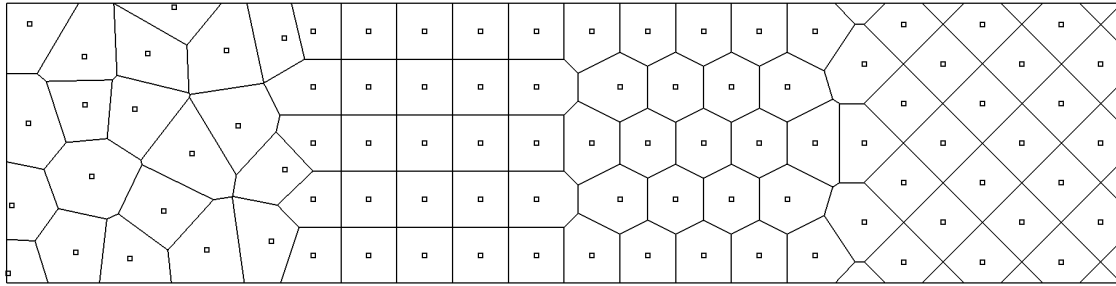


Figure 3.6. 2D representation of a multi-lattice structure consisting of random Voronoi, quad, hexagonal and rotated quad cells.

Extending this approach for 3D Voronoi diagrams, we obtained cubic, rotated cubic, hexagonal and tetrakaidecahedron lattice structures. Figure 3.7 exemplifies 3D multi-lattice consisting of a combination of rotated cube, cube, hexagon and random Voronoi cells, which are attached to a hexagonal honeycomb. The algorithm used to create such a structure is shown in Figure 3.8. Depending on the desired structure, the points are populated in the space within a certain domain. The points and geometries are all united and a final Voronoi algorithm is used to create the whole structure at once. The created Voronoi structure is then decomposed to obtain the structure lines and surfaces (in case of a honeycomb) as the output. These edges and surfaces were then used to form CAD models with STL format, for 3D printing.



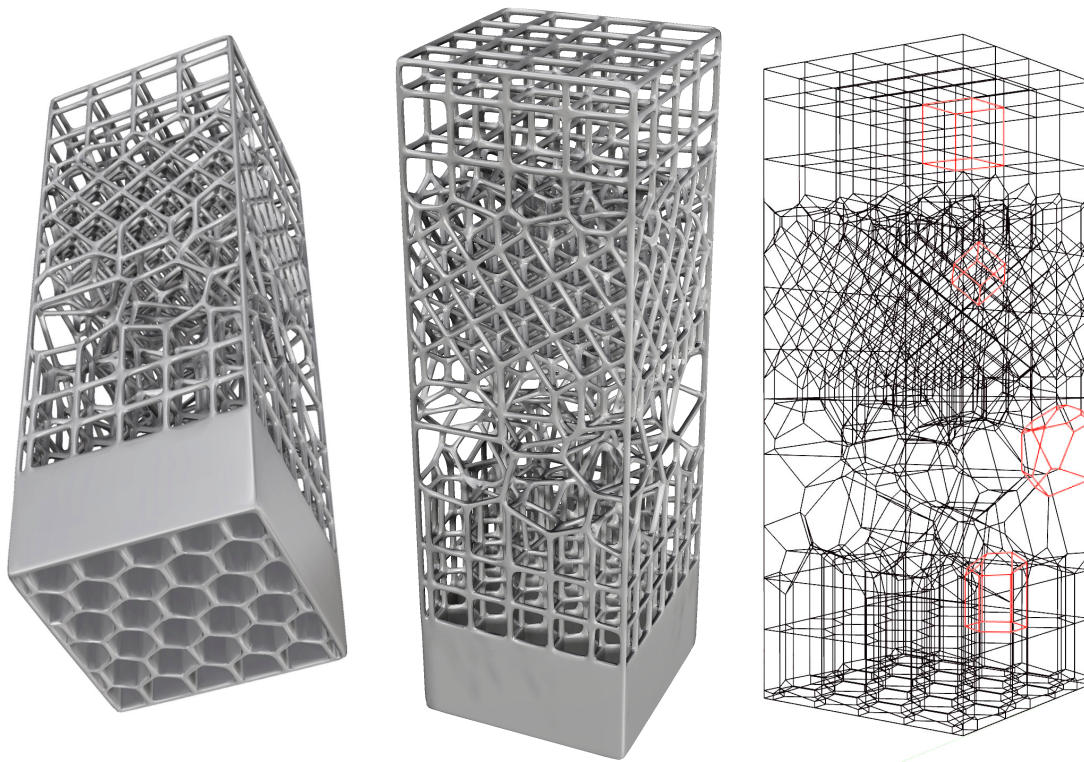


Figure 3.7. Different views of a Voronoi-based structure as a combination of hexahedral, cubic, rotated cube and random cells (shown in red) attached to a hexahedral honeycomb.

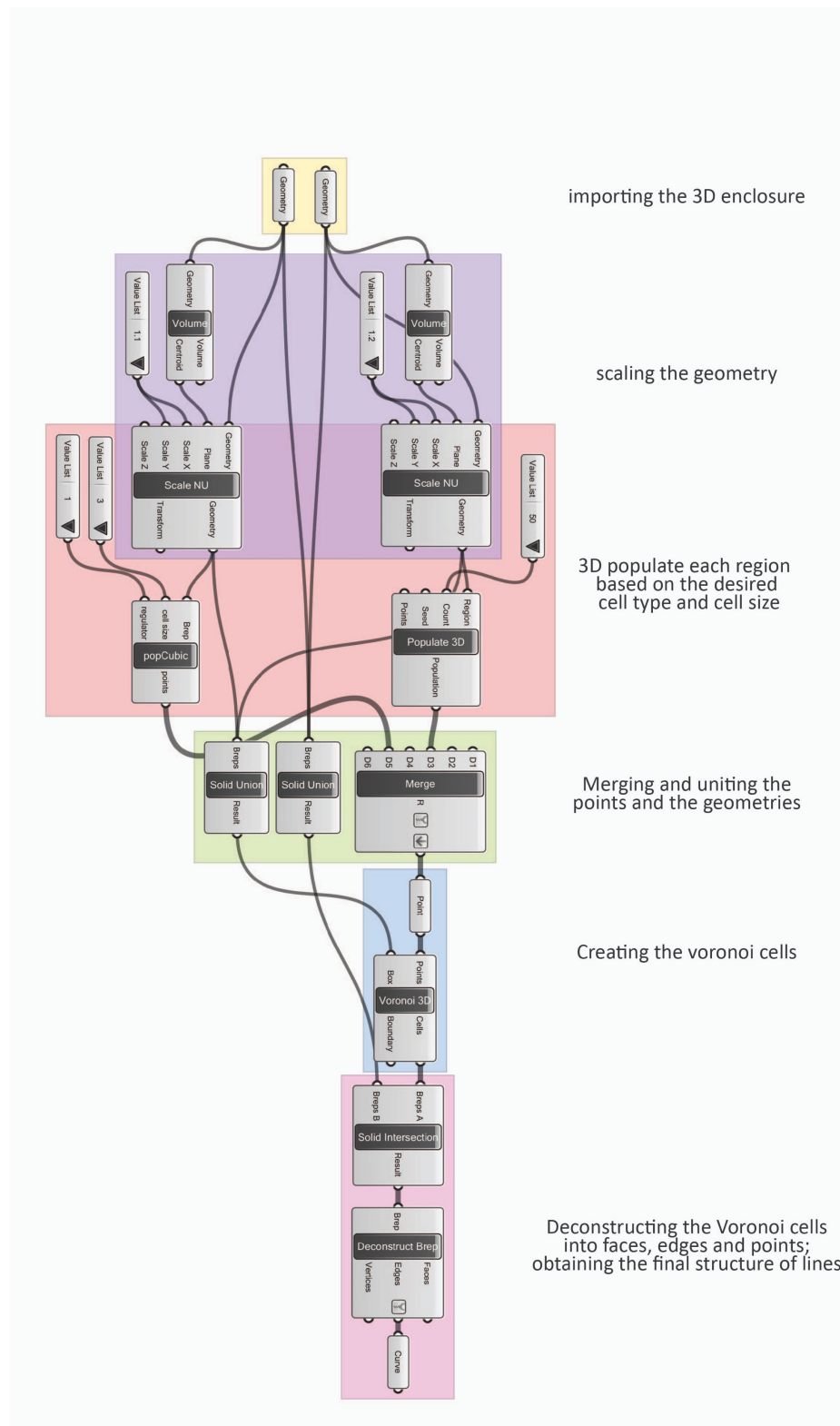


Figure 3.8. The Grasshopper flowchart for creating multi-lattice structures.

### **3.5 Conclusions**

Due to the large number of geometrical features presented in the structure of cellular solids, alternative design approaches are required to provide platforms able to create geometries that can be used for both, computer simulations and additive manufacturing. This chapter presents three alternative design methods to create cellular structures with regular and irregular configurations. The tools developed here, were used to design the samples in this thesis and other projects [22]–[26].

The first approach is based on the creation of a desired unit-cell and its spatial replication within a geometrical enclosure followed by cutting the struts that “fall out” of the enclosure boundaries. This approach, while being simple, provided the tool used for creation of most of the specimens used in this thesis. It is an ideal tool for generation of regular lattices in simple forms such as a cylinder for heat exchangers or gas filters. However, it lacks the flexibility to create structures with variable cell sizes, variable unit-cells, or complex shapes.

The second approach is developed in order to create unstructured lattices within complex enclosures. The idea is based on mapping lattices with cubic symmetry within hexahedral mesh elements. The developed design tool imports a part meshed by commercial software, and creates unit-cells within each hexahedral mesh element. The developed numerical tool can generate lattices with variable cell size within any complex shape. However, it only can use unit-cells with cubic symmetry. Furthermore, the mesh generation must be carefully performed in order to avoid elements with large distortions.

The third approach is based on the creation of Voronoi structures with different input seed points. It is demonstrated that using patterned seed points for a Voronoi algorithm, cubic, tetrakaidecahedral and hexagonal lattices can be generated in any desired direction. This tool provides a flexible way to design pieces consisting of different lattice types, in different orientations, and with variable cell sizes. It can join two lattices to each other, by creation of a Voronoi-based mid-layer between them. However, the approach is limited to certain unit-cells. A further development of the tool is possible in order to combine this tool with the second approach to include further unit-cells with cubic symmetry.

### 3.6 References

- [1] A. Ortona and E. Rezaei, “Modeling the Properties of Cellular Ceramics: From Foams to Lattices and Back to Foams,” *Adv. Sci. Technol.*, vol. 91, pp. 70–78, Oct. 2014.
- [2] G. Mayer and M. Sarikaya, “Rigid biological composite materials: Structural examples for biomimetic design,” *Exp. Mech.*, vol. 42, no. 4, pp. 395–403, Dec. 2002.
- [3] A. Ortona, C. D’Angelo, S. Gianella, and D. Gaia, “Cellular ceramics produced by rapid prototyping and replication,” *Mater. Lett.*, vol. 80, pp. 95–98, Aug. 2012.
- [4] J. W. Halloran, “Ceramic Stereolithography: Additive Manufacturing for Ceramics by Photopolymerization,” *Annu. Rev. Mater. Res.*, vol. 46, no. 1, pp. 19–40, 2016.
- [5] J. T. Muth, P. G. Dixon, L. Woish, L. J. Gibson, and J. A. Lewis, “Architected cellular ceramics with tailored stiffness via direct foam writing,” *Proc. Natl. Acad. Sci.*, p. 219, Feb. 2017.
- [6] L. J. Gibson and M. F. Ashby, *Cellular Solids: Structure and Properties*. Cambridge University Press, 1999.
- [7] A. G. Evans, J. W. Hutchinson, and M. F. Ashby, “Cellular metals,” *Curr. Opin. Solid State Mater. Sci.*, vol. 3, no. 3, pp. 288–303, Jun. 1998.
- [8] L. Giani, G. Groppi, and E. Tronconi, “Mass-Transfer Characterization of Metallic Foams as Supports for Structured Catalysts,” *Ind. Eng. Chem. Res.*, vol. 44, no. 14, pp. 4993–5002, Jul. 2005.
- [9] M. Lacroix, P. Nguyen, D. Schweich, C. Pham Huu, S. Savin-Poncet, and D. Edouard, “Pressure drop measurements and modeling on SiC foams,” *Chem. Eng. Sci.*, vol. 62, no. 12, pp. 3259–3267, Jun. 2007.
- [10] J. T. Richardson, Y. Peng, and D. Remue, “Properties of ceramic foam catalyst supports: pressure drop,” *Appl. Catal. Gen.*, vol. 204, no. 1, pp. 19–32, Nov. 2000.
- [11] Murr L. E. *et al.*, “Next-generation biomedical implants using additive manufacturing of complex, cellular and functional mesh arrays,” *Philos. Trans. R. Soc. Math. Phys. Eng. Sci.*, vol. 368, no. 1917, pp. 1999–2032, Apr. 2010.
- [12] V. S. Deshpande, M. F. Ashby, and N. A. Fleck, “Foam topology: bending versus stretching dominated architectures,” *Acta Mater.*, vol. 49, no. 6, pp. 1035–1040, Apr. 2001.

- [13] P. Wang, J. B. Li, K. Vafai, L. Zhao, and L. Zhou, “Thermo-fluid optimization of a solar porous absorber with a variable pore structure,” *J. Sol. Energy Eng.*, vol. 139, no. 5, pp. 051012-051012–5, Aug. 2017.
- [14] H. Wang, Y. Chen, and D. W. Rosen, “A Hybrid Geometric Modeling Method for Large Scale Conformal Cellular Structures,” in *Volume 3: 25th Computers and Information in Engineering Conference, Parts A and B*, Long Beach, California, USA, 2005, vol. 2005, pp. 421–427.
- [15] T. Williams and C. Kelley, “GNUplot: an interactive plotting program,” <http://www.gnuplot.info> 1998.
- [16] “POV-Ray,” Persistence of Vision Pty. Ltd., Williamstown, Victoria, Australia, <http://www.povray.org/>.
- [17] D. S. H. Lo, *Finite Element Mesh Generation*. CRC Press, 2015.
- [18] P. Bourke, “Polygonising a scalar field,” <http://paulbourke.net/geometry/polygonise> 1994.
- [19] S. Fortune, “A sweepline algorithm for Voronoi diagrams,” *Algorithmica*, vol. 2, no. 1, p. 153, Nov. 1987.
- [20] J. Martínez, J. Dumas, and S. Lefebvre, “Procedural voronoi foams for additive manufacturing,” *ACM Trans. Graph.*, vol. 35, no. 4, pp. 1–12, Jul. 2016.
- [21] D.-M. Yan, W. Wang, B. Lévy, and Y. Liu, “Efficient computation of clipped Voronoi diagram for mesh generation,” *Comput.-Aided Des.*, vol. 45, no. 4, pp. 843–852, 2013.
- [22] A. Szczurek *et al.*, “Carbon periodic cellular architectures,” *Carbon*, vol. 88, pp. 70–85, Jul. 2015.
- [23] M. Aronovici *et al.*, “Heat and Mass Transfer in Ceramic Lattices During High-Temperature Oxidation,” *J. Am. Ceram. Soc.*, vol. 98, no. 8, pp. 2625–2633, Aug. 2015.
- [24] Y. S. Montenegro Camacho *et al.*, “Development of a robust and efficient biogas processor for hydrogen production. Part 1: Modelling and simulation,” *Int. J. Hydrog. Energy*, vol. 42, no. 36, pp. 22841–22855, Sep. 2017.
- [25] M. Pelanconi, M. Barbato, S. Zavattoni, G. L. Vignoles, and A. Ortona, “Thermal design, optimization and additive manufacturing of ceramic regular structures to maximize the radiative heat transfer,” *Mater. Des.*, vol. 163, p. 107539, Feb. 2019.
- [26] G. Bianchi, S. Gianella, and A. Ortona, “Design and Additive Manufacturing of Periodic Ceramic Architectures,” no. 01, 2017.



## 4 Characterization of pressure drop and convective heat transfer

*The content of this chapter is used for an article by Ehsan Rezaei, Maurizio Barbato, Alberto Ortona and Sophia Haussener, in revision, Sep. 2019.*

### 4.1 Introduction

It is well known that the properties of porous media not only depend on their bulk material properties but also on their microstructure [1]. The traditional production of open-cell porous ceramics results in assemblies of edges (called cell struts) and faces (called cell windows) that form randomly organized cells connected together through open faces [2]. Recently, efforts have been devoted to investigating novel additive manufacturing methodologies to directly or indirectly fabricate ceramic structures [3]–[5]. As a result, researchers have been working on design and characterization of structures with engineered unit-cells, called lattices [6]–[9]. Compared to traditional random foams, lattices produced by additive manufacturing techniques are reproducible and offer more design variability, which can result in structures with tailored properties such as high stiffness/weight ratio [10], zero thermal expansion coefficient [11], and negative Poisson's ratio [12]. However, while the multi-physical behavior of the ceramic foams is extensively investigated, there is a lack of studies on the behavior of lattices and other novel structures.

Porous ceramics are often used in high temperature applications given by their high-temperature stability, their inertness to acidic or base environments, their possibility to withstand oxidative environments, and their relatively high mechanical strength and thermal shock resistance [2], [13]–[15]. Furthermore, they can be manufactured to exhibit high specific surface areas and a percolating fluid phase, making them particularly interesting for

applications including heat exchangers, radiant burners, reformers, solar receivers, or heat storage systems [16]–[19]. The study of the thermal and fluid transport in porous ceramic structures is essential for a subsequent optimization of their application [20], [21].

The heat transfer from the solid phase to a fluid passing through the porous media is often characterized by the volumetric convective heat transfer coefficient. In the literature, two experimental approaches are usually followed for the determination of the volumetric convective heat transfer in porous media. Younis and Viskanta [22] calculated the volumetric convective heat transfer coefficient for different velocities in ceramic foams by passing steam into the cold foam and measuring the transient gas temperature at the outlet. In a different approach, Calmidi and Mahajan [23] investigated aluminium foams by passing cold air into the foams, which were heated by an electric source. They calculated the average convective heat transfer coefficient at different velocities using the steady state temperature readings of the thermocouples. Fuller et al. [24] illustrated that the transient method is a more accurate technique as it excludes the conduction effects on the samples. However, the results of the two methods will converge for thin samples with high thermal conductivities. Various studies used both methods to determine the heat transfer rate in the ceramic foams, however only few correlations have been proposed. Younis and Viskanta [22] investigated the heat transfer in a set of 10-65 PPI alumina and cordierite foams with porosities ranging between 0.83-0.87. They proposed a correlation based on the foam's pore diameter and sample length. Kamiuto and Yee [25] proposed a correlation based on a collection of results from 16 foams reported in literature. Dietrich [26] tested 10-45 PPI foams made of alumina, mullite and oxidic-bonded SiC, with porosities ranging between 0.75-0.85, and proposed a Nusselt-Hagen correlation valid for a large range of Reynolds numbers. Xia et al. [27] proposed their own correlation based on a set of metallic and ceramic foams and performed a comparison between different correlations proposed in the literature. They found a large discrepancy between various correlations that were attributed to different conditions at which the studies were carried on.

The pressure drop within a porous medium has been particularly well studied due to the simplicity and low cost of the measurement procedure. It consists of passing fluid into a duct filled with the porous medium and measuring the pressure at the inlet and outlet of the sample [28]–[31]. The accuracy of this method is high as long as the sample is thick enough or exhibits low permeability. Several groups studied the pressure drop of ceramic or metal foams [29]–[35]. Edouard et al. [36] published a summary of the correlations reported in these studies. Dietrich et al. [28] proposed a correlation based on experiments of different ceramic foams and compared their correlation with large number of experimental data from the literature, demonstrating that their correlation could predict most of the literature values within an error range of  $\pm 40\%$ .



Advances in computational power have allowed advanced numerical characterization of porous structures utilizing their exact microstructures (obtained, for example, by computed tomography and subsequent digitalization through various segmentation approaches) in pore-level simulation to calculate the transport properties and structural parameters [37], [38]. Transport characteristics of regular lattices (such as tetrakaidecahedron and Weaire-Phelan structures) have also been modeled, claiming that they are the closest representative lattices to the structure of the random foams [39], [40].

In the literature, the experimental studies on transport properties have been mainly performed on random foams. To the author's knowledge, there is no study in the literature that systematically analyzes pressure drop and heat transfer behavior of ceramic structures with different unit-cells made by the same manufacturing procedure. This is a particularly important task for the case of SiC-based structures as they have been widely used for high-temperature applications involving fluid flow and heat transfer [16], [17], [19], [41]. Here, we aim at analyzing the effect of the porous medium's unit-cell shape on the transport behavior. For this reason, lattices with three different microstructures are designed and manufactured. A random foam with similar porosity is also produced for comparison. The specimens were used in a combined experimental-numerical approach to quantify their pressure drop and convective heat transfer behavior. The morphology of the produced specimens was characterized and the advantages and disadvantages of the manufacturing technique are briefly discussed. Nusselt correlations are formulated for each specimen and the results are compared with literature.

## **4.2 Samples and the experimental set-up**

### **4.2.1 Fabrication and characterization of the porous specimens**

Lattice structures with three different unit-cells, rotated cube (RC), tetrakaidecahedron (TK), and Weaire-Phelan (WPh), were designed in a cylindrical form with diameter of 20 mm and length of 100 mm. We used an in-house tool (developed in MATLAB R2014a) that generated lattices with a given unit-cell inside a cylindrical enclosure and cropped the cells on the boundary surfaces. The polymeric templates of the designed lattices were fabricated using a commercial 3D-printer (3DLPrinter-HD 2.0, Robot Factory S.r.l., It), with a resolution of 0.01 and 0.05 mm in vertical and horizontal axes, respectively. The printed polymeric structures were then used as the template to manufacture near-net-shape SiSiC lattices by EngiCer SA (Balerna, CH), via the replica technique followed by reactive melt infiltration of silicon. The detailed manufacturing process of the samples is described by Ortona et al. [3]. In addition, SiSiC foams were manufactured by the same procedure utilizing

commercial 5 PPI polyurethane foams as the template. A photo of the final SiSiC pieces is shown in Figure 4.1. The relative density was calculated as the weight of each sample divided by the mass of the bulk material of the same volume. The total porosity was determined based on the calculated relative density. The cell size,  $d_c$ , was defined as the unit-cell length for the lattices and the nominal cell diameter for the random foam. The strut diameter was obtained based on 10 random measurements in the middle of the struts (center location between two strut junctions) on each of the specimens. The lattices were designed with a 5 mm cell length and a 5 PPI (pores per inch, i.e.  $\sim 5$  mm nominal pore diameter) random foam was chosen for comparison. The manufacturing procedure resulted in lattices with 5% shrinkage. An overview of the microstructural properties of the investigated specimens is given in Table 4.1. The specific surface area,  $S_v$  (also called geometric surface area [ $\text{m}^2/\text{m}^3$ ]) is defined as the total surface of the struts per unit volume of each sample. For the lattices, it was calculated by creating CAD models with cell and strut diameters, measured from each manufactured lattice. The specific surface area of the random foam was obtained from a correlation proposed by Inayat et al. [41] for foams with circular struts:

$$S_v = 3 \frac{(1 - \phi)}{d_{st}} \quad (4.21)$$

Table 4.1. Microstructural properties of the four investigated specimens.

ID	Structure	Density [ $\text{kg}/\text{m}^3$ ]	$\phi$ [-]	$d_c$ [mm]	$d_{st}$ [mm]	$S_v$ [ $\text{m}^2/\text{m}^3$ ]
<b>RC</b>	Rotated cube	$578.6 \pm 5.5$	$0.796 \pm 0.008$	$4.75 \pm 0.02$	$1.19 \pm 0.11$	542.85
<b>TK</b>	Tetrakaidecahedron	$540.3 \pm 5.4$	$0.809 \pm 0.009$	$4.75 \pm 0.02$	$0.94 \pm 0.14$	833.26
<b>Foam</b>	Various-polyhedra	$444.6 \pm 4.4$	$0.843 \pm 0.008$	5.08	$1.03 \pm 0.14$	456.40
<b>WPh</b>	Weaire-Phelan	$546.8 \pm 5.4$	$0.807 \pm 0.008$	$4.75 \pm 0.02$	$1.26 \pm 0.17$	745.42

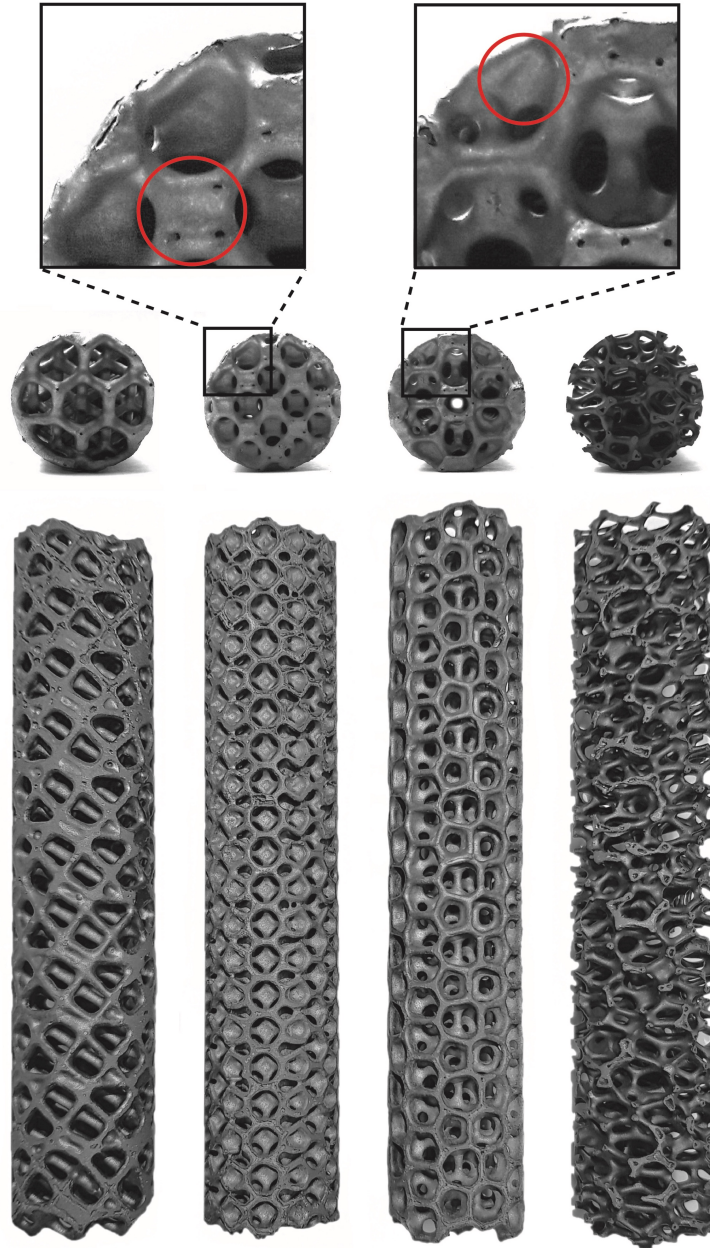


Figure 4.1. Front and top view of cylindrically shaped SiSiC structures (diameter of 20 mm and length of 100 mm). From left to right: RC, TK, WPh lattices, and random foam. The presence of closed cell walls were observed in the manufactured samples, especially in the TK and WPh. Some of these closed cell walls are shown in the magnified section. An example of the closed cells in these two lattices are shown with the red circles in the magnified section.

### 4.2.2 Experimental set-up

A scheme of the test rig used for the measurements of the pressure drop and the volumetric convective heat transfer is shown in Figure 4.2. The air stream was continuously supplied by a compressor, and passed through an air preparation unit comprising pressure regulator, filter and dehydrator sections, in order to decrease the supplied pressure and remove the moisture and contaminants such as oil and dust particles. A commercial mass flow controller (GSC red-y, Vögtlin, CH) was used with an accuracy of  $\pm 0.24\%$ . The mass flow controller works based on the thermal mass flow measurement principle [43], and uses a sealed valve with very low leakage ( $10^{-6}$  mbar l/s He) and fast response time (300 ms) to control the flow rate. The air then entered a calm chamber (in order to damp the possible pressure waves) and an entry pipe of 50 cm length before entering the furnace. A tubular electric furnace (XTUBE series 1600, Xerion, Freiberg, De) was used to heat up the samples. The tube is heated using two U-shaped heating elements (Figure 4.2), each with a diameter of 0.8 cm, that are placed in the middle of the furnace, 6 cm apart from each other. An alumina tube was horizontally fitted in the middle of the furnace, passing through the heating elements and connected to the inlet tube by a water-cooled flange.

The samples were placed in the middle of the alumina tube, wrapped into a thin layer of expanded graphite foil to avoid air bypassing between the sample and the tube. A differential pressure transmitter (DPGM409, Omega Engineering, Inc., US) with working pressure range of 0-2500 Pa and accuracy of 0.08% BSL (best straight line) was used to measure the pressure drops. The temperatures were monitored by several K-type thermocouples, placed on the alumina tube, on the specimens and in the air stream at the inlet and the outlet. All thermocouples were calibrated to have an accuracy of  $\pm 0.4^\circ\text{C}$ . For the measurements of the tube wall temperature,  $T_{\text{wall}}$  in Figure 4.2, seven thermocouples were fixed on the alumina tube in different locations along the tube length, glued to the surface using a high-temperature silicate adhesive (Coltogram 1500, Blattener AG, Zürich, CH) and covered by an alumina felt to decrease the radiation effects. The set-up had a quasi-axis-symmetric configuration, and therefore the temperature was assumed to be uniform around the tube at each axial point. The assumption was ensured in a preliminary test, by measuring the wall temperature difference at upper and lower side of the tube in three points in the axial direction (middle, inlet and outlet sides), which were differing by  $0.5^\circ\text{C}$  at maximum. To determine the lattice temperature, a thermocouple with exposed tips was tightened to a strut, glued and isolated with the silicate adhesive. The inlet temperature was measured by a thermocouple placed in the middle of the duct just before the air enters the alumina tube. To measure the outlet air temperature three thermocouples were fixed on a mounting structure and inserted into the alumina tube. The thermocouples were placed 10 mm behind the porous sample in order to measure the outlet air temperature ( $T_{\text{f,out},i,\text{exp}}$  ( $i$  is the thermocouple number shown in Figure

4.2). One of the three thermocouples was at the center ( $i=2$ ), while the other two were fixed at off-center locations, 5 mm up ( $i=3$ ) and down ( $i=1$ ) from the center. Assuming the thermocouple's bead as a perfect sphere with a diameter of 1 mm and emissivity of 0.9, the fluid temperature measurements were corrected for radiation losses using the bare-bead model [44]. Whitaker's correlation [45] was used to obtain the convective heat transfer coefficient for the flow passing over the sphere. All data were recorded using NI data acquisition modules (NI 9219, NI 9213 and NI 9203, National Instruments, Austin, TX, USA).

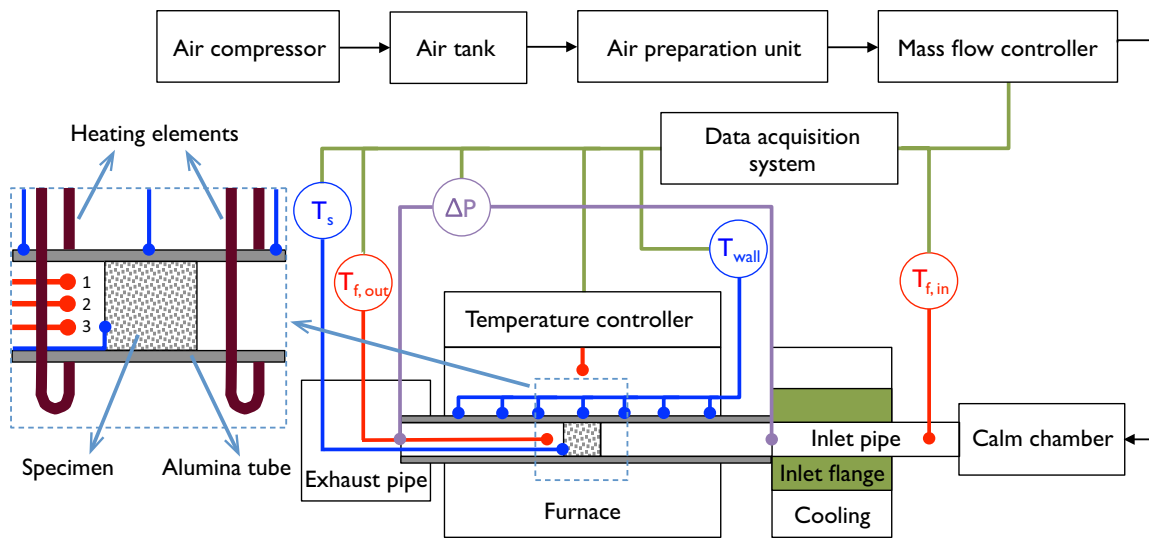


Figure 4.2. Scheme of the test set-up for measurements of pressure drop and convective heat transfer. The cylindrical porous samples are embedded in a cylindrical tube, which is heated in the temperature-controlled electric furnace. The pressure drop sensors (purple lines), the thermocouples placed on the solid parts (blue lines), and the thermocouples to measure the air stream inlet and outlet temperatures (red lines) are shown. The magnified region shows the two U-shaped heating elements that are placed around the tube, and the thermocouples used to measure the temperature of the air stream and the porous specimens, which are placed inside the tube.

### 4.3 Calculation procedure

#### 4.3.1 Pressure drops coefficients

The pressure drop was experimentally measured and used to calculate permeability,  $K$ , and form coefficient,  $C$  (also called Dupuit-Forchheimer coefficient). For each porous structure, two specimens were placed in the middle of the alumina tube, one after the other to form a

200 mm long sample. The desired air mass flow rate was selected and the pressure drop was measured. The experiments were conducted in ambient temperature for different mass flow rates between 2.5 and 50 NL/min, corresponding to superficial velocities ranging between 0.15-2.97 m/s. For an isothermal flow with constant inlet velocity, the Darcy-Forchheimer equation can be written for 1-D domain in a non-dimensional form as [38]:

$$-\frac{\Delta p}{L} \frac{d_c^2}{\mu_f u_f} = \underbrace{\frac{d_c^2}{K}}_a + \underbrace{d_c C}_b \underbrace{\frac{\rho_f u_f d_c}{\mu_f}}_{Re}, \quad (4.22)$$

where  $L$  is the length of the sample. Knowing the non-dimensional pressure drop,  $\Pi$ , for different Reynolds numbers,  $Re$ , the intercept and slope ( $a$  and  $b$  in Eq. 4.22) and consequently  $K$  and  $C$  were calculated by a least-square method.

### 4.3.2 Volumetric heat transfer coefficients

To determine the volumetric convective heat transfer coefficients of the porous samples, a steady state approach was employed. The lattices were cut to obtain samples of 25 mm length and then placed in the middle of the alumina tube. The furnace temperature was fixed to 100 °C and the air at ambient temperature was introduced at the inlet of the alumina tube. The experiments were done for five mass flow rates between 5 and 15 NL/min at ambient temperature, corresponding to the superficial velocities ranging between 0.30-0.89 m/s. For each test, the desired mass flow was set and the temperatures were recorded at steady state condition, reached after about 20 min. The pipe flow Reynolds number,  $Re_{pipe}$ , at the inlet varied between 380-1160, and thus a laminar flow was ensured in the duct. In order to evaluate the convective heat transfer coefficients, an inverse method was used, consisting of comparing the steady state data of the experiments with the numerical predictions and adjusting the volumetric convective heat transfer coefficient (in the simulations) until both agree. The numerical method we used to calculate the heat transfer coefficients is presented in the next section.

### 4.3.3 Computational heat transfer and fluid flow model

The following assumptions and simplifications were made for the computational model: (1) the inlet flow is laminar with a uniform temperature, (2) the porous domain is modeled by two homogenous and isotropic media (solid and fluid), (3) the solid and fluid phases are in

local thermal non-equilibrium (LTNE), (4) the solid phase temperature is considered constant given by the high conductivity of the material and the short sample length, and (5) the buoyancy forces in the fluid are not negligible due to high radial temperature gradients and low fluid velocities.

Brinkman equations with Forchheimer corrections were solved for the porous media, considering a formulation for low Mach number, steady state compressible flow [46]:

$$\nabla \cdot (\rho_f \mathbf{u}_f) = 0 \quad (4.23)$$

$$\begin{aligned} \frac{\rho_f}{\phi^2} (\mathbf{u}_f \cdot \nabla) \mathbf{u}_f = & -\nabla p \\ & + \nabla \cdot \left[ \frac{\mu_f}{\phi} (\nabla \mathbf{u}_f + (\nabla \mathbf{u}_f)^T) - \frac{2}{3} \frac{\mu_f}{\phi} (\nabla \cdot \mathbf{u}_f) \mathbf{I} \right] - \left[ \frac{\mu_f}{K} + \rho_f C |\mathbf{u}_f| \right] \mathbf{u}_f \\ & + \rho_f \mathbf{g} \end{aligned} \quad (4.24)$$

$K$  and  $C$  are independent of the fluid velocity and were calculated directly from the pressure-drop experimental test results (see section 3.1).

The LTNE formulation of the energy equation was solved for the fluid phase in the porous media domain [45]:

$$\rho_f c_{p,f} \mathbf{u}_f \cdot \nabla T_f - \nabla \cdot (\phi \lambda_f \nabla T_f) = h_v (T_s - T_f), \quad (4.25)$$

where  $T$  stands for the intrinsic average of the temperature and  $h_v$  is the volumetric convective heat transfer coefficient ( $h_v = S_v h_{sf}$ ). For the free fluid flow inside the inlet tube, the standard Navier-Stokes and energy equations for a single-phase flow model were used. In all the simulations, the fluid was assumed as ideal gas and its properties were calculated as a function of the local temperature.

#### 4.3.4 Numerical procedure

For every specimen and each mass flow rate, the convective heat transfer coefficient was estimated by solving the numerical model several times until it matched the experimental

steady state fluid outlet temperature data. As this iterative procedure is highly time-consuming, a submodeling technique was implemented so as to reduce the calculation domain in the iterative procedure. A numerical solution for the global model was acquired initially using the entire domain, in which the porous medium was modelled with an initial guess value for the convective heat transfer coefficient. A submodel (indicated by the red rectangle in Figure 4.3) was used for further iterations, which didn't need to again solve the equations for the entry region.

The coupled continuity, momentum and energy equations, formulated in a 3D domain, were solved in Comsol Multiphysics package® (ver. 5.2) interlinked with Matlab. Figure 4.3 displays the computational domain, which consisted of a cylinder with the porous specimen inside. Due to the symmetry only half of the cylinder was investigated. As we accounted for gravity, axis-symmetry was not given.

For the global mode, no slip conditions with fixed temperature on the lateral walls and constant solid temperature for the porous medium were given as boundary conditions. Furthermore, a laminar flow with uniform temperature, and a velocity profile calculated as a function of the mass flow rate and the entrance length, was considered at the inlet. No conductive heat transfer was also applied at the outlet. The outlet pressure was specified as:

$$p_{\text{out}} = p_{\text{atm}} - \rho_f g Z \quad (4.26)$$

The exit tube length (after the porous domain) was chosen long enough to avoid back flow in the outlet. For the submodel, all the boundary conditions are the same as the global model except for the inlet. The solution of the global model was prescribed on the cutting interface as the inlet boundary conditions for the sub-model.

A first order discretization scheme was implemented and the generalized minimal residual (GMRES) iterative solver with a relative tolerance of  $10^{-3}$  was set for the convergence of the solutions. Convergence with this relative tolerance value was ensured by solving for a value of  $10^{-4}$  and comparing temperatures, velocities and pressures. They varied by less than 0.23%. A mesh made of variable non-uniform mesh element sizes was used in the tube's axial direction in order to have finer elements near the inlet, outlet and the porous medium regions. Grid convergence was obtained at about  $9.6 \times 10^5$  and  $4.6 \times 10^5$  cells for the global and the submodels. Mesh convergence was confirmed by doubling the element numbers and comparing temperatures, velocities and pressures, which varied by less than 0.5%.



The numerical procedure used to determine the volumetric convective heat transfer coefficients is as follows:

- 1- The global model is solved using a guess value  $h_v = h_0$
- 2- Two values  $h_0$  and  $h_1 = 1.2h_0$  are used as the initial guess for  $h_v$  in the submodel
- 3- Two solutions are obtained solving the submodel for  $h_0$  and  $h_1$  and the outlet air temperatures at the center location,  $(T_{f,out,2})_{num,h0}$  and  $(T_{f,out,2})_{num,h1}$ , just after the porous medium.
- 4- A new  $h_v$  is estimated as:

$$h_v = \frac{[(T_{f,out,2})_{exp} - (T_{f,out,2})_{num,h0}]}{[(T_{f,out,2})_{num,h1} - (T_{f,out,2})_{num,h0}]} \cdot (h_1 - h_0) + h_0 \quad (4.27)$$

- 5- The new value  $h_v$  is used as  $h_2$  and step 3 and 4 are repeated for  $h_1$  and  $h_2$  instead of  $h_0$  and  $h_1$  obtaining a new  $h_v$ . The same process continues for new values  $h_2$  and  $h_3$  until the last iteration with  $h_{n-1}$  and  $h_n$  where the following criteria is fulfilled and the solution is converged:

$$|(T_{f,out,2})_{num,n} - (T_{f,out,2})_{exp}| < 0.04 \text{ } ^\circ\text{C} \quad (4.28)$$

The threshold value of 0.04 °C in Eq. 4.28 was chosen as 10% of the uncertainty of the thermocouples. Depending on the initial guess, the numerical procedure converged after 6-10 iterations. The deviation of the numerical solution from the experimental temperature values at the three outlet positions was calculated from Eq. 4.29. The deviation was smaller than 0.05 for all the cases.

$$D = \sqrt{\frac{1}{3} \sum_{i=1}^3 \left[ \frac{(T_{f,out,i})_{num} - (T_{f,out,i})_{exp}}{(T_{f,out,i})_{exp}} \right]^2} \quad (4.29)$$

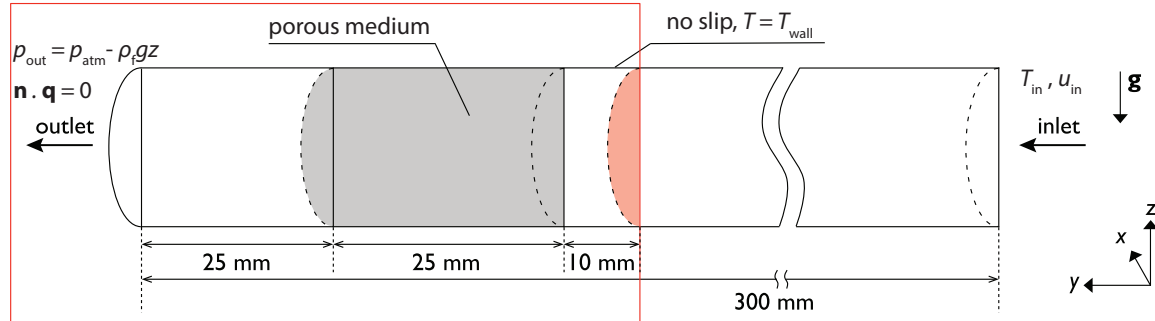


Figure 4.3. Schematic of the numerical domain used when solving the coupled Eqs 4.4 and 4.5. The red rectangle shows the submodel used for the determination of the volumetric convective heat transfer coefficients. The inlet boundary condition of the submodel (red surface) is obtained from the global model solution.

#### 4.3.5 Uncertainty analysis

The uncertainty of the calculated  $K$  and  $C$  is a function of the uncertainties of the air properties, the specimen length, and the measured velocity and pressure values. In all our calculations, the uncertainty of the air properties was not considered and the uncertainty of  $d_c$  was considered negligible. As the experimental values and their uncertainties ( $\sigma_{\Delta p} = 2$  Pa,  $\sigma_L = 1$  mm,  $\sigma_{u_f} = 0.0024 u_f$  m/s) were known, the uncertainty of  $\Pi$  (as defined in Eq. 4.22) was calculated by applying an error propagation analysis:

$$\sigma_{\Pi} = \sqrt{\left(\frac{\partial \Pi}{\partial \Delta p} \sigma_{\Delta p}\right)^2 + \left(\frac{\partial \Pi}{\partial L} \sigma_L\right)^2 + \left(\frac{\partial \Pi}{\partial u_f} \sigma_{u_f}\right)^2}. \quad (4.30)$$

The uncertainty of the Reynolds number was calculated as:

$$\sigma_{\text{Re}} = \sqrt{\left(\frac{\partial \text{Re}}{\partial u_f} \sigma_{u_f}\right)^2}. \quad (4.31)$$

Knowing the values and uncertainties of  $\Pi$  and Re for each test, the parameters  $a$  and  $b$  (and consequently  $K$  and  $C$ ) and their standard errors were obtained using the iterative least squares solutions developed by York et al. [46].

The estimation of the uncertainty of the predicated volumetric convective heat transfer coefficient was not straightforward as the values were obtained through a combined experimental and numerical analysis. A sensitivity analysis of the numerical model was conducted using the uncertainty of the main input parameters. The effect of the measured tube's surface temperature, absolute pressure of the air, and the geometry parameters was assumed negligible. The uncertainty of volumetric convective heat transfer coefficient was calculated by varying three experimental parameters - the outlet air temperature  $(T_{f,out})_{exp}$ , the porous solid temperature, and the air inlet velocity - within their experimental uncertainties ( $\sigma_T = 0.4$  °C,  $\sigma_{u_f} = 0.0024 u_f$  m/s). The sensitivity of the calculations to the three parameters,  $P_i$ , was calculated by:

$$S_{h_v} = \sqrt{\sum_{i=1}^3 \left( \frac{(h_v)_{P_i+\sigma_{P_i}} - (h_v)_{P_i-\sigma_{P_i}}}{2 (h_v)_{P_i}} \right)^2} \quad (4.32)$$

## 4.4 Results and discussion

### 4.4.1 Measured pressure drop

Experimental results expressed as the pressure drop per sample length for various flow rates for the four porous structures are shown in Figure 4.4. The pressure drop increases exponentially when raising the mass flow rate. At low Reynolds numbers (of the order unity), the pressure drop is a linear function of the velocity (Darcy's law). At higher velocities, before entering the turbulence regime, a second-order polynomial model fits the data best, resulting from the dominance of the inertia effects. To determine permeability and form coefficients, we only used the data at  $Re < 250$  to ensure that the flow didn't enter the turbulent regime [47]. Table 4.2 shows the calculated permeability and form coefficients together with their uncertainties. The high values of the coefficient of determination,  $R^2$ , from the linear fitting of Eq. 4.22 suggest that the Darcy-Forchheimer model fits the data well. The uncertainties of  $C$  were lower compared to the ones of  $K$ . This was because of the high uncertainty of the pressure drop measurements at lower velocities, which has a higher contribution to the uncertainty of  $K$  than  $C$ . Figure 4.5 shows the dimensionless pressure gradient with experimental uncertainties as a function of Reynolds number. For the sake of clarity, only the data from WPh lattices and the foam are shown.

Pressure gradients in WPh and TK lattices were 2-3 times higher as in the RC lattice and random foams. As shown in Table 4.1, designed TK and WPh lattices have higher specific

surface area than the other two specimens, which causes higher viscous drag and therefore higher pressure drops. Besides, the morphology of the manufactured lattices is different from their ideal designed shape: the replica process resulted in the agglomeration of material in the strut joints (nodes) during the impregnation of the polymeric template in the ceramic slurry, which led to bigger nodes. Furthermore, during the manufacturing process, the high cohesion forces of the slurry kept a membrane in small windows, resulting in the clogged cell windows, a phenomenon that was mostly observed in the TK and WPh lattices. This was not the case for the RC lattice as the cubic unit-cell contained larger windows. In case of TK, all the square windows in each unit-cell were closed, which accounts for about 29% of the windows. For WPh, counting the closed windows in each periodic section resulted in a total of about 20% closed pores in the structure. A closed pore deviates the fluid flow passage, i.e. increases the tortuosity [48], and also reduces the available cross-sectional area for the fluid to pass. This is probably the main reason for the higher pressure gradients in the TK and WPh samples. The lower pressure-drop values in the random foam (compared to the RC lattice) are attributed to its 4.7% higher porosity and lower specific surface area.

Table 4.2. Permeability and form coefficients and their uncertainties for the four porous specimens.

Sample	$K (\times 10^7 \text{ m}^2)$	$\sigma_K [\%]$	$C (\text{m}^{-1})$	$\sigma_c [\%]$	$R_2$
<b>RC</b>	1.80	34.1	326.1	15.4	0.963
<b>TK</b>	0.75	15.2	814.8	6.5	0.991
<b>Foam</b>	2.20	42.2	270.5	18.4	1.000
<b>WPh</b>	1.00	19.3	943.8	5.4	0.999

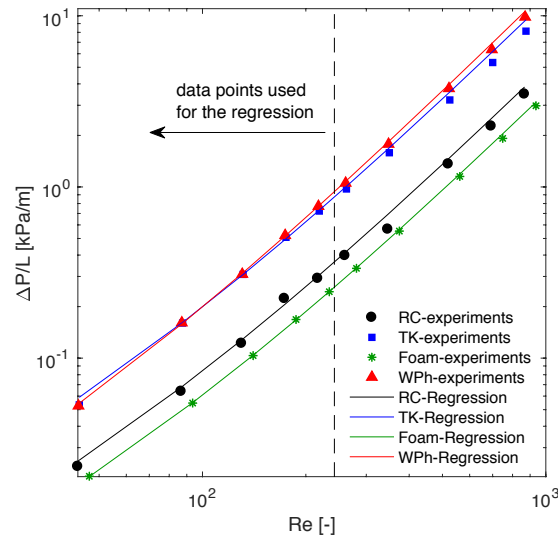


Figure 4.4. Measured pressure drops per length for the four specimens for 10 different velocities, corresponding to Re in the range of 40 to 940. The regression lines are obtained only using the data points with  $Re < 250$ .

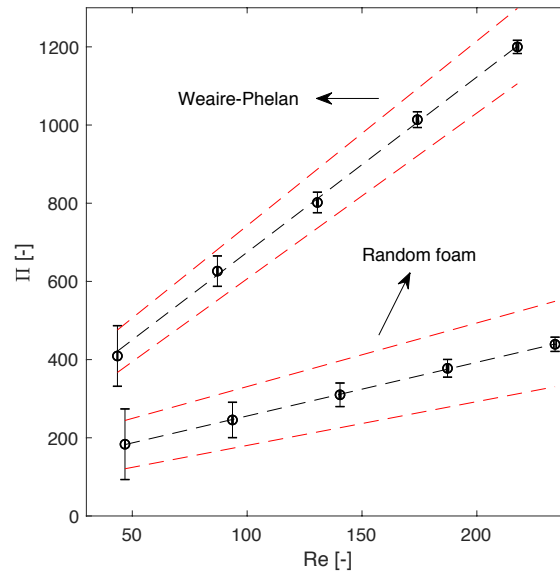


Figure 4.5. Measured dimensionless pressure gradient as a function of Reynolds number. The error bar indicates the calculated uncertainty of each data point. The black and red dotted-lines, respectively, represent the best line fits for mean and their standard errors.

#### 4.4.2 Literature comparison for pressure drop

Experimentally determined  $K$  and  $C$  of the foams with the same pore size (5 PPI) but different porosities (0.91-0.97) obtained from literature [29], [49], [31], [33], [50] were used for comparison (Table 4.3). Even though we chose reported data for samples with similar porosity and the same PPI value, it is not assured that their morphology is equivalent. The manufacturing process can, for example, affect the morphology by formation of clogged pores or different shapes of the struts. As illustrated by Inayat et al. [41], manufactured ceramic foams with different porosities have different strut shapes. The foams with porosities lower than 0.9 have a circular strut cross-section (similar to our samples), while increasing the porosity results in struts with triangular and concave triangular cross-sections. Also, the values reported in Table 4.3 are based on experiments with Reynolds numbers up to 5000, which clearly lies outside of the Forchheimer flow regime. At large Reynolds numbers a cubic model is recommended [51].

The foam used in our work has a permeability value within the range of permeability values reported ( $2.30 \pm 0.65 \cdot 10^{-7} \text{ m}^2$ ) but its form coefficient is 44% larger than the average of the reported values ( $188.5 \pm 18.6 \text{ m}^{-1}$ ). Accurate permeability values can be obtained by investigations at low Reynolds numbers, where the pressure changes are mainly due to the friction at the solid strut walls [2]. The higher form coefficient of our foam can be attributed to its lower porosity, which is about 9% less than the average porosity of the data in Table 4.3. In general, decreasing the porosity decreases the effective flow passage cross section leading to higher flow resistance.

Table 4.3. Permeability and form coefficients reported in literature for 5 PPI foams with different porosities

References	PPI	$\phi$ [-]	$K$ [ $\times 10^7 \text{ m}^2$ ]	$C$ [ $\text{m}^{-1}$ ]
Bhattacharya et al. [29]	5	0.973	2.7	186.7
	5	0.912	1.8	200.3
	5	0.972	2.52	191.2
	5	0.946	2.17	212.5
	5	0.905	1.74	187.0
Liu et al. [31]	5	0.914	3.7	164.1
Mancin [33]	5	0.921	1.52	151.3
Mancin [50]	5	0.920	2.36	205.0
Calmidi and Mahajan [49]	5	0.973	2.7	186.7
	5	0.912	1.8	200.3

For the comparison of the lattice structures, we used computational pressure drop predictions reported for regular structures. Cunsolo et al. [39] modelled a laminar flow in both WPh and TK structures and reported Darcy–Weisbach friction factors for different porosity and cell sizes. Wu et al. [38] also used a turbulence model to numerically investigate the pressure drop in an ideal TK lattice. Figure 4.6 shows the results of these two works together with the results of our study. Results of Cunsolo et al. are 25-70% higher than our values. These higher values are due to the methodology they used to calculate the friction factor and Reynolds number. In their model, the porous structure was heated up by a constant flux and the convective heat transfer coefficients were determined from the volume-averaged values of the solid and fluid temperatures. However, the calculations of Reynolds number and friction factor were based on the inlet velocity, which was lower than the average velocity. We expect that using the average velocity, will decrease their calculated friction factor and increase the Reynolds number, and consequently decreases the gap between our results. Also, the triangular shape of the strut cross section in their models results in higher tortuosity and thus higher pressure drops [54]. Wu et al. used circular struts, which is closer to the shape of the struts in our study. However due to the clogged windows, the final shapes of the manufactured TK and WPh lattices are different from the ideal models considered in the two numerical works. Our samples had friction factors 1.4-1.9 times larger than Wu et al., which can be explained by the higher drag forces caused by the clogged pores in the manufactured samples.

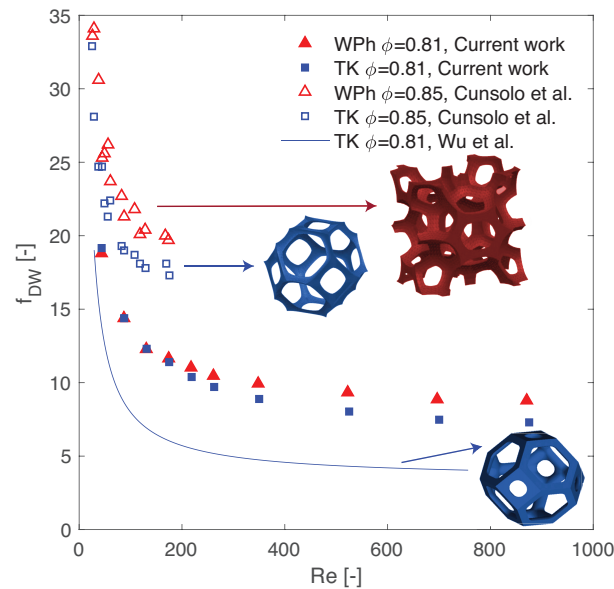


Figure 4.6. Comparison of our experimental friction factor of WPh and TK lattices with the numerical results in the literature. The values of Wu et al. were obtained by extrapolation of their results for a TK lattice with  $d_c = 4.75$  mm.

### 4.4.3 Predicted convective heat transfer coefficients

The samples were tested at five different inlet velocities (between 0.30 and 0.89 m/s). A typical result of the experimental and numerical air temperatures at the same sample cross section is presented in Figure 4.7. We note that the temperature profile was asymmetric due to the effect of buoyancy. The air properties and velocity used in the Reynolds and Nusselt formulations are based on the calculated volume averaged temperature and velocity of the fluid in the porous media. Figure 4.8 shows the predicted mean Nusselt number as a function of Reynolds number. TK and WPh lattices showed similar behavior and slightly higher values than RC lattice and the random foam. RC lattice had the lowest heat transfer rates, 30% lower than WPh at higher Reynolds numbers. As mentioned by Fuller et al. [23], there are two main causes for the enhanced heat exchange in porous media: higher specific surface area and tortuosity. In porous structures with high thermal conductivity (such as SiSiC specimens in this study), higher specific surface area means extended surfaces for heat transfer from the solid walls to the fluid and, thus, is directly proportional to the volumetric convective heat transfer coefficient. Ideal structures of WPh and TK lattices have larger specific surface area than the foam and RC structures (Table 4.1). The clogged pores in both manufactured WPh and TK lattices can change the flow characteristics, leading to a more tortuous fluid path [30] but also an increased probability of the flow separation from the solid walls. On one side, higher tortuosity increases the thermal dispersion within the porous medium and on the other side the separation effect can decrease the heat transfer from the solid walls to the fluid [39]. Furthermore, the lattices have slightly lower porosity (on average about 4% lower) than the random foam. Since porosity is inversely related to the fluid pore velocity, the lower porosity results in higher pore velocity, which can result in higher local heat transfer between the solid and the fluid.



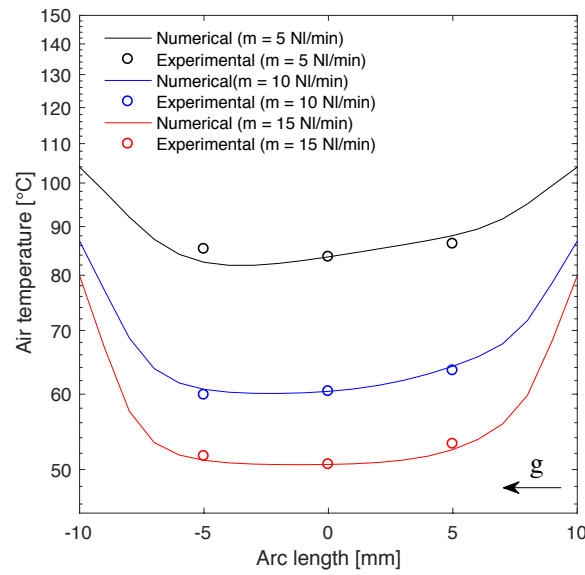


Figure 4.7. Comparison of experimental (points) and the numerical (lines) air temperatures at the porous sample outlet for a RC sample at three different velocities. Gravitational force is in the direction from right to left.

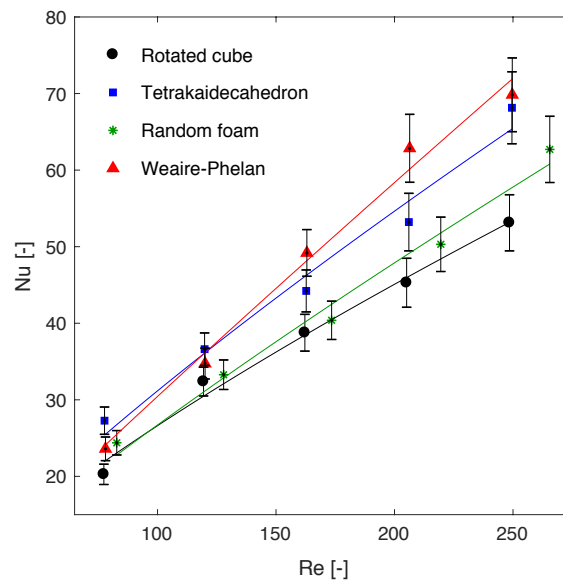


Figure 4.8. The predicted Nusselt number as a function of Reynolds number for the porous specimens. The uncertainty of the results, calculated according to Eq. 12, is indicated with error bars.

Empirical volumetric convective heat transfer coefficients are often reported in the form of Nusselt correlations as a function of porosity, Prandtl number and Reynolds number [24][25][2]. Nusselt number should asymptotically reach a constant value for the limit of very low Reynolds numbers [53]. However for the investigated range ( $70 < \text{Re} < 250$ ), a simpler power correlation is postulated:

$$\text{Nu}_v = a_1 \text{Re}^{a_2} \quad (4.33)$$

The coefficients  $a_1$  and  $a_2$  were obtained for the lattices and the foam by least square fitting.  $a_1$  is typically a function of Prandtl number and porosity. As we didn't test different fluids, no Prandtl dependence could be estimated. Theory predicts a  $\text{Pr}^{1/3}$  dependence for the flows over a cylinder [54]. The porosity dependence for the random foams are also reported [20], [26], [55]. Table 4.4 lists the correlation coefficients with the  $R^2$  values of the fittings.

Table 4.4. Coefficients of the proposed Nusselt correlations (Eq. 4.33) for each of the samples with  $R^2$  values of the fitting. The correlations are valid for  $70 < \text{Re} < 250$ .

Samples	$a_1$	$a_2$	$R^2$
RC	0.80	0.76	0.989
TK	0.75	0.81	0.976
Foam	0.55	0.84	0.985
WPh	0.40	0.94	0.990

#### 4.4.4 Literature comparison for heat transfer

Most of the data reported in literature has been obtained by analyses of random foams with small pore diameters (i.e.  $\text{PPI} \geq 10$ ). Table 4.5 collects empirical correlations based on random foams of different materials, cell density, and porosities.

Figure 4.9 (a) displays a comparison between the heat transfer results of the foam in this study and the values predicted by the correlations from literature. We observed a high variation between the proposed correlations, reaching a difference up to one order of magnitude. At low velocities, our foams agree best with the correlation of Xia et al. [26]. At high velocities the correlation of Wu et al. [55] has a better agreement with our experimental data.

Table 4.5. Literature correlations based on experimental studies of foams with various porosities and pore densities.

Reference	Correlation	Comments
Younis et al. [21]	$\text{Nu}_{\text{Yo}} = \frac{h_v d_p^2}{\lambda_f}$ $= 0.819 \left[ 1 - 7.33 \left( \frac{d_p}{L} \right) \right] \text{Re}_{\text{Yo}}^{0.36 \left[ 1 + 15.5 \left( \frac{d_p}{L} \right) \right]}$	<p>Based on 5 specimens of alumina foams with:</p> <p><math>0.83 &lt; \phi &lt; 0.87</math></p> <p><math>10 &lt; \text{PPI} &lt; 65</math></p> <p><math>5.1 &lt; \text{Re}_{\text{Yo}} = \frac{\rho_f u_f d_p}{\mu_f} &lt; 564</math></p>
Dietrich [25]	$\text{Nu}_{\text{Di}} = \frac{h_{\text{sf}} d_h}{\lambda_f} = 0.31 \text{Hg}^{\frac{1}{3}} \text{Pr}^{\frac{1}{3}}$ $\text{Hg} = 110 \text{Re}_{\text{Di}} + 1.45 \text{Re}_{\text{Di}}^2$ $d_h = \frac{4\phi}{A_{\text{sf}}}, S_v = \frac{2.87}{d_w + d_s} (1 - \phi)^{0.25}$	<p>Based on 18 specimens of alumina, mullite and oxidic-bonded SiC foams with:</p> <p><math>0.75 &lt; \phi &lt; 0.85</math></p> <p><math>10 &lt; \text{PPI} &lt; 45</math></p> <p><math>10^{-1} &lt; \text{Re}_{\text{Di}} = \frac{\rho_f u_f d_h}{\phi \mu_f} &lt; 10^5</math></p>
Kamiuto and Yee [24]	$\text{Nu}_{\text{KY}} = \frac{h_v d_{\text{st}}^2}{\lambda_f} = 0.124 (\text{Re}_{\text{KY}} \text{Pr})^{0.791}$ $d_{\text{st}} = 2d_c \frac{0.5 + \cos \left( \frac{1}{3} \cos^{-1} (2\phi - 1) + \frac{4\pi}{3} \right)}{\sqrt{\pi}}$	<p>Based on 16 specimens of cordierite–aluminite, nickel, alumina, cordierite and mullite foams with:</p> <p><math>0.74 &lt; \phi &lt; 0.95</math></p> <p><math>6 &lt; \text{PPI} &lt; 60</math></p> <p><math>1 &lt; \text{Re}_{\text{KY}} \text{Pr} = \frac{\rho_f u_f d_{\text{st}}}{\mu_f} \text{Pr} &lt; 1000</math></p>
Wu et al. [55]	$\text{Nu}_{\text{Wu}} = \frac{h_v d_c^2}{\lambda_f} = 32.504 \phi^{0.38} - 109.94 \phi^{1.38} + 166.65 \phi^{2.38} - 86.98 \phi^{3.38} \text{Re}_{\text{Wu}}^{0.438}$	<p>Based on parametric numerical study on TK lattices with:</p> <p><math>0.66 &lt; \phi &lt; 0.93</math></p> <p><math>1.414 &lt; d_c &lt; 2.828</math></p> <p><math>70 &lt; \text{Re}_{\text{Wu}} = \frac{\rho_f u_f d_c}{\lambda_f} &lt; 800</math></p>
Xia et al. [26]	$\text{Nu}_{\text{Xi}} = \frac{h_v d_p^2}{\lambda_f} = 0.34 \phi^{-2} \text{Re}_{\text{Xi}}^{0.61} \text{Pr}^{\frac{1}{3}}$	<p>Based on 9 specimens of Cu, Ni, SiC foams with:</p> <p><math>0.87 &lt; \phi &lt; 0.97</math></p> <p><math>10 &lt; \text{PPI} &lt; 40</math></p> <p><math>20 &lt; \text{Re}_{\text{Xi}} = \frac{\rho_f u_f d_p}{\mu_f} &lt; 1000</math></p>

Similar to the pressure drop results, WPh and TK lattices are compared in Figure 4.9 (b) with the numerically obtained heat transfer results of Cunsolo et al. [39] and Wu et al. [55]. The overall trend of our results agrees with their predictions. At high Reynolds numbers, the correlation of Wu et al. [38] predicts similar Nusselt numbers as our results, however at lower Reynolds numbers we predict values 65% lower than theirs.

The discrepancy between the experimental works, shown in Figure 4.9 (a), is attributed to the different measurement techniques (steady state or transient methods), and also different ranges of measurement conditions such as skeleton's material and flow velocity. Besides, the traditional manufacturing processes result in foams that are geometrically different from sample to sample [58]. Various irregularities are presented in pore microstructure of commercial foams, which results in different cell distributions, presence of closed pores or local agglomeration of material and also a variation in surface roughness of each sample. These irregularities, which influence the flow path and the heat transfer rates, are not accounted in any of the correlations shown in Table 4.5. Direct additive manufacturing techniques can resolve some of these problems, as they benefit from reproducible computer-controlled processes for creation of complex structures.

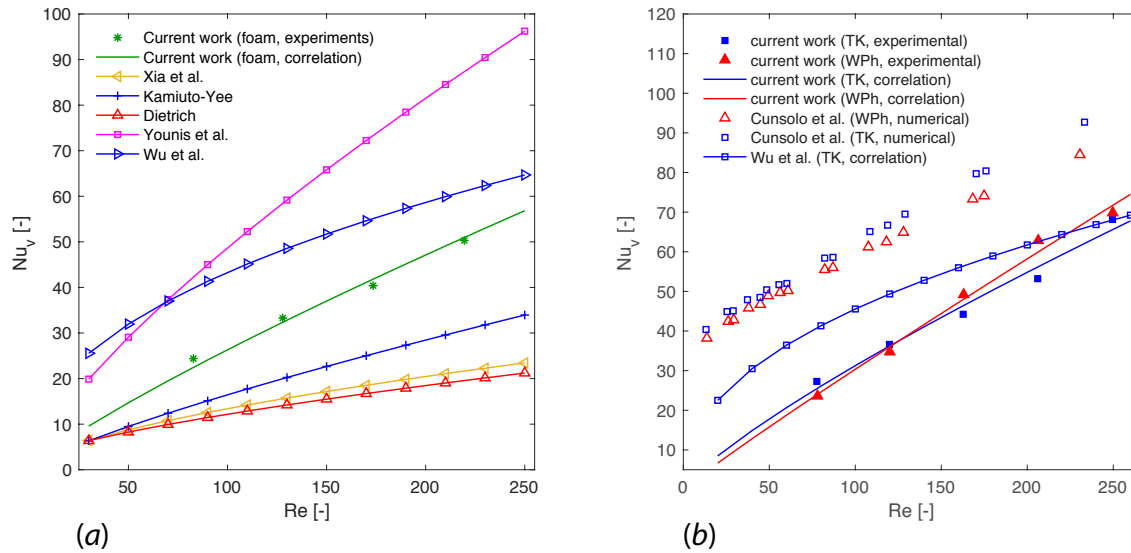


Figure 4.9. (a) Comparison of the predicted Nusselt values for the foam in the present study with correlations listed in Table 4.5. All correlations are plotted for a 5 PPI foam with  $\phi = 0.843$ . (b) Comparison between the Nusselt values of the numerical results from the literature with the values obtained in the current study for TK and WPh.

### 4.5 Conclusions

We present pressure drop and convective heat transfer measurements of porous media with different morphologies. RC, TK and WPh lattices (obtained by additive manufacturing) and commercial random foams with similar structural parameters (porosity and cell density) are investigated. The volumetric convective heat transfer coefficients of the specimens were estimated using the steady state experiments combined with numerical simulations. The numerical model consisted of solving the Brinkman equations with Forchheimer corrections coupled with two-homogeneous phase local non-thermal equilibrium formulations.

The production of the specimens using replica technique caused undesirable cell window clogging, which was observed specifically in smaller cell windows in TK and WPh samples and affected their transport properties (compared to ideal, unclogged TK and WPh structures). The pressure drop and heat transfer analysis showed that the manufactured RC lattice and the random foam have 2-3 times lower pressure drops and slightly lower heat transfer rates compared to WPh and TK lattices. The higher pressure drop values in TK and WPh samples were mainly attributed to the clogged pores, leading to higher flow resistance. However, for the same porosity and cell density, the lower specific surface area of the RC lattice and the foam explained their lower heat transfer rates. Hence, the overall transport properties of the porous structures are not only a function of the cell size and porosity but also depend on the geometrical anomalies, which can deviate the flow path. Finally, correlations are proposed for each of the morphologies to obtain volumetric Nusselt number as a function of Reynolds number, valid for the range of  $70 < Re < 250$ . The results were then compared to the literature showing an agreement for the foam values and general support for the values obtained for the TK and WPh lattices.

### 4.6 References

- [1] L. J. Gibson and M. F. Ashby, *Cellular Solids: Structure and Properties*. Cambridge University Press, 1999.
- [2] M. Scheffler and P. Colombo, *Cellular ceramics: structure, manufacturing, properties and applications*. John Wiley & Sons, 2006.
- [3] A. Ortona, C. D'Angelo, S. Gianella, and D. Gaia, "Cellular ceramics produced by rapid prototyping and replication," *Mater. Lett.*, vol. 80, pp. 95–98, Aug. 2012.
- [4] J. W. Halloran, "Ceramic Stereolithography: Additive Manufacturing for Ceramics by Photopolymerization," *Annu. Rev. Mater. Res.*, vol. 46, no. 1, pp. 19–40, 2016.
- [5] J. T. Muth, P. G. Dixon, L. Woish, L. J. Gibson, and J. A. Lewis, "Architected cellular ceramics with tailored stiffness via direct foam writing," *Proc. Natl. Acad. Sci.*, p. 219, Feb. 2017.
- [6] P. F. Egan, V. C. Gonella, M. Engensperger, S. J. Ferguson, and K. Shea, "Computationally designed lattices with tuned properties for tissue engineering using 3D printing," *PLOS ONE*, vol. 12, no. 8, p. e0182902, Aug. 2017.
- [7] D. W. Rosen, "Computer-Aided Design for Additive Manufacturing of Cellular Structures," *Comput.-Aided Des. Appl.*, vol. 4, no. 5, pp. 585–594, Jan. 2007.
- [8] G. Yang, C. Hou, M. Zhao, and W. Mao, "Comparison of convective heat transfer for Kagome and tetrahedral truss-cored lattice sandwich panels," *Sci. Rep.*, vol. 9, 2019.
- [9] J. Tian *et al.*, "Fluid Flow and Heat Transfer Characteristics of Composite Lattice Core Sandwich Structures," *Int. J. Heat Mass Transf.*, vol. 47, no. 14, pp. 3171–3186, Jul. 2004.
- [10] V. S. Deshpande, M. F. Ashby, and N. A. Fleck, "Foam topology: bending versus stretching dominated architectures," *Acta Mater.*, vol. 49, no. 6, pp. 1035–1040, Apr. 2001.
- [11] Wadley Haydn N.G, "Multifunctional periodic cellular metals," *Philos. Trans. R. Soc. Math. Phys. Eng. Sci.*, vol. 364, no. 1838, pp. 31–68, Jan. 2006.
- [12] A. R. Studart, U. T. Gonzenbach, E. Tervoort, and L. J. Gauckler, "Processing Routes to Macroporous Ceramics: A Review," *J. Am. Ceram. Soc.*, vol. 89, no. 6, pp. 1771–1789, Jun. 2006.
- [13] E. Rezaei, G. Bianchi, S. Gianella, and A. Ortona, "On the nonlinear mechanical behavior of macroporous cellular ceramics under bending," *J. Eur. Ceram. Soc.*, vol. 34, no. 10, pp. 2133–2141, Sep. 2014.

- [14] E. Rezaei, S. Haussener, S. Gianella, and A. Ortona, “Early-stage oxidation behavior at high temperatures of SiSiC cellular architectures in a porous burner,” *Ceram. Int.*, vol. 42, no. 14, pp. 16255–16261, Nov. 2016.
- [15] S. Gianella, D. Gaia, and A. Ortona, “High Temperature Applications of SiSiC Cellular Ceramics,” *Adv. Eng. Mater.*, vol. 14, no. 12, pp. 1074–1081, 2012.
- [16] T. Fend, B. Hoffschmidt, R. Pitz-Paal, O. Reutter, and P. Rietbrock, “Porous materials as open volumetric solar receivers: Experimental determination of thermophysical and heat transfer properties,” *Energy*, vol. 29, no. 5–6, pp. 823–833, Apr. 2004.
- [17] S. Wood and A. T. Harris, “Porous burners for lean-burn applications,” *Prog. Energy Combust. Sci.*, vol. 34, no. 5, pp. 667–684, Oct. 2008.
- [18] Y. S. Montenegro Camacho *et al.*, “Development of a robust and efficient biogas processor for hydrogen production. Part 2: Experimental campaign,” *Int. J. Hydrog. Energy*, vol. 43, no. 1, pp. 161–177, Jan. 2018.
- [19] S. Suter and S. Haussener, “Morphology Engineering of Porous Media for Enhanced Solar Fuel and Power Production,” *JOM*, vol. 65, no. 12, pp. 1702–1709, Dec. 2013.
- [20] S. Suter, A. Steinfeld, and S. Haussener, “Pore-level engineering of macroporous media for increased performance of solar-driven thermochemical fuel processing,” *Int. J. Heat Mass Transf.*, vol. 78, pp. 688–698, Nov. 2014.
- [21] L. B. Younis and R. Viskanta, “Experimental determination of the volumetric heat transfer coefficient between stream of air and ceramic foam,” *Int. J. Heat Mass Transf.*, vol. 36, no. 6, pp. 1425–1434, Jan. 1993.
- [22] V. V. Calmide and R. L. Mahajan, “Forced Convection in High Porosity Metal Foams,” *J. Heat Transf.*, vol. 122, no. 3, pp. 557–565, Feb. 2000.
- [23] A. J. Fuller, T. Kim, H. P. Hodson, and T. J. Lu, “Measurement and interpretation of the heat transfer coefficients of metal foams,” *Proc. Inst. Mech. Eng. J. Mech. Eng. Sci. Part C Lond.*, vol. 219, no. 2, pp. 183–191, Feb. 2005.
- [24] K. Kamiuto and S. S. Yee, “Heat transfer correlations for open-cellular porous materials,” *Int. Commun. Heat Mass Transf.*, vol. 32, no. 7, pp. 947–953, Jul. 2005.
- [25] B. Dietrich, “Heat transfer coefficients for solid ceramic sponges – Experimental results and correlation,” *Int. J. Heat Mass Transf.*, vol. 61, pp. 627–637, Jun. 2013.

- [26] X. Xia, X. Chen, C. Sun, Z. Li, and B. Liu, “Experiment on the convective heat transfer from airflow to skeleton in open-cell porous foams,” *Int. J. Heat Mass Transf.*, vol. 106, pp. 83–90, Mar. 2017.
- [27] B. Dietrich, “Pressure drop correlation for ceramic and metal sponges,” *Chem. Eng. Sci.*, vol. 74, no. Supplement C, pp. 192–199, May 2012.
- [28] N. Dukhan, “Correlations for the pressure drop for flow through metal foam,” *Exp. Fluids*, vol. 41, no. 4, pp. 665–672, Oct. 2006.
- [29] A. Bhattacharya, V. V. Calmidi, and R. L. Mahajan, “Thermophysical properties of high porosity metal foams,” *Int. J. Heat Mass Transf.*, vol. 45, no. 5, pp. 1017–1031, Feb. 2002.
- [30] E. A. Moreira, M. D. M. Innocentini, and J. R. Coury, “Permeability of ceramic foams to compressible and incompressible flow,” *J. Eur. Ceram. Soc.*, vol. 24, no. 10–11, pp. 3209–3218, Sep. 2004.
- [31] J. F. Liu, W. T. Wu, W. C. Chiu, and W. H. Hsieh, “Measurement and correlation of friction characteristic of flow through foam matrixes,” *Exp. Therm. Fluid Sci.*, vol. 30, no. 4, pp. 329–336, Mar. 2006.
- [32] L. Giani, G. Groppi, and E. Tronconi, “Mass-Transfer Characterization of Metallic Foams as Supports for Structured Catalysts,” *Ind. Eng. Chem. Res.*, vol. 44, no. 14, pp. 4993–5002, Jul. 2005.
- [33] S. Mancin, C. Zilio, A. Cavallini, and L. Rossetto, “Pressure drop during air flow in aluminum foams,” *Int. J. Heat Mass Transf.*, vol. 53, no. 15–16, pp. 3121–3130, Jul. 2010.
- [34] A. Inayat, J. Schwerdtfeger, H. Freund, C. Körner, R. F. Singer, and W. Schwieger, “Periodic open-cell foams: Pressure drop measurements and modeling of an ideal tetrakaidecahedra packing,” *Chem. Eng. Sci.*, vol. 66, no. 12, pp. 2758–2763, Jun. 2011.
- [35] D. Edouard, M. Lacroix, C. P. Huu, and F. Luck, “Pressure drop modeling on solid foam: State-of-the art correlation,” *Chem. Eng. J.*, vol. 144, no. 2, pp. 299–311, Oct. 2008.
- [36] J. Petrasch, F. Meier, H. Friess, and A. Steinfeld, “Tomography based determination of permeability, Dupuit–Forchheimer coefficient, and interfacial heat transfer coefficient in reticulate porous ceramics,” *Int. J. Heat Fluid Flow*, vol. 29, no. 1, pp. 315–326, Feb. 2008.
- [37] S. Haussener, P. Coray, W. Lipiński, P. Wyss, and A. Steinfeld, “Tomography-Based Heat and Mass Transfer Characterization of Reticulate Porous Ceramics for High-



- Temperature Processing,” *J. Heat Transf.*, vol. 132, no. 2, pp. 023305–023305, Dec. 2009.
- [38] Z. Wu *et al.*, “Experimental and numerical studies of the pressure drop in ceramic foams for volumetric solar receiver applications,” *Appl. Energy*, vol. 87, no. 2, pp. 504–513, Feb. 2010.
- [39] S. Cunsolo, M. Iasiello, M. Oliviero, N. Bianco, W. K. Chiu, and V. Naso, “Lord Kelvin and Weaire–Phelan Foam Models: Heat Transfer and Pressure Drop,” *J. Heat Transf.*, vol. 138, no. 2, p. 022601, 2016.
- [40] A. Ortona, D. H. Yoon, T. Fend, G. Feckler, and O. Smirnova, “Tubular Si-infiltrated SiC<sub>f</sub>/SiC composites for solar receiver application – Part 2: Thermal performance analysis and prediction,” *Sol. Energy Mater. Sol. Cells*, vol. 140, pp. 382–387, Sep. 2015.
- [41] A. Inayat, H. Freund, T. Zeiser, and W. Schwieger, “Determining the specific surface area of ceramic foams: The tetrakaidecahedra model revisited,” *Chem. Eng. Sci.*, vol. 66, no. 6, pp. 1179–1188, Mar. 2011.
- [42] L. G. Blevins and W. M. Pitts, “Modeling of bare and aspirated thermocouples in compartment fires,” *Fire Saf. J.*, vol. 33, no. 4, pp. 239–259, Nov. 1999.
- [43] S. Whitaker, “Forced convection heat transfer correlations for flow in pipes, past flat plates, single cylinders, single spheres, and for flow in packed beds and tube bundles,” *AIChE J.*, vol. 18, no. 2, pp. 361–371, Mar. 1972.
- [44] K. Vafai and S. J. Kim, “On the limitations of the Brinkman–Forchheimer-extended Darcy equation,” *Int. J. Heat Fluid Flow*, vol. 16, no. 1, pp. 11–15, Feb. 1995.
- [45] K. Vafai, *Handbook of Porous Media, Third Edition*. CRC Press, 2015.
- [46] D. York, N. M. Evensen, M. L. Martinez, and J. De Basabe Delgado, “Unified equations for the slope, intercept, and standard errors of the best straight line,” *Am. J. Phys.*, vol. 72, no. 3, pp. 367–375, Feb. 2004.
- [47] A. Dybbs and R. V. Edwards, “A New Look at Porous Media Fluid Mechanics — Darcy to Turbulent,” in *Fundamentals of Transport Phenomena in Porous Media*, J. Bear and M. Y. Corapcioglu, Eds. Dordrecht: Springer Netherlands, 1984, pp. 199–256.
- [48] E. A. Moreira and J. R. Coury, “The influence of structural parameters on the permeability of ceramic foams,” *Braz. J. Chem. Eng.*, vol. 21, no. 1, pp. 23–33, Jan. 2004.
- [49] V. V. Calmidi and R. L. Mahajan, “Forced convection in high porosity metal foams,” *J. Heat Transf.*, vol. 122, no. 3, pp. 557–565, Feb. 2000.

- [50] S. Mancin, C. Zilio, L. Rossetto, and A. Cavallini, “Heat Transfer Performance of Aluminum Foams,” *J. Heat Transf.*, vol. 133, no. 6, pp. 060904–060904–9, Mar. 2011.
- [51] J. L. Lage, B. V. Antohe, and D. A. Nield, “Two Types of Nonlinear Pressure-Drop Versus Flow-Rate Relation Observed for Saturated Porous Media,” *J. Fluids Eng.*, vol. 119, no. 3, p. 700, 1997.
- [52] A. Inayat, M. Klumpp, M. Lämmermann, H. Freund, and W. Schwieger, “Development of a new pressure drop correlation for open-cell foams based completely on theoretical grounds: Taking into account strut shape and geometric tortuosity,” *Chem. Eng. J.*, vol. 287, pp. 704–719, Mar. 2016.
- [53] N. Wakao and S. Kagei, *Heat and mass transfer in packed beds*. New York: Gordon and Breach Science Publishers, 1982.
- [54] S. W. Churchill and M. Bernstein, “A Correlating Equation for Forced Convection From Gases and Liquids to a Circular Cylinder in Crossflow,” *J. Heat Transf.*, vol. 99, no. 2, pp. 300–306, May 1977.
- [55] Z. Wu, C. Caliot, G. Flamant, and Z. Wang, “Numerical simulation of convective heat transfer between air flow and ceramic foams to optimise volumetric solar air receiver performances,” *Int. J. Heat Mass Transf.*, vol. 54, no. 7–8, pp. 1527–1537, Mar. 2011.

## 5 Early-stage oxidation

*The content of this chapter is adapted with permission from Elsevier from an article by Ehsan Rezaei, Sophia Haussener, Sandro Gianella and Alberto Ortona published 2016 in Ceramics International [1].*

### 5.1 Introduction

Open-celled cellular ceramics are attractive materials for high temperature applications such as solar receivers, heat exchangers, porous burners and reformers [2]–[4]. Among the potential ceramic materials which can be shaped in a cellular architecture, silicon-infiltrated SiC (SiSiC) is particularly interesting due to its outstanding mechanical and thermal properties at high temperatures. SiSiC porous periodic architectures have recently been produced using replica technique of lattice structures obtained from polymeric templates made by 3D printing followed by reactive infiltration of silicon [5].

SiSiC cellular ceramics are currently industrially employed as burner components [6] at high temperatures ( $\sim 1400$  °C) in oxidative conditions. Indeed, porous SiSiC has proven to withstand long operating conditions in a combustion environment [7], [8]. It has been noted that foams' behavior is strongly affected by the way they interact with the environment during the very initial phases of operation. This is the result of high thermal shocks imposed to the structures during the ignition and the cooling phases of the operation, leading to high thermo-mechanical loads on the struts and the nodes [2]. Moreover, long operating times at high temperatures requires good corrosion resistance. The oxidation behavior of silicon and SiC is very complex due to different parameters and species participating in the reactions. Two main oxidation modes have been observed in presence of oxygen, depending on its partial pressure, temperature and mass flow velocity. At very high temperatures and low oxygen partial pressure, or very high velocities (over 100 m/s), the so-called active oxidation is dominant and the material is gradually consumed by the following reactions [9]–[11]:

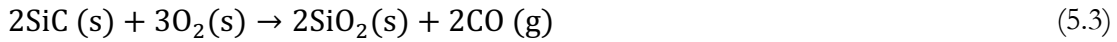
## Early-stage oxidation

---

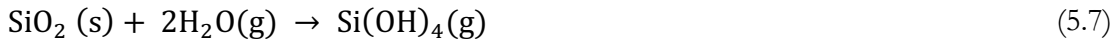
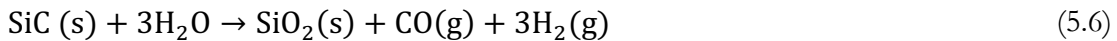
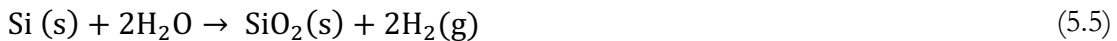


In this case a linear mass loss is observed due to volatile reaction products.

In high oxygen partial pressure environments, passive oxidation occurs. Passivation leads to the growth of a protective silica layer on the material surface and thus to a parabolic mass gain [12]. As the silica scale grows, the oxygen diffusion through the oxidation layer and the oxidation rate decrease [13]:



Water vapor, which is a byproduct of combustion, becomes the dominant reactant species for both silicon and SiC [14]–[19]. Simultaneous reaction of H<sub>2</sub>O with silica scale, Eq. (5.7), results in parabolic formation and linear consumption of SiO<sub>2</sub>, known as para-linear oxidation kinetics [20]:



In addition to the aforementioned reactions, oxidation can be affected by other factors such as scale/substrate interactions [21], [22], presence of impurities [12], [23], [24], and silica crystallization or fracture [14], [22], [25].

Another phenomenon, highlighted by Aronovici et al. [26], is the exudation of alloyed silicon beads at temperatures above 1400°C. Oxide scale foaming during long lasting operational conditions slows down the gasses flow in the pores with a subsequent local overheating and

degradation of the material [7]. It is thus very important to understand what triggers this phenomenon as it impacts the life span of porous ceramic burners' components.

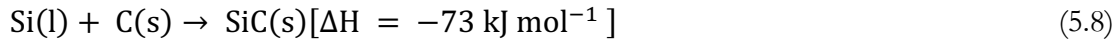
There are several works in the literature concerning oxidation of SiC, sintered and CVD (chemical vapor deposition), and silicon; few of them consider the case of SiSiC by reactive silicon infiltration [7], [13], [26]–[28]. There is a lack in studies on the effect of oxidation on macro porous materials in a flowing gas caused by combustion. Moreover porous materials under oxidation present a surface to volume ratio of about one order of magnitude higher than the bulk materials studied in the literature ( $500 \text{ m}^2/\text{m}^3$  vs.  $5 \text{ m}^2/\text{m}^3$ ). This has a dramatic effect on the porous material life span: we show in this work that lattice architecture changes hot gasses flow paths inside the structure and, as a consequence, affects oxidation. This work investigates the effect of cellular architecture and skeleton material microstructure on SiSiC porous ceramics degradation in a porous burner. The thermal tests in this study were all performed at  $1400^\circ\text{C}$  (slightly below silicon's melting point) as it is the typical operating temperature in industrial burners.

## 5.2 Experimental procedure

### 5.2.1 Material and sample preparation

Regular lattices, consisting of arrays of  $5 \times 5 \times 5$  cells, were designed by CAD (UGS NX 9.0, Siemens, Munich, D) with five different cell types (see Figure 5.1): tetrakaidecahedron, straight cube, rotated cube (with one of the cube's main diagonal along the flow direction) and a modified octet-truss unit cell as in [29]. The cell length was kept 7 mm. Random structures were generated from Laguerre Tessellation [30] with similar average geometrical parameters. All templates were 3D-printed with the same strut diameter  $d_{st} = 0.4 \text{ mm}$  using 3DLPrinter-HD 2.0 (Robot Factory S.r.l., It), with a resolution of 10 and 50  $\mu\text{m}$  in vertical and horizontal axes, respectively. Replica technique was used to convert the polymeric structures into ceramic [31]: the templates were impregnated in a slurry containing bimodal  $\alpha$ -SiC particles dispersed in an organic solvent by ball milling for 12 h and then, after adding a polymer binder, for further 36 h [5]. The fine and coarse SiC powders present an average particle size of 1.4  $\mu\text{m}$  D50 and 5  $\mu\text{m}$  D50, measured by laser diffraction, respectively. After drying the solvents, the resulting coating was comprised of 40 vol% plastic binder and 60 vol.% of ceramic powders. Pyrolysis of the green bodies was carried out in argon (300 sccm) with a heating rate of  $40^\circ\text{C}/\text{h}$  up to  $500^\circ\text{C}$ , and  $60^\circ\text{C}/\text{h}$  to  $1000^\circ\text{C}$ , followed by dwelling for 1 h and natural cooling. Decomposition of the green body leads to a skeleton material with  $\sim 30\%$  porosity. This porosity allows liquid silicon to fill the microstructure via capillary forces. Reactive infiltration using silicon of 99.5% purity was performed by heating

samples at 1500 °C for 4 h in a  $10^{-2}$  mbar residual pressure to form  $\beta$ -SiC according to the following reaction [32]:



The resulting microstructures consisted of  $\alpha$ -SiC particles, reaction bonded SiC and unreacted silicon ( $\sim 20\%$ ). Two opposite surfaces of each lattice were milled using diamond tools to realize parallel surfaces (Figure 5.1) for compression tests.

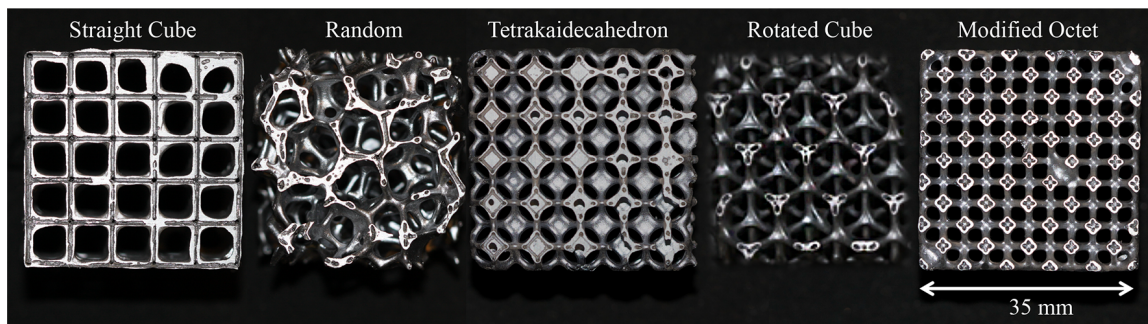


Figure 5.1. Front view of the five SiSiC lattices produced by replica technique.

### 5.2.2 Oxidation tests and characterization

45 samples were produced and divided in three groups as shown in Table 5.1. Samples of group I were oxidized in a furnace (LHT 08/16 Nabertherm GmbH, Bremen, D) in calm air atmospheric conditions. The furnace was heated up (10 °C/min) to 1400 °C, kept for one hour at that temperature and then naturally cooled to prevent thermal shock and preserve integrity of the oxide layer.

Table 5.1. Produced specimens and their distribution into three test groups.

	foam	rotated cube	cube	tetrakaidecahedron	octet	total/group
group I	3	3	3	3	3	15
group II	3	3	3	3	3	15
group III	3	3	3	3	3	15
tot./type	9	9	9	9	9	45

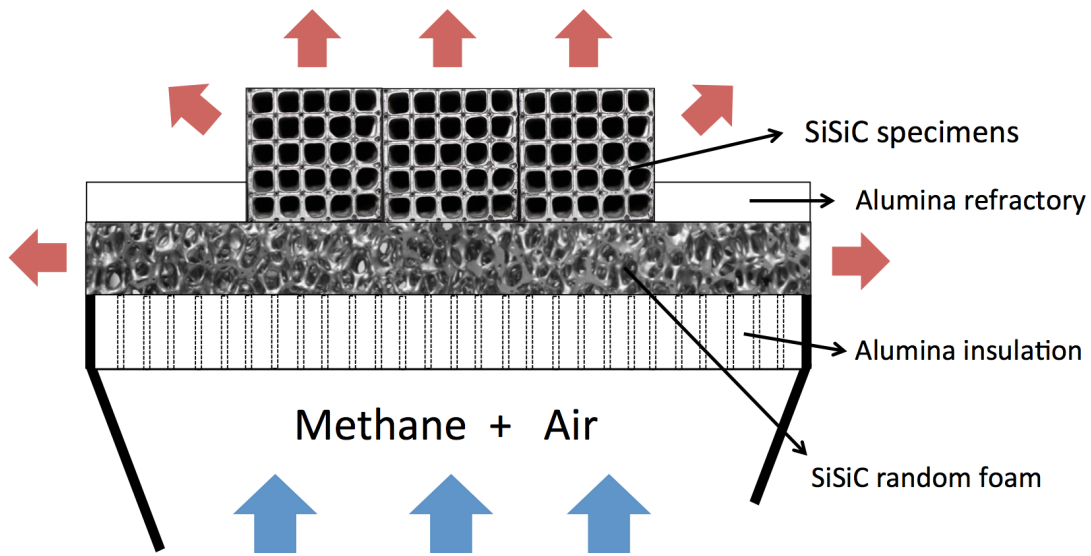


Figure 5.2. Schematic representation of the test set up with the porous burner and three cubic samples placed on it.

Group II specimens were tested using a porous burner. Porous burner is an advanced combustion technology that offers flameless and stable reaction of fuel and air with a homogeneous temperature field on the surface [3]. The schematic set up of the burner with specimens is shown in Figure 5.2. Methane and air enter into the system, pass the porous alumina insulation and react within the pores of the SiSiC foam (similar to the ones produced in this work). In each run three specimens of the same morphology were placed in the center of the burner. The rest of the burner's surface was covered with refractory alumina (Figure 5.2). The power and the ratio of actual to stoichiometric amount of air ( $\lambda$ ) feeding the system were adjusted to 25 kW and  $\lambda = 1.3$ , respectively. Tests were carried out following the subsequent procedure: flame ignition, dwelling, and shut down by closing the fuel valve while keeping the air flowing. The tests were consecutively repeated four times. Heating consisted

## Early-stage oxidation

---

in ramping up to 1400 °C (in the hottest spot on the lattice) at about 36 °C/sec. Samples were kept at 1400 °C for 15 min and then cooled to 400 °C at about 29 °C/sec. The temperature of the samples was measured using a two-color pyrometer (PYROSPOT DG 4N, DIAS Infrared GmbH, D). Group III samples were kept as produced. (Table 5.2) To evaluate the strength retention of the specimens, all samples of three groups were mechanically tested under compression.

Different characterization techniques were used to study the oxidation behavior. Optical microscopy (Leica DMLM, D) and a scanning electron microscopy (SEM) equipped with energy dispersive X-ray spectroscopy (JSM6010plus/LA, JEOL, Tokyo, JP) were used to evaluate the surface morphology and struts microstructure before and after the tests. Single struts of Group I and II were pulverized for X-ray diffraction (XRD) using Cu K $\alpha$  radiation analysis (PW 3830, Philips, Eindhoven, the Netherlands). One strut was extracted from each porous architecture and pulverized for the XRD tests. As a result the signal from the oxide phases is quite low, nevertheless we detected the same phases shown in the literature [7], [8], [18]. Due to silicon alloy formation and loss, peripheral strut rupture during the thermal treatment in the porous burner of the most delicate structures, the recorded mass change data were not reliable and thus not reported in detail. Compression tests were conducted in a typical compression test set-up using a universal testing machine (Z050, Zwick/Roell Ulm, D) with cross head speed of 0.1 mm/min. The displacement of the cross head and the loads were measured using the integrated position control system of the machine and a 50 kN load cell (Zwick/Roell, D) respectively.

Table 5.2. Thermal tests of each of the three groups of specimens.

	Thermal treatments	Temperature [°C]	Cycles
Group I	In furnace	1400	One cycle with slow cooling and heating ratios.
Group II	In porous burner	Max. 1400 (1100 - 1400)	Four cycles with 36 °C/s heating and 29 °C/s cooling ratios.
Group III		As produced	



## 5.3 Results and discussion

### 5.3.1 Oxidation behavior

Specimens of group I, which were oxidized isothermally in calm air, did not show any visible mechanical damage or crack. A general mass gain was observed in all specimens in agreement with our previous work [26], suggesting passivation as the dominant oxidation mode. Passivation produces a dense oxide layer of  $\text{SiO}_2$  according to reactions 3 and 4. The formation of this protective oxide scale decreases the oxygen diffusion rate and thus decelerates the oxidation process [13]. XRD pattern for the skeleton material after the tests revealed that this oxidation layer is likely made of cristobalite and tridymite (Figure 5.3).

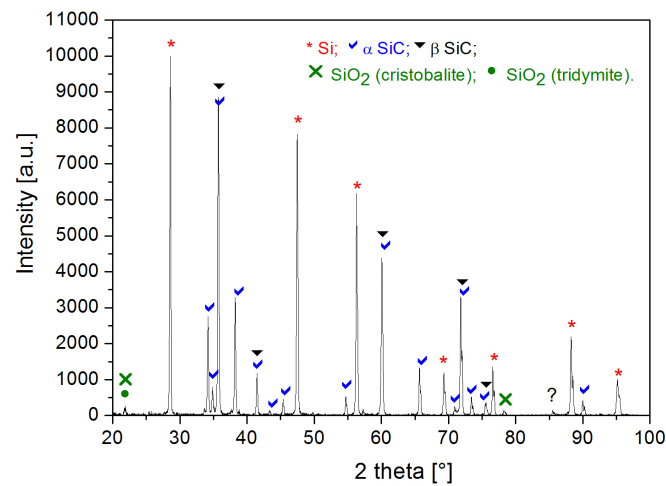


Figure 5.3. XRD analysis of a pulverized strut from cubic lattice after thermal tests of group I, showing the formation of cristobalite and tridymite.

All the samples used in this study present a cylindrical cavity inside the struts due to the replica manufacturing technique [33]. The presence of this cavity may lead to oxidation of inner surface of the struts. Due to limited oxygen supply, the surface of these cavities may undergo either active oxidation (resulting in loss of material) or formation of silica whiskers [27]. Figure 5.4 (a) shows the formation of silica whiskers inside the strut [26].

In addition to oxidation, scattered silicon alloy beads of different size were observed, mainly on the outer surface of the samples (Figure 5.4 (b)). EDS analyses of the beads showed the presence of iron, titanium and chromium. These impurities come from the silicon (purity: 99.5%). During high temperature conditioning being them alloyed with silicon melted

at low temperatures (lower than the test temperature). As pure silicon shrinks upon melting, it further favors the oxidation process by opening up new pores in the microstructure. On the other hand, silica while forming expands and squeezes out the molten silicon alloy from the microstructure [26]. The low wettability of the silicon alloy on  $\text{SiO}_2$  [34] favors beads formation on the strut's outer surface. These beads then coalesce in larger and larger beads (Figure 5.4 (b) dashed lines).

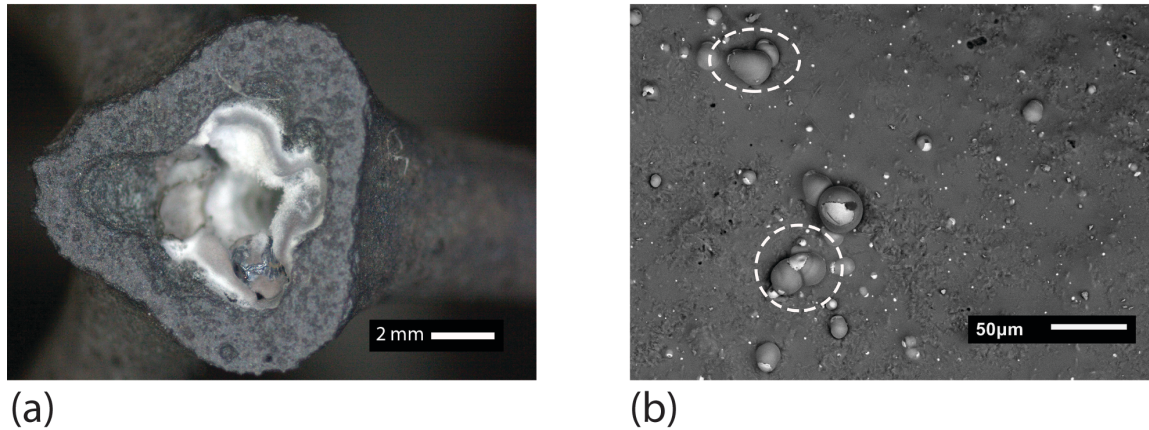


Figure 5.4. (a) Rotated cubic sample of group I after thermal oxidation. The cavities inside the struts oxidized in a lower oxygen partial pressure. That can result in formation of silica whiskers (white features). An exuded silicon alloy bead is also evident inside the strut. (b) Silicon alloy bead on the surface of a cubic lattice belonging to group I. White features correspond to heavier elements (Fe, Cr). In the dashed areas, beads coalescing in larger ones.

Unlike group I, samples of group II showed local corrosion due to inhomogeneous temperature and gas velocity in the lattices on the burner. The average gas velocity, entering the samples, was estimated around 5 m/s. The bottom side was at 1400°C whereas the top part was at 1100 °C. This temperature gradient resulted in different struts' coloration, which can be due to formation of different thicknesses of the silica scale [35]. Silicon alloy beads were observed only on the bottom part of the lattices (dashed rectangles in Figure 5.5).

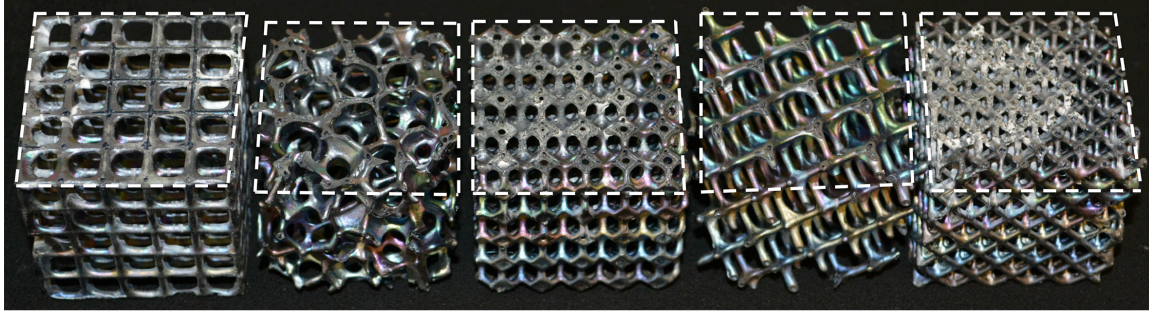
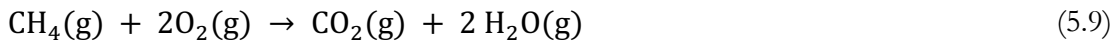


Figure 5.5. Five different lattices of group II after thermal tests in porous burner. The dashed lines mark out the surface at the maximum temperature 1400°C.

The ratio of actual to stoichiometric amount of air ( $\lambda$ ) in burner was 1.3 resulting in lean reaction of methane in air. The outlet gas flow was calculated to contain about 15 vol.% H<sub>2</sub>O and 7 vol.% CO<sub>2</sub>, according to Eq. 5.9 and 5 vol% O<sub>2</sub> due to the present excess air.



Gases with such compositions can degrade both silicon and SiC phases [13]. Because of the high percentage of water vapor, the samples faced a more severe oxidation in the hot zones compared to the samples of group I tested isothermally [36]. Presence of water vapor increases the oxidation rate of both Si and SiC by an order of magnitude [18], [19], [37]. H<sub>2</sub>O can also increase the porosity of the oxide layer [36]. Due to high gas velocity (over 1 m/s) inside the lattices, the oxidation kinetics can change to para-linear behavior following the simultaneous formation and volatilization of SiO<sub>2</sub>, shown in equations (5.5), (5.6) and (5.7) [38].

At the bottom of some lattices, where the temperature was ~1400 °C, and especially in the octet, tetrakaidecahedron and cubic structures, a distinct thick layer (20-200 μm) of porous silica was formed (Figure 5.6 (a)). This porous layer fully covered the windward side of the struts, while the leeward side was less affected. The severe oxidation was likely because of the high percentage of water vapor. Moreover molten silicon exuded on the surface in group II facilitating the oxidation. The exuded beads depleted the inner microstructure of free silicon leading to the formation of porosity (dashed rectangle in Figure 5.6 (a)) [39]. Figure 5.6 (b) depicts bubbles and craters together with whiskers in these regions. Gaseous products of the oxidation reactions may initially diffuse to the surface. With the oxide layer thickening, bubbles form into the viscous medium (most likely an amorphous silica film [13]) and move



toward the external surface. On the surface, they explode resulting in craters and filled-out bubbles [17] (Figure 5.6 (c)). These craters, exposing the bare SiSiC surface to the open environment, are then healed by the viscous flow of silica [21].

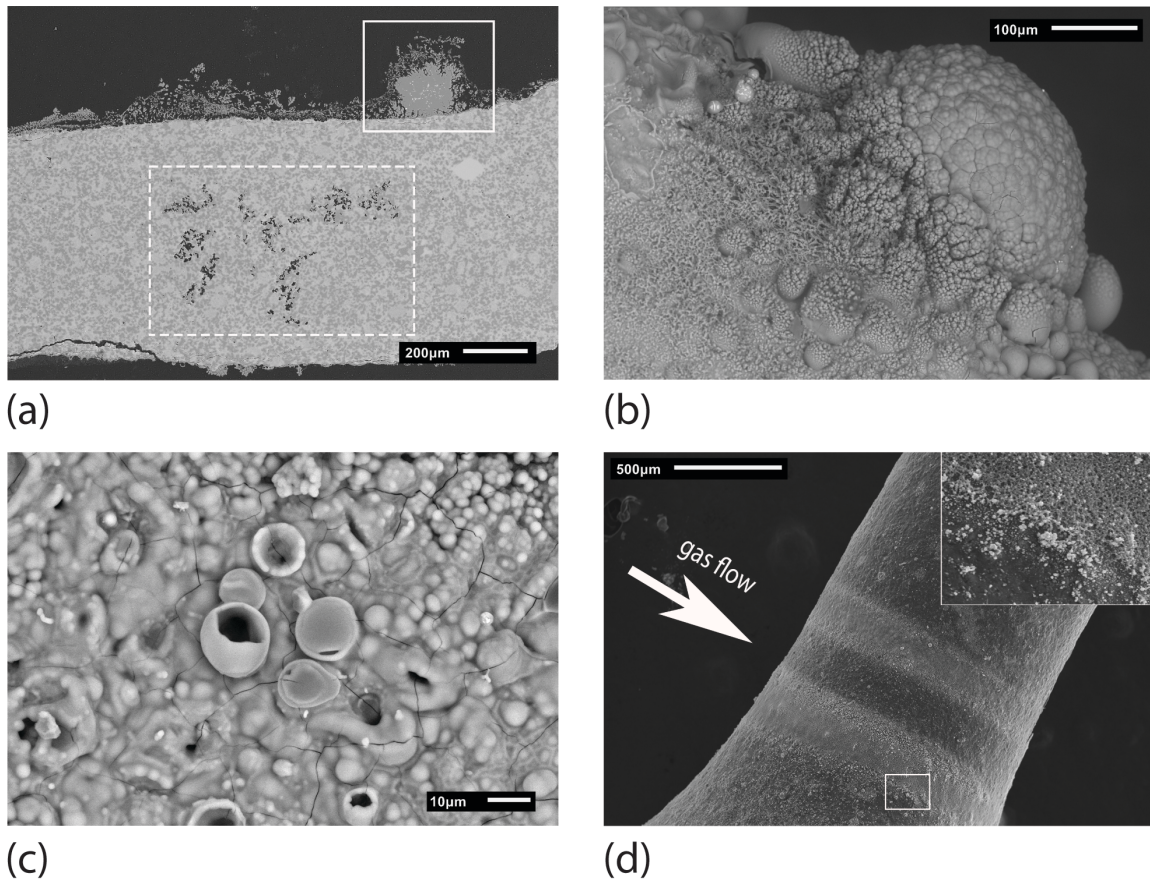


Figure 5.6. (a) A strut of octet samples of group II after tests. The topside of the strut is the windward side, which had a thicker silica scale. Silicon depleted regions are shown in the dashed rectangle. (b) SEM image of the surface (the hot zone) of octet specimen of group II after the tests. The swelled region corresponds to an exuded bead after severe oxidation. A cross section of it can be seen also in the rectangle in (a). (c) Bubble and craters formed in process of silica formation. Craters are filled with silica after the gas explosion. The silica surface is full of cracks made in thermal cycles due to large difference of its thermal expansion with substrate. (d) Formation of two stripes of silica on a strut of a cubic sample of group II. The white arrow shows the gas flow direction.

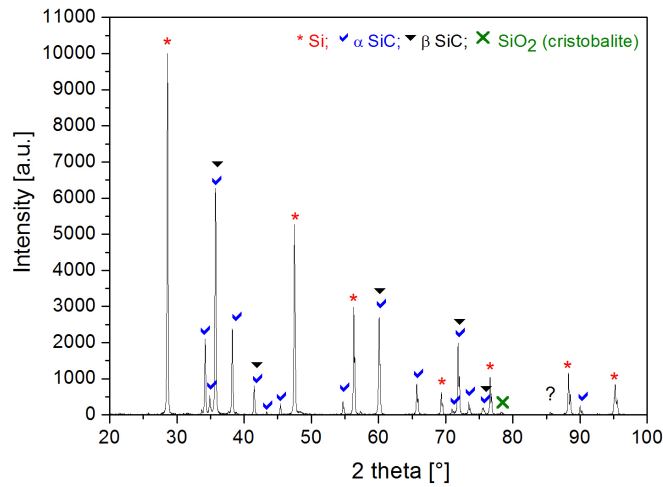


Figure 5.7. XRD analysis of a pulverized strut of a cubic lattice in group II.

In the colder part of the samples, the oxidation was negligible. However, on many struts, arc-shaped stripes of white silica were observed. This phenomenon took its form along the flow direction around the struts. These observations reveal the onset of oxidation on a single strut. Figure 5.6 (d) depicts SEM images from the surface of the oxide layers, characterized by silica wires. This is similar to what is reported as transition from active to passive oxidation mode in presence of oxygen [30]. This silica layer was loosely attached to the substrate resulting spallation in some zones, likely during heating and cooling ramps. XRD analysis of the strut showed the presence of cristobalite (Figure 5.7). We propose the mechanism of the ring shaped oxide layer formation as follows:

$\text{SiO}_2$  islands form on the surface, most likely in a point with higher concentration of impurities such as iron. At the same time  $\text{SiO}$  is produced and diffuses away from the surface [27]. The  $\text{SiO}_2$  islands act as nucleation points for  $\text{SiO}$  reacting with  $\text{O}_2$  and the formation of  $\text{SiO}_2$  rods [9]. In stationary air, this phenomenon results in circular regions on the surface [11]. In a gas flow over the struts, the very first nucleation zones are formed in the stagnation point (Figure 5.8 (a)).  $\text{SiO}$  is then transported by the gas and further oxidizes along the flow path on a single strut (Figure 5.8 (b)). In a turbulent flow regime, such as in a porous burner, the oxide layer formation continues up to the point where the flow separates from the strut's surface (Figure 5.8 (c) and (d)).

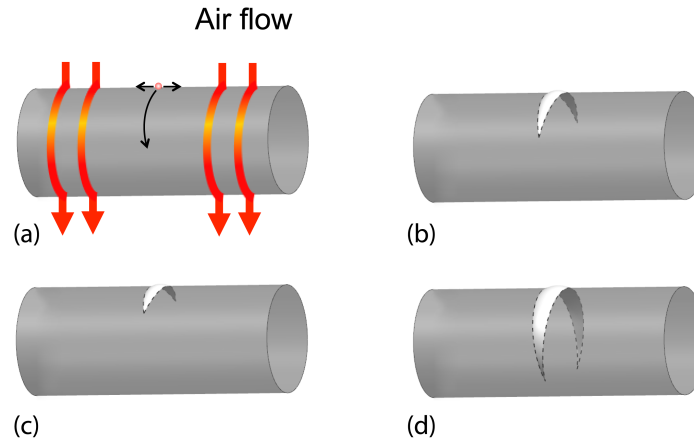


Figure 5.8. Schematic representation of the mechanism of formation of silica on a single strut. (a) The very first  $\text{SiO}_2$  points are formed in stagnation point of the flow. (b) The layer grows in both directions on the strut along the flow stream. (c) and (d) The gradual growth is much faster along the gas flow.

This porous silica layer was observed mainly on the straight cubic samples than on the other lattices. Silica was mainly cristobalite (Figure 5.7). Based on the proposed mechanism, lattices with struts misaligned in respect of the gasses flow (i.e. some struts of the octet, tetrakaidecahedron and straight cubic structures) get a higher chance to show this oxidation pattern, while it will be much less evident in rotated cubes and random foams (comprised of more struts aligned with the gasses flow).

### 5.3.2 Mechanical strength

In order to evaluate the effect of different lattice structures on the retained strength after the thermal cycling, isothermally oxidized (group I), thermally cycled (group II) and the as-produced (group III) samples were mechanically tested under compression. Load-displacement data of the samples showed two main regimes. An initial linear regime due to the elastic deformation of the struts. Further on, a new regime appeared due to the gradual failure of some struts, followed by the collapse of the entire porous architecture. This is in agreement with the literature [40] reporting damage accumulation mechanism in compression tests of ceramic foams. An example of the stress-strain curve for these lattices is plotted in Figure 5.9.

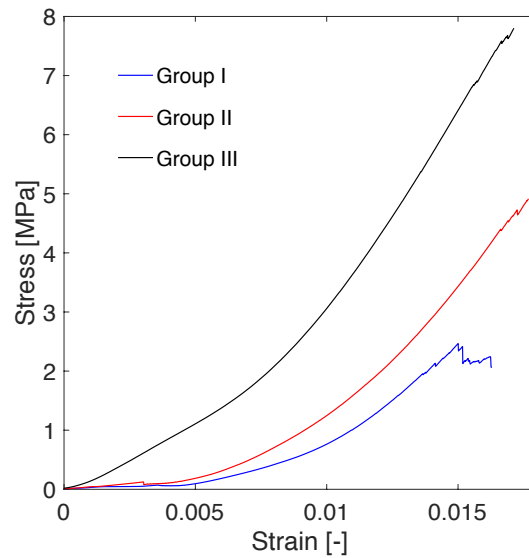


Figure 5.9. Stress-strain curves for three lattices with cubic structures from each of the three groups. Under compression loading, the struts were gradually breaking until the final catastrophic failure of the samples.

Figure 5.10 shows the result of the tests on samples of the three groups. Samples of group I showed a decrease in strength compared to as produced specimens. This can be explained by silicon melting and leaving the specimens and the consequent formation of porosity, as shown in Figure 5.6 (a), which reduces the strength of the skeleton's material. Results of group II specimens did not differ from the as-produced ones. One reason is that the phenomena described above occurred in a limited region of the sample facing the hottest zones. The rest of the structure was neither affected by silicon depletion nor heavily oxidized. In some sample the strength even increased; this can be due to the blunting of surface cracks by the formation of silica scale [24], [41].

It was also noticed that, while intact samples strength values were broadly distributed, the thermally treated specimens of group I and II had very low variations, which may suggest an increased uniformity in flaw distribution. This phenomenon is also reported for sintered SiC [42].

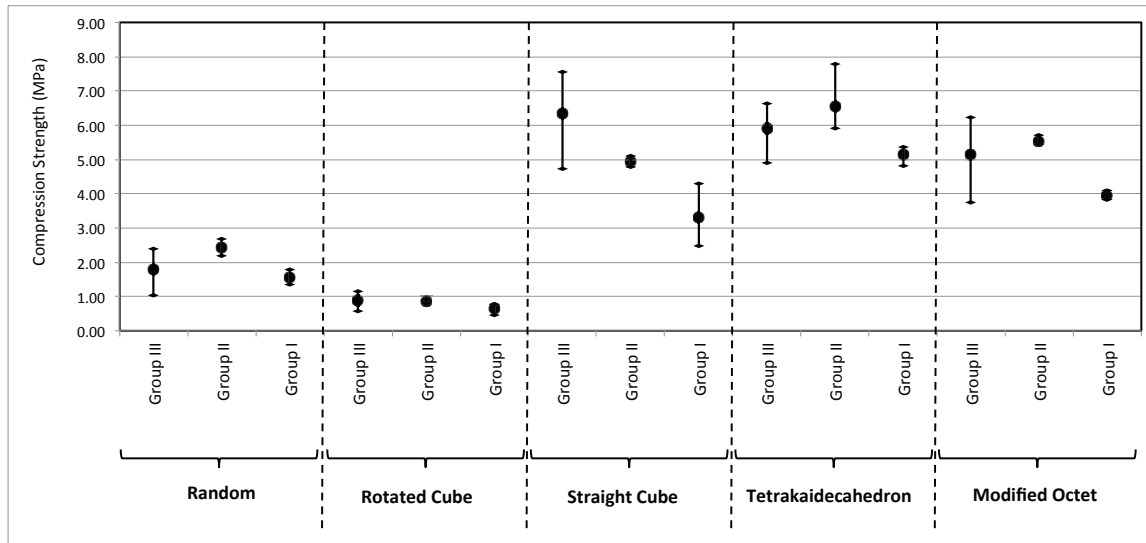


Figure 5.10. Compression test results of three sets of lattices before and after thermal tests. The maximum, minimum and the average values are displayed for lattices in each group. While strength values of group II specimens did not differ from the as-produced ones, samples of group I showed a decreased retained strength.

## 5.4 Conclusions

Oxidation behavior of five different SiSiC lattice structures were studied at 1400 °C. A group of specimens were thermally tested in calm air. The second group faced thermo-cyclic oxidation in a porous burner. It was shown that at 1400°C, there are two main limiting factors in using SiSiC materials: silicon alloy bead formation and combustion products such as H<sub>2</sub>O and CO<sub>2</sub>. Silicon alloy melted out of the samples, introducing more porosity in the microstructure. This resulted in decreased retention strength and rapid oxidation on the surface and inside porosities. High partial pressure of H<sub>2</sub>O in the combustion environment of the porous burner resulted in a porous silica glass layer on the hot zones of samples group II. This severe oxidation was also due to liquid silicon that melted out from the microstructure. In addition to this, silica was formed along the fluid flow on single struts. This can be explained as initial silica formation in the stagnation point of the flow and its gradual growth along the gas flow. The severity of oxidation in samples group II was different depending on lattice morphology. It was observed that straight cubic lattices, having more struts perpendicular to the gas flow direction, offer more stagnation zones and higher oxidation. Therefore, in designing lattices for high temperature applications, in addition to parameters such as thermo-mechanical properties or permeability, one should also consider the effect of lattice type on corrosion.



## 5.5 References

- [1] E. Rezaei, S. Haussener, S. Gianella, and A. Ortona, “Early-stage oxidation behavior at high temperatures of SiSiC cellular architectures in a porous burner,” *Ceram. Int.*, vol. 42, no. 14, pp. 16255–16261, Nov. 2016.
- [2] S. Gianella, D. Gaia, and A. Ortona, “High Temperature Applications of SiSiC Cellular Ceramics,” *Adv. Eng. Mater.*, vol. 14, no. 12, pp. 1074–1081, 2012.
- [3] D. Trnitskiy and F. Durst, “Combustion in a Porous Medium-Advances and Applications,” *Combust. Sci. Technol.*, vol. 121, no. 1–6, pp. 153–168, Dec. 1996.
- [4] T. Fend, B. Hoffschmidt, R. Pitz-Paal, O. Reutter, and P. Rietbrock, “Porous materials as open volumetric solar receivers: Experimental determination of thermophysical and heat transfer properties,” *Energy*, vol. 29, no. 5–6, pp. 823–833, Apr. 2004.
- [5] A. Ortona, C. D’Angelo, S. Gianella, and D. Gaia, “Cellular ceramics produced by rapid prototyping and replication,” *Mater. Lett.*, vol. 80, pp. 95–98, Aug. 2012.
- [6] A. Ortona *et al.*, “SiSiC Heat Exchangers for Recuperative Gas Burners with Highly Structured Surface Elements,” *Int. J. Appl. Ceram. Technol.*, vol. 11, no. 5, pp. 927–937, Sep. 2014.
- [7] F. R. A. Mach, F. V. Lssendorff, and A. Delgado, “Experimental Investigation of the Oxidation Behavior of SiSiC Foams,” in *Ceramic Engineering and Science Proceedings*, 2008, vol. 29, p. 299.
- [8] S. P. A Ortona, “Aging of reticulated Si-SiC foams in porous burners,” *Adv. Appl. Ceram.*, vol. 109, no. 4, pp. 246–251, 2010.
- [9] J. W. Hinze and H. C. Graham, “The Active Oxidation of Si and SiC in the Viscous Gas-Flow Regime,” *J. Electrochem. Soc.*, vol. 123, no. 7, pp. 1066–1073, Jul. 1976.
- [10] E. A. Gulbransen, K. F. Andrew, and F. A. Brassart, “The Oxidation of Silicon Carbide at 1150° to 1400°C and at  $9 \times 10^{-3}$  to  $5 \times 10^{-1}$  Torr Oxygen Pressure,” *J. Electrochem. Soc.*, vol. 113, no. 12, pp. 1311–1314, Dec. 1966.
- [11] N. S. Jacobson and D. L. Myers, “Active Oxidation of SiC,” *Oxid. Met.*, vol. 75, no. 1–2, pp. 1–25, Oct. 2010.
- [12] C. Wagner, “Passivity during the Oxidation of Silicon at Elevated Temperatures,” *J. Appl. Phys.*, vol. 29, no. 9, pp. 1295–1297, Sep. 1958.

- [13] N. S. Jacobson, "Corrosion of Silicon-Based Ceramics in Combustion Environments," *J. Am. Ceram. Soc.*, vol. 76, no. 1, pp. 3–28, 1993.
- [14] P. J. Jorgensen, M. E. Wadsworth, and I. B. Cutler, "Effects of Water Vapor on Oxidation of Silicon Carbide," *J. Am. Ceram. Soc.*, vol. 44, no. 6, pp. 258–261, 1961.
- [15] H. Cappelen, K. H. Johansen, K. Motzfeldt, J. Weidlein, and O. Wahlberg, "Oxidation of Silicon Carbide in Oxygen and in Water Vapour at 1500 degrees C.," *Acta Chem. Scand.*, vol. 35a, pp. 247–254, 1981.
- [16] T. Narushima, T. Goto, Y. Iguchi, and T. Hirai, "High-Temperature Oxidation of Chemically Vapor-Deposited Silicon Carbide in Wet Oxygen at 1823 to 1923 K," *J. Am. Ceram. Soc.*, vol. 73, no. 12, pp. 3580–3584, Dec. 1990.
- [17] M. Maeda, K. Nakamura, and T. Ohkubo, "Oxidation of silicon carbide in a wet atmosphere," *J. Mater. Sci.*, vol. 23, no. 11, pp. 3933–3938, Nov. 1988.
- [18] E. J. Opila, "Variation of the Oxidation Rate of Silicon Carbide with Water-Vapor Pressure," *J. Am. Ceram. Soc.*, vol. 82, no. 3, pp. 625–636, Mar. 1999.
- [19] B. E. Deal and A. S. Grove, "General Relationship for the Thermal Oxidation of Silicon," *J. Appl. Phys.*, vol. 36, no. 12, pp. 3770–3778, Dec. 1965.
- [20] E. J. Opila, "Oxidation and Volatilization of Silica Formers in Water Vapor," *J. Am. Ceram. Soc.*, vol. 86, no. 8, pp. 1238–1248, 2003.
- [21] R. Raj and K. Terauds, "Bubble Nucleation During Oxidation of SiC," *J. Am. Ceram. Soc.*, vol. 98, no. 8, pp. 2579–2586, Aug. 2015.
- [22] B. Harder, N. Jacobson, and D. Myers, "Oxidation Transitions for SiC Part II. Passive-to-Active Transitions," *J. Am. Ceram. Soc.*, vol. 96, no. 2, pp. 606–612, Feb. 2013.
- [23] E. J. Opila, "Oxidation Kinetics of Chemically Vapor-Deposited Silicon Carbide in Wet Oxygen," *J. Am. Ceram. Soc.*, vol. 77, no. 3, pp. 730–736, 1994.
- [24] S. C. Singhal and F. F. Lange, "Effect of Alumina Content on the Oxidation of Hot-Pressed Silicon Carbide," *J. Am. Ceram. Soc.*, vol. 58, no. 9–10, pp. 433–435, Sep. 1975.
- [25] L. U. J. T. Ogbuji and M. Singh, "High-temperature oxidation behavior of reaction-formed silicon carbide ceramics," *J. Mater. Res.*, vol. 10, no. 12, pp. 3232–3240, 1995.
- [26] M. Aronovici *et al.*, "Heat and Mass Transfer in Ceramic Lattices During High-Temperature Oxidation," *J. Am. Ceram. Soc.*, vol. 98, no. 8, pp. 2625–2633, Aug. 2015.

- [27] H. Nanri, M. Shirai, N. Takeuchi, S. Ishida, K. Watanabe, and M. Wakamatsu, "Oxidation Behavior of Si-SiC at High Temperature," *J. Ceram. Soc. Jpn.*, vol. 105, no. 1217, pp. 15–20, 1997.
- [28] R. Röttenbacher and G. Willmann, "SisiC — A Material for High Temperature Ceramic Heat Exchangers," in *Ceramics in Advanced Energy Technologies*, H. Kröckel, M. Merz, and O. V. D. Biest, Eds. Springer Netherlands, 1984, pp. 231–249.
- [29] A. Ortona and E. Rezaei, "Modeling the Properties of Cellular Ceramics: From Foams to Lattices and Back to Foams," *Adv. Sci. Technol.*, vol. 91, pp. 70–78, Oct. 2014.
- [30] C. Lautensack, "Fitting three-dimensional Laguerre tessellations to foam structures," *J. Appl. Stat.*, vol. 35, no. 9, pp. 985–995, Sep. 2008.
- [31] J. Adler, M. Teichgraeber, G. Standke, H. Jaunich, H. Stoever, and R. Stoetzel, "Open cell expanded ceramic with a high level of strength, and process for the production thereof, European Patent 0 907 (1999): 621."
- [32] E. Rezaei, G. Bianchi, S. Gianella, and A. Ortona, "On the nonlinear mechanical behavior of macroporous cellular ceramics under bending," *J. Eur. Ceram. Soc.*, vol. 34, no. 10, pp. 2133–2141, Sep. 2014.
- [33] S. Karl and A. V. Somers, "Method of making porous ceramic articles," US3090094 A, 21-May-1963.
- [34] R. Sangiorgi, M. L. Muolo, D. Chatain, and N. Eustathopoulos, "Wettability and Work of Adhesion of Nonreactive Liquid Metals on Silica," *J. Am. Ceram. Soc.*, vol. 71, no. 9, pp. 742–748, Sep. 1988.
- [35] H. C. Evitts, H. W. Cooper, and S. S. Flaschen, "Rates of Formation of Thermal Oxides of Silicon," *J. Electrochem. Soc.*, vol. 111, no. 6, pp. 688–690, Jun. 1964.
- [36] P. F. Tortorelli and K. L. More, "Effects of High Water-Vapor Pressure on Oxidation of Silicon Carbide at 1200°C," *J. Am. Ceram. Soc.*, vol. 86, no. 8, pp. 1249–1255, Aug. 2003.
- [37] E. J. Opila and R. E. Hann, "Paralinear Oxidation of CVD SiC in Water Vapor," *J. Am. Ceram. Soc.*, vol. 80, no. 1, pp. 197–205, 1997.
- [38] E. J. Opila, "Water Vapor Effects on High-Temperature Oxidation and Volatilization of Ceramics," *J. Am. Ceram. Soc.*, vol. 86, no. 8, pp. 1237–1237, 2003.
- [39] J. Adler, "Cellular ceramics made of silicon carbide ceramics for burner technology," presented at the The American Ceramic Society, 2009.

- [40] R. Brezny and D. J. Green, “Uniaxial Strength Behavior of Brittle Cellular Materials,” *J. Am. Ceram. Soc.*, vol. 76, no. 9, pp. 2185–2192, Sep. 1993.
- [41] F. F. Lange, “Healing of Surface Cracks in SiC by Oxidation,” *J. Am. Ceram. Soc.*, vol. 53, no. 5, pp. 290–290, May 1970.
- [42] T. E. Easler, R. C. Bradt, and R. E. Tressler, “Strength Distributions of SiC Ceramics After Oxidation and Oxidation Under Load,” *J. Am. Ceram. Soc.*, vol. 64, no. 12, pp. 731–734, Dec. 1981.

## 6 Anisotropic elastic properties

### 6.1 Introduction

Open cell foams are cellular materials with large porosities (over 70%) consisting of gas filled pores, i.e. cells, whose edges are made of interconnected solid ligaments. Generating pores into the structure of the materials, while creating many new applications for them, affects their mechanical properties and introduces new defects into their structure. Mechanical properties of cellular structures depend on three main factors: their relative density, cell morphology, and their constituent material. Gibson and Ashby [1] wrote the first detailed book on cellular solids, obtaining their properties and mechanisms of fracture. They revealed that for brittle open cell foams, the elastic modulus and strength are directly related to their relative density. Their analyses were based on a simplified cubic unit cell model with the assumption that the predominant failure mechanism in the foam is bending of the struts. Experimental studies have validated, to a certain extent, Gibson and Ashby's results [2]–[4]. It must be noted that real foams are different from the simplified model of Gibson and Ashby. They consist of defects such as aggregations, closed cell walls, and strut cavities, and their heterogeneous structure results in locally weak zones, which decreases their overall mechanical properties. The exact properties of the foams' constituent material is difficult to obtain, as ceramics tend to have different strength based on their size and manufacturing method [5].

Deshpande et al. [6] showed that even though most random foams fail by a bending-dominated mechanism, we can design stretching-dominated structures, which fail by tension or compression of their struts. This can largely enhance mechanical properties of these structures. It is shown that the stiffness and strength of the bending and stretching-dominated structures scales with relative density as follows [7]:

$$\text{stiffness} \propto \rho_{\text{rel}}^2, \quad \text{strength} \propto \rho_{\text{rel}}^{1.5} \quad (\text{bending – dominated}) \quad (6.10)$$

$$\text{stiffness} \propto \rho_{\text{rel}}, \quad \text{strength} \propto \rho_{\text{rel}} \quad (\text{stretching – dominated}) \quad (6.11)$$

Therefore, for a certain relative density, stretching-dominated structures are stiffer and stronger than the bending-dominated ones. Figure 6.1 shows different polyhedral cells with bending and stretching-dominated fracture mechanisms.

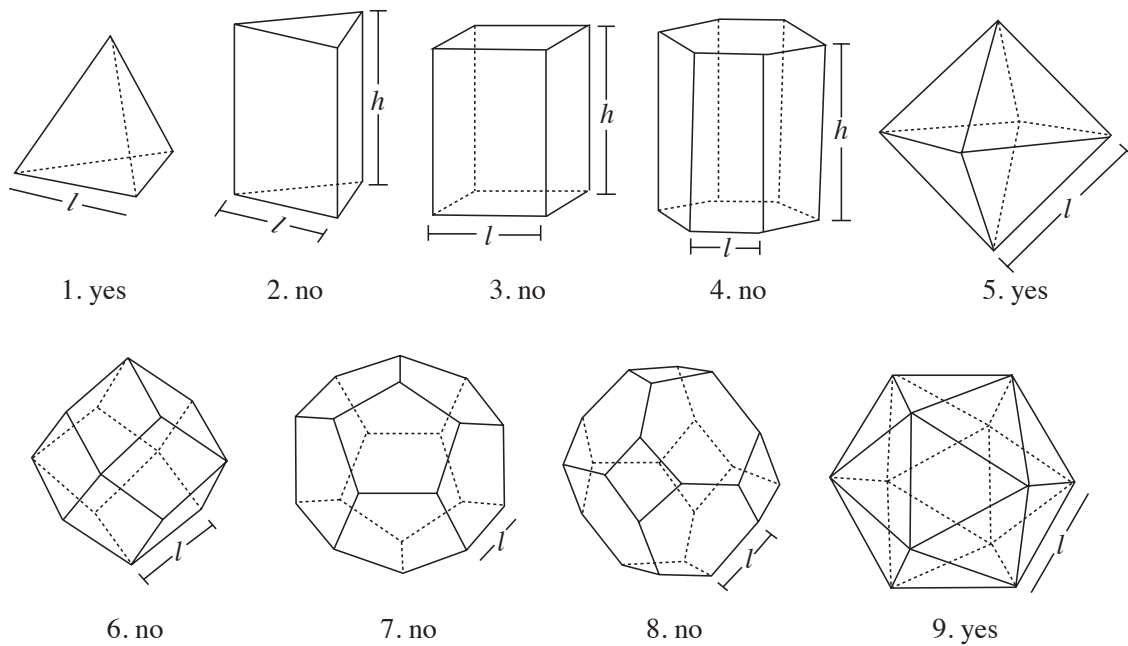


Figure 6.1. Examples of simple polyhedral cells. The polygons that can form stretching-dominated structures are labeled with yes [7].

New developments in additive manufacturing have opened up further possibilities to economically produce cellular materials with engineered structures. As a result, several studies have been conducted on the analysis and testing of mechanical properties of porous structures with innovative morphologies [8], [9]. A detailed numerical simulation of the cellular solids is an expensive task due to the large amount of micro-scale details of their morphology. Several works have used an analytical approach with major simplifications to derive the mechanical properties [10]–[12]. Some others used discrete models, assuming that each strut behaves like a slender beam [13], [14]. This assumption holds for large porosities but as the solid volume

fraction increases is not valid anymore. Due to the continuing increase in computing power, detailed discrete FE analyses are getting more and more interesting and feasible. Profiting from the periodicity of the cellular structures, homogenization methods can be used to obtain the structural properties using detailed FE analysis [15]–[17]. These models are based on a representative unit-cell, which can be either the unit cell in the periodic structures or the smallest volume representing the characteristic behavior of a random structure.

Almost all the lattices studied in the literature, such as tetrakaidecahedron, octet-truss, dodecahedron and cubic unit-cells, have anisotropic behavior [18]–[21]. D’Angelo et al. [18] reported that, compared to random foams, tetrakaidecahedron lattices behave more anisotropic under different spatial loading directions. Berger et al. [21] investigated a group of open cell and closed-cell lattice structures and demonstrated their anisotropic behavior, compared to random foams. They showed that contrary to most lattices, random foams have quasi-isotropic elastic behavior. However, adjusting the strut diameter and cell wall thickness of a unit-cell could change the anisotropy of the lattices as well.

This chapter aims at investigating the mechanical properties and anisotropic behavior of lattice structures with different porosities using a representative unit-cell approach. For this task, four lattices are considered: simple cube, tetrakaidecahedron, octet-truss and a modified octet-truss lattice. The detailed geometry of each unit-cell is created and FE models were solved using periodic boundary conditions. Using the numerical models, the elastic properties of the unit-cells are calculated in the principal unit-cell coordinate system. The elastic anisotropies of the lattices were then explored by calculating the directional dependency of the unit-cells’ elastic constants. At last, a systematic strategy is presented and applied to obtain a unit-cell with high elastic modulus and controlled anisotropy.

## 6.2 Methodology for the mechanical Characterization

### 6.2.1 Periodic boundary conditions

The methodology used here is based on the one developed by Xia et al. [16] for FE analysis of unit-cells with periodic boundary conditions. For a representative unit-cell (RUC) with periodic boundaries, the microscopic displacement field,  $\mathbf{u}$ , can be written as:

$$u_i = \bar{\epsilon}_{ik} \cdot x_k + \tilde{u}_i \quad (\tilde{u}_i \text{ periodic}), \quad (6.12)$$

where  $\bar{\epsilon}_{ik}$  is a  $3 \times 3$  macro-scale strain tensor,  $x_k$  is the Cartesian coordinate of a material point inside RUC and  $\tilde{u}_i$  is the displacement fluctuations at the boundaries of the RUC. Since the unit-cell is a point in a continuous material, the displacements must be continuous and periodic; therefore there is no separation or overlapping between the RUCs. For a hexahedral RUC with a periodic structure, one can write the following equations for every two parallel boundaries:

$$u_i^{j+} = \bar{\epsilon}_{ik} \cdot x_k^{j+} + \tilde{u}_i \quad (6.13)$$

$$u_i^{j-} = \bar{\epsilon}_{ik} \cdot x_k^{j-} + \tilde{u}_i, \quad (6.14)$$

where “ $j+$ ” and “ $j-$ ” mean on the boundary surfaces in the positive and negative directions, respectively, on the axis  $X_j$ . Because of the continuity and periodicity conditions,  $\tilde{u}_i$  must be the same on the two parallel boundaries of the RUC. Therefore, we can write a simpler form for the FE nodal displacements:

$$u_i^{j+} - u_i^{j-} = \bar{\epsilon}_{ik} \cdot (x_k^{j+} - x_k^{j-}) = \bar{\epsilon}_{ik} \cdot \Delta x_k^j \quad (6.15)$$

Note that for any two parallel boundary surfaces,  $\Delta x_k^j$  is a constant value and equal to the length of the RUC in that direction. Therefore, for a certain macroscopic strain, the right-hand side of Eq. 6.15 will be a constant value. It is assumed that the macroscopic stresses and strains in a homogenized porous medium are the volume-averages of the microscopic values [22], i.e.:

$$\bar{\sigma}_{ij} = \frac{1}{V} \int_V \sigma_{ij} \, dV \quad (6.16)$$

$$\bar{\epsilon}_{ij} = \frac{1}{V} \int_V \epsilon_{ij} \, dV, \quad (6.17)$$

where  $V$  is the volume of the RUC.



### 6.2.2 Unit-cells and the methodology

Four different unit-cells were considered in this study: simple cube, tetrakaidecahedron, octet-truss and a modified octet-truss lattice, which was created by deleting the struts lying on the  $xy$ -planes of the boundary surfaces in  $z$ -direction of the octet-truss unit-cell. The unit-cells are all shown in Figure 6.2.

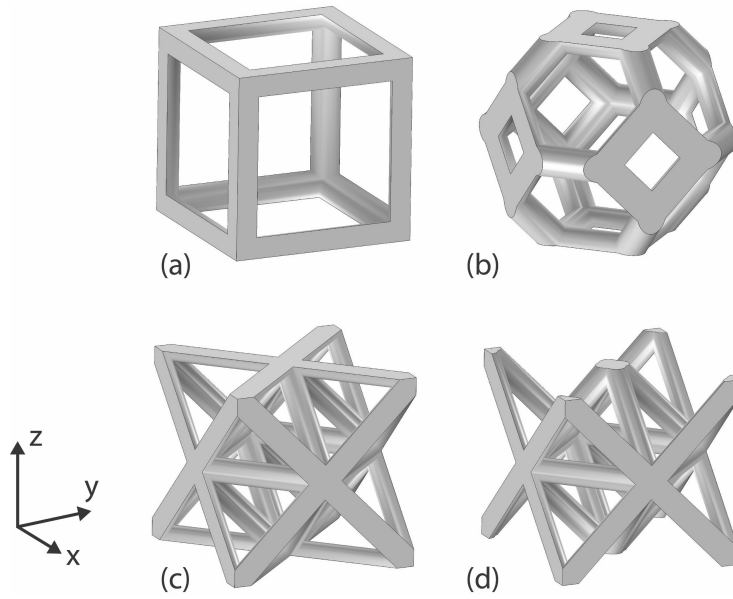


Figure 6.2. (a) simple cube, (b) tetrakaidecahedron, (c) octet-truss and (d) modified octet-truss unit-cells used in this study.

All unit-cells had a length equal to unity in each direction. From these unit-cells the octet-truss is known as a stretching-dominated structure and the rest are bending-dominated structures. The unit cells are hexahedral blocks with cubic or tetragonal symmetry. Here as a general case, the detailed procedure to obtain the elastic constants for an orthotropic material is described.

In macro-scale, for a homogeneous elastic material, Hooke's law connects the volume averaged stresses and strains:

$$\bar{\epsilon}_{ij} = \bar{S}_{ijkl} \bar{\sigma}_{kl} , \quad (6.18)$$

## Anisotropic elastic properties

where  $\bar{S}$  is the macroscale compliance matrix. The compliance matrix has 9 independent parameters for the case of the orthotropic structures, 6 parameters for tetragonal ones and 3 parameters for the ones with cubic symmetry [23]. The independent parameters for orthotropic unit-cells can be determined using 6 models by applying a small non-zero value for one of the strain components, while keeping the other ones as zero. The considered cases are listed in Table 6.1.

Table 6.1. Macroscopic strain cases used for determination of the elastic properties.

	$\bar{\epsilon}_{xx}$	$\bar{\epsilon}_{yy}$	$\bar{\epsilon}_{zz}$	$\bar{\epsilon}_{yz}$	$\bar{\epsilon}_{xy}$	$\bar{\epsilon}_{xz}$
1	0.001	0	0	0	0	0
2	0	0.001	0	0	0	0
3	0	0	0.001	0	0	0
4	0	0	0	0.001	0	0
5	0	0	0	0	0.001	0
6	0	0	0	0	0	0.001

The cases 1-3 consider pure tensile strains in the three main directions and the cases 4-6 are for the pure shear strains. For each case considering a linear elastic material, the following equations (neglecting the body forces) were solved:

$$\nabla \cdot \sigma_{ij} = 0, \quad (6.19)$$

where strains are related to stresses using the stiffness tensor,  $C$ , in Duhamel-Hooke's law:

$$\sigma_{ij} = C_{ijkl} \epsilon_{kl} \quad (6.20)$$

and the strain-displacement equation is:

$$\epsilon_{ij} = \frac{1}{2} \left( \frac{\partial u_i}{\partial x_j} + \frac{\partial u_j}{\partial x_i} \right) \quad (6.21)$$

Eq. 6.15 can be used to derive the appropriate microscopic boundary conditions from the macroscopic strain values. As an example, for case 4, the unit-cell boundary conditions were as follows:

- For the two parallel surfaces in  $x$ -direction:

$$u_x^{x+} - u_x^{x-} = 0; \quad u_y^{x+} - u_y^{x-} = 0; \quad u_z^{x+} - u_z^{x-} = 0 \quad (6.22)$$

- For the two parallel surfaces in  $y$ -direction:

$$u_x^{y+} - u_x^{y-} = 0; \quad u_y^{y+} - u_y^{y-} = 0; \quad u_z^{y+} - u_z^{y-} = 0.001 L_y \quad (6.23)$$

- For the two parallel surfaces in  $z$ -direction:

$$u_x^{z+} - u_x^{z-} = 0; \quad u_y^{z+} - u_y^{z-} = 0.001 L_z; \quad u_z^{z+} - u_z^{z-} = 0 \quad (6.24)$$

In the above equations,  $L_y$  and  $L_z$  are the unit-cell length in  $y$  and  $z$ -directions. For all the above equations with the right-hand side as zero, we applied a periodic boundary condition.

A parametric 3D model of each unit cell was developed based on the abovementioned equations and boundary conditions in Comsol Multiphysics package® (ver. 5.3) interlinked with Matlab. SiSiC was used as the constituent material of the unit-cells with  $\rho_s = 2900 \left[ \frac{\text{kg}}{\text{m}^3} \right]$ ,  $E_s = 264 \text{ MPa}$  and  $\nu_s = 0.15$  [24]. A fully coupled set of equations was computed using direct solver MUMPS. A first order discretization scheme was used for all the dependent variables. The geometries were meshed using triangular elements with the maximum element size as a function of the strut diameter (maximum element size =  $0.2 d_{st}$ ). Tetraikaidecahedron unit-cell with the smallest and largest porosities (0.95 and 0.7) were chosen for the grid convergence analysis. The analysis was performed by doubling the grid size and comparing the final results (elastic constants), which varied by less than 1%.

### 6.3 Results and discussion

#### 6.3.1 Numerical calculations of the elastic constants

The parametric study was performed to obtain the mechanical properties of the lattices for six different porosities between 0.7-0.95. The modified octet-truss unit-cell has a tetragonal symmetry with equal properties in  $x$  and  $y$  direction. Its macro-scale compliance matrix has 6 independent parameters that can be obtained by running cases 2-5 in Table 6.1. The other unit-cells have cubic symmetry with 3 independent elastic parameters, which were calculated by running cases 3 and 4. The variation of the strut diameter and the specific surface area as a function of the lattice relative density was calculated and is shown in Figure 6.3. At a certain porosity, the modified octet-truss has a larger diameter than the octet-truss unit-cell. This should be considered for the interpretation of the elastic moduli. The specific surface area is an important factor in the heat and mass transfer behavior of the porous solids. The specific surface area of the cube is much lower than the other lattices (more than 2 times lower at porosity of 0.9). An example of the calculated deformation and normalized stresses for the pure tensile and shear simulations of the octet-truss unit-cell is shown in Figure 6.4.

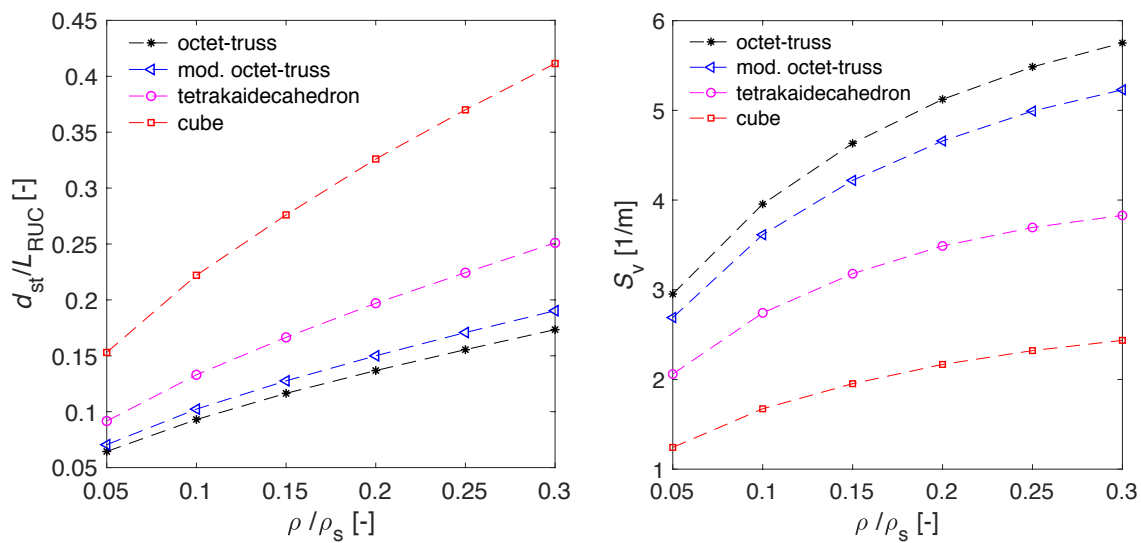


Figure 6.3. Variation of the strut diameter and the specific surface area for the studied unit-cells.

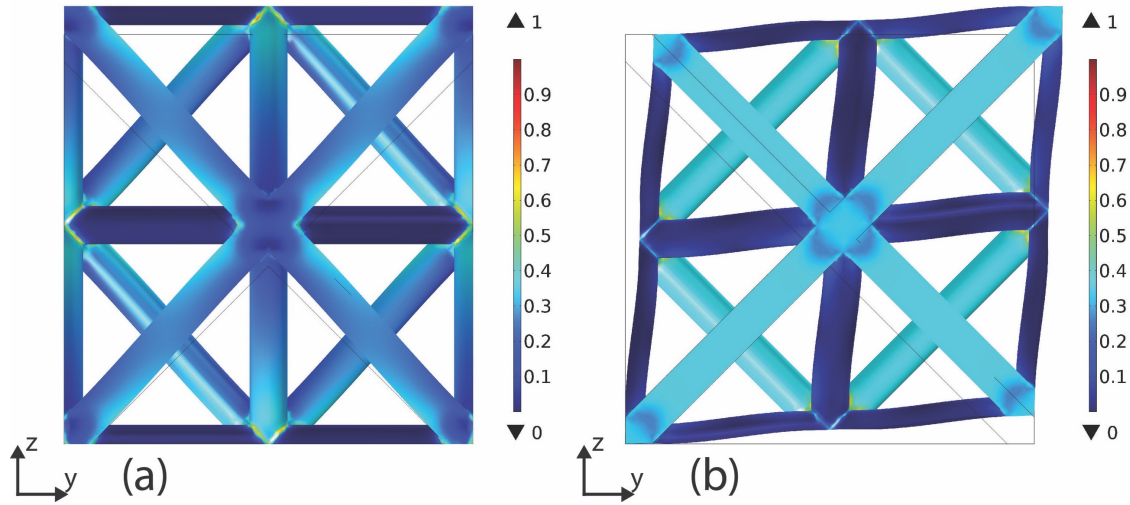


Figure 6.4. The normalized stresses and deformations (with a scale factor of 70) of the octet-truss unit-cell with a porosity of 0.9 for the two cases: (a) pure tensile in  $z$ -direction, and (b) pure shear in  $yz$ -direction.

The compliance tensor constants were calculated for each unit-cell and converted into elastic modulus (Figure 6.5), shear modulus and Poisson's ratio values (Figure 6.6). The cubic unit-cell had the highest elastic modulus in different porosities reaching a value of  $0.15E_s$  at a porosity of 0.7. This is because the cubic structure has the highest proportion of struts ( $1/3$ ) aligned with the main axes, which is desirable for uniaxial loading in the main directions, but undesirable for loading cases in other spatial directions. At large porosities, the struts can be assumed as slender beams that deform under flexural and axial loadings. In those porosities, tetrakaidecahedron and octet-truss respectively had the lowest and highest elastic moduli, because of their bending-dominated and stretching-dominated deformation mechanisms. However their values increased, reaching each other at porosity of about 0.85. On the other side, the modifications on the octet-truss slightly enhanced the elastic properties in the  $x$  and  $y$ -directions but highly decreased the values in the  $z$ -direction. The octet-truss family had also the highest shear moduli, because in a pure shear loading, their struts mainly undergo normal stresses and not flexural ones. As a result their structure is stiffer than the bending-dominated structures such as tetrakaidecahedron and cubic unit-cells. The modifications on the octet-truss resulted in elastic properties enhanced in one direction, but as well diminished in another direction.

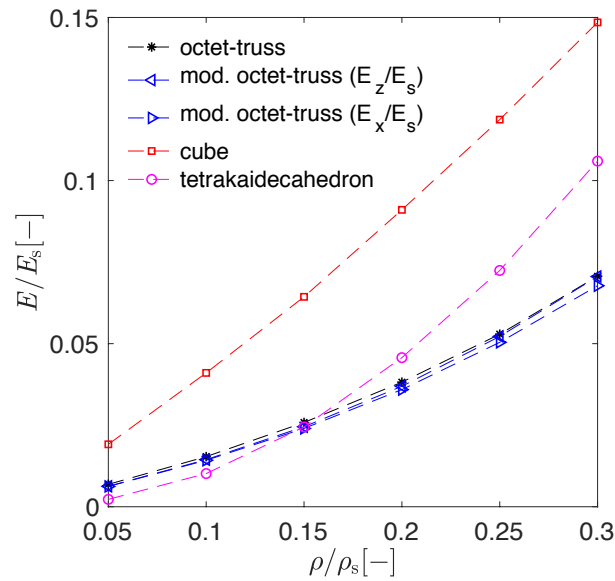


Figure 6.5. Calculated effective elastic moduli for the four unit-cells as a function of solid volume fraction. For the modified octet-truss, two values in different directions are reported due to its tetragonal symmetry.

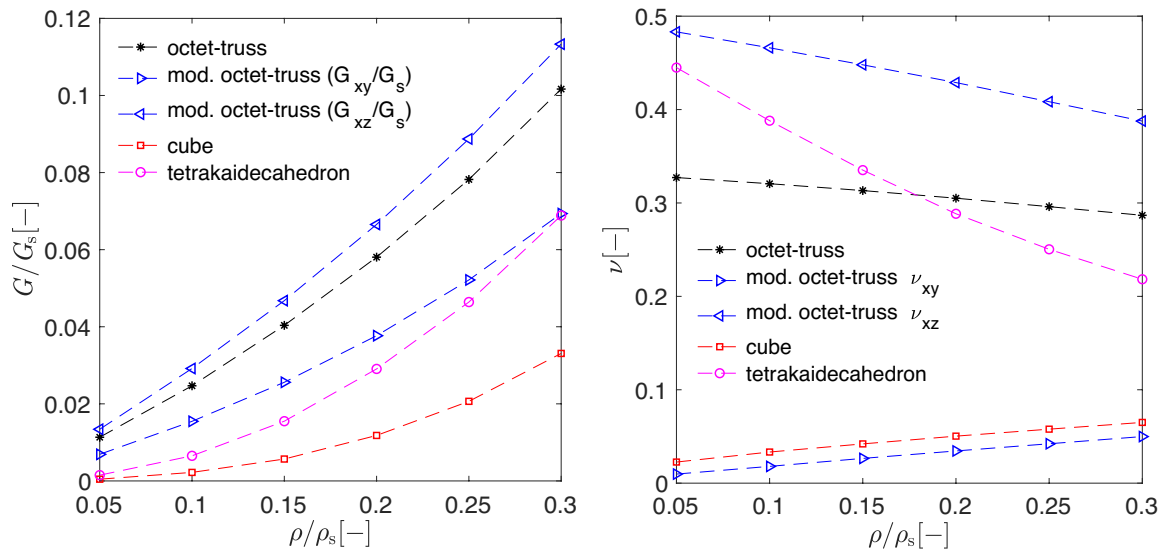


Figure 6.6. Calculated shear moduli and Poisson's ratio for the four unit-cells as a function of solid volume fraction. For the modified octet-truss, two values in different directions are reported due to its tetragonal symmetry.

The calculated effective elastic and shear moduli were used to obtain correlations in the power-law form of  $a\rho_{rel}^b$ . The calculated regression models and their coefficient of determinations are shown in

Table 6.2 and 6.3. The coefficients are different from the ones for bending and stretching-dominated structures, because the analytical calculations for the bending and stretching-dominated models are based on slender struts, which is valid just for high porosities typically above 0.9.

Table 6.2. Calculated regression models for the effective elastic modulus of the lattices in the principal directions.

	<b>cube</b>	<b>tetrakaidecahedron</b>	<b>octet-truss</b>	<b>mod. octet-truss</b>	
	<b><i>x, y, z</i></b>	<b><i>x, y, z</i></b>	<b><i>x, y, z</i></b>	<b><i>x, y</i></b>	<b><i>z</i></b>
<b><i>a</i></b>	0.612	1.329	0.386	0.390	0.421
<b><i>b</i></b>	1.182	2.103	1.422	1.466	1.495
<b>R<sup>2</sup></b>	1.000	1.000	0.998	0.998	0.998

Table 6.3. Calculated regression models for the effective shear modulus of the lattices in the principal directions.

	<b>cube</b>	<b>tetrakaidecahedron</b>	<b>octet-truss</b>	<b>mod. octet-truss</b>	
	<b><i>xy, yz, xz</i></b>	<b><i>xy, yz, xz</i></b>	<b><i>xy, yz, xz</i></b>	<b><i>xz, yz</i></b>	<b><i>xy</i></b>
<b><i>a</i></b>	0.715	0.905	0.483	0.506	0.371
<b><i>b</i></b>	2.557	2.144	1.305	1.251	1.406
<b>R<sup>2</sup></b>	1.000	1.000	0.999	0.999	0.998

### 6.3.2 Directional dependency of the elastic constants

In order to investigate the directional dependency of the elastic properties, a coordinate transformation is needed to find the compliance tensor components in the new coordinate system. Knowing the transformation matrix, the compliance tensor in the transformed coordinates can be calculated as:

$$\bar{S}_{mnop} = a_{mi}a_{nj}a_{ok}a_{pl}\bar{S}_{ijkl} \quad (6.25)$$

The compliance is a 4<sup>th</sup>-rank tensor; thus, this transformation is not a straightforward task. For this aim, we used the transformation formulations derived by Zhang et al. [25]. Using these formulations, the elastic moduli of the unit-cells in different directions were obtained (Figure 6.7). Comparing all the unit-cells studied here, we see that the cubic lattice has the highest elastic modulus in direction [001]. However, it has a large anisotropy, which results in lowest elastic modulus in the unit-cell diagonal direction [111]. As an example, at a porosity of 0.95, the elastic modulus of the cube in direction [111] is about 32 times lower than its value at the principal direction [001]. This anisotropy is much smaller in the case of tetrakaidecahedron lattice, whose minimum to maximum ratio (at porosity of 0.95) is about 1.2. On the other side, the modifications on the geometry of the octet-truss unit-cell resulted in larger anisotropy in its behavior.

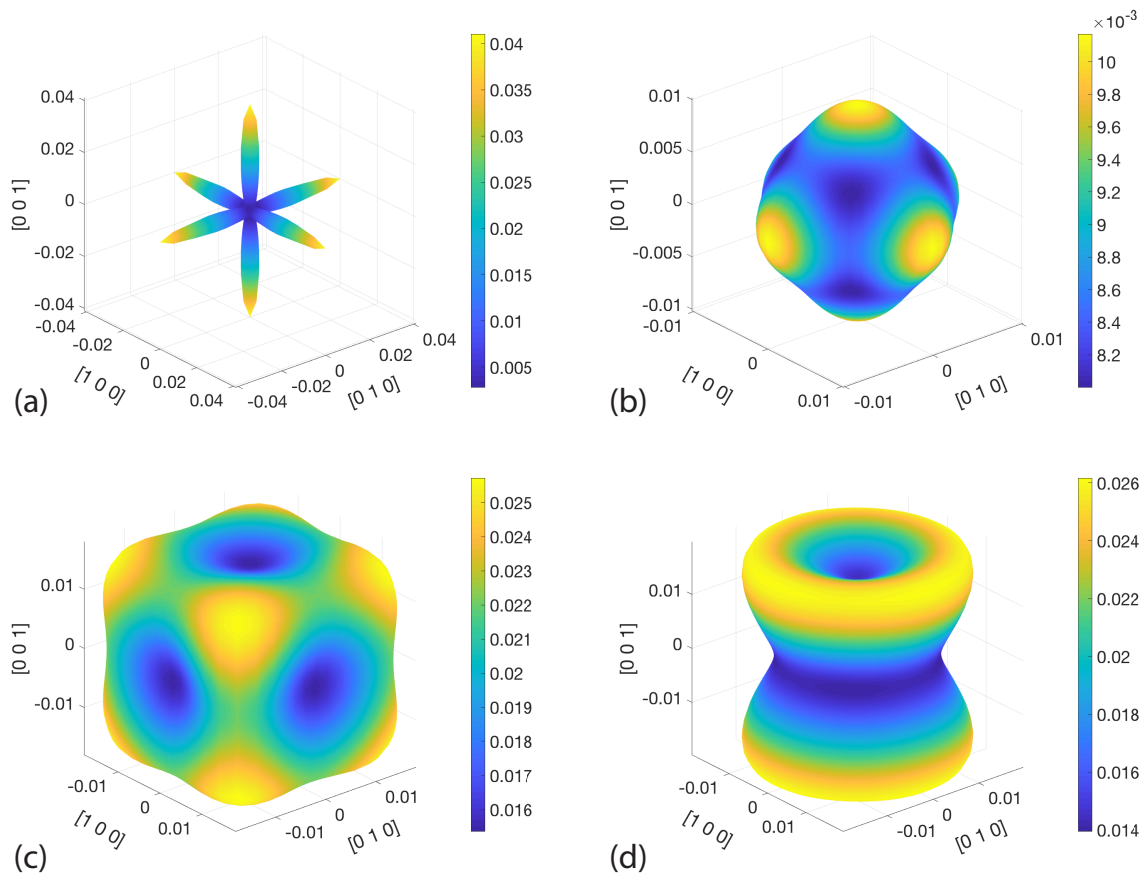


Figure 6.7. Directional dependence of the effective elastic modulus for (a) cubic, (b) tetrakaidecahedron, (c) octet-truss and (d) for lattices, all with 0.9 porosity.



To understand the variation of the anisotropy in different relative densities, the elastic moduli for the cubic structure in different directions and for different porosities are plotted in Figure 6.8. Increasing the solid volume fraction resulted in higher elastic moduli and lower anisotropy until reaching an effective elastic modulus equal to unity for an isotropic bulk material. The same behavior was observed also for the other lattices.

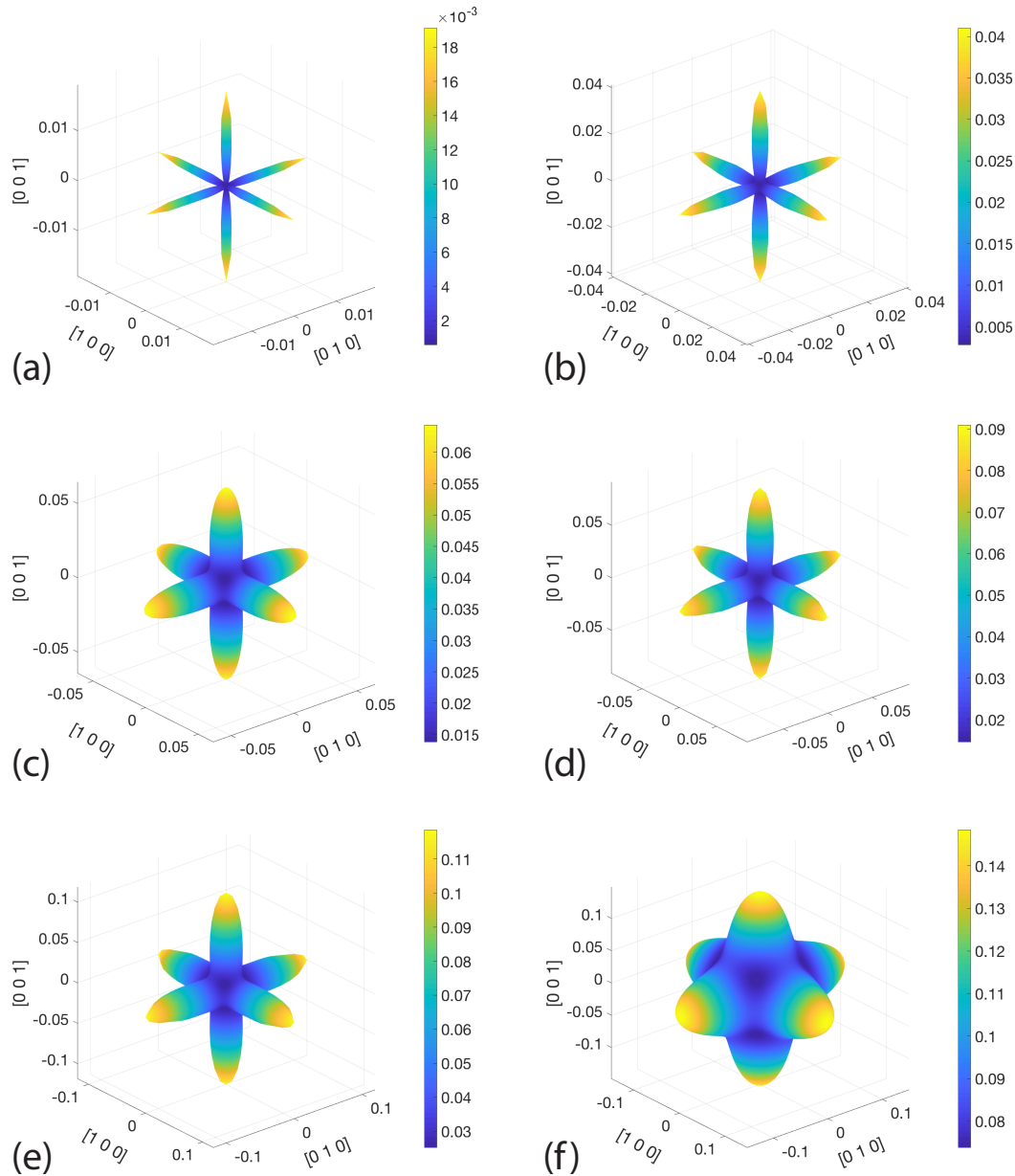


Figure 6.8. Directional dependence of the effective elastic modulus for the cubic unit-cells with (a) 0.95, (b) 0.9, (c) 0.85, (d) 0.8, (e) 0.75 and (f) 0.7 porosities.

As it can be seen, in contrary to the elastic behavior of octet-truss unit-cell, the maximum and minimum elastic moduli in a cubic unit-cell are in directions [100] and [111]. It is possible to combine various unit-cells with complimentary elastic behavior to achieve new lattices with isotropic elastic behavior [26]. Combining tetrakaidecahedron and octet-truss is not practical due to the mismatch of their nodal locations. This is not the case for the octet-truss and cubic unit-cells. Their geometry can be simply jointed forming a new unit-cell (Figure 6.9), which we refer to as the combined octet-truss-cube (COTC).

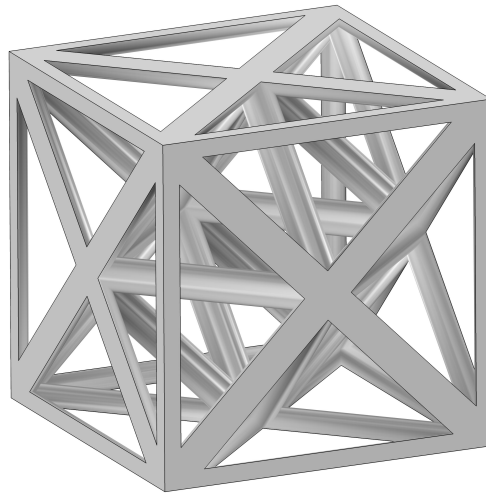


Figure 6.9. The COTC unit-cell created based on assembling a simple cubic structure with the octet-truss unit-cell.

The COTC unit-cell was modeled and solved in a parametric study for geometries, at constant porosity of 0.9 with various cube to octet-truss strut diameter ratios ( $d_{\text{cube}}/d_{\text{octet}}$  between 1-2.5). The elastic modulus calculation in the principal directions and the transformation to other directions was done using the same methodology explained earlier. The evolution of the elastic moduli with different  $d_{\text{cube}}/d_{\text{octet}}$  is demonstrated in Figure 6.10. For unit-cells with cubic symmetry, the Zener ratio can be used as a measure of their anisotropic behavior, defined as:  $\frac{2G(1+\nu)}{E}$  [27]. Zener ratio for an isotropic material is equal to unity. Therefore, plotting Zener ratio as a function of COTC unit-cell diameter ratio, one can predict that a COTC lattice with  $d_{\text{cube}}/d_{\text{octet}} = 1.208$  should have an elastically isotropic behavior. Thus, the elastic moduli of COTC unit-cell with  $d_{\text{cube}}/d_{\text{octet}} = 1.208$ , and with different porosities were calculated. Figure 6.11 demonstrates the quasi-spherical surface plot of the elastic moduli of COTC unit-cell at different porosities.

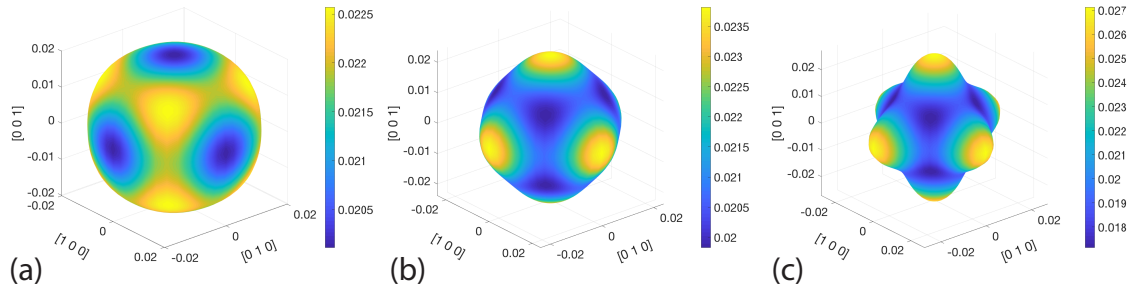


Figure 6.10. Directional surface plot of the effective elastic modulus for the COTC unit-cell with a porosity of 0.9 and (a)  $d_{\text{cube}}/d_{\text{octet}} = 1$ , (b)  $d_{\text{cube}}/d_{\text{octet}} = 1.5$  and, (c)  $d_{\text{cube}}/d_{\text{octet}} = 2$ .

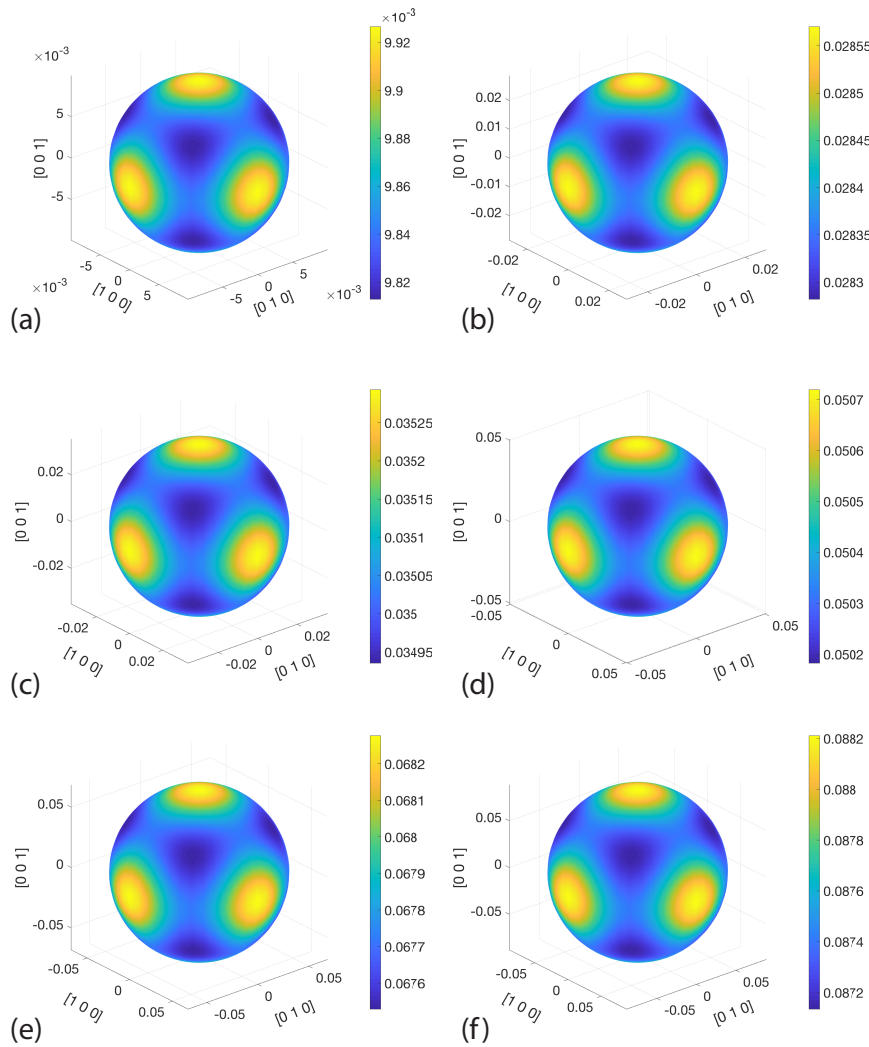


Figure 6.11. Directional dependence of the effective elastic modulus for the COTC unit-cells with  $d_{\text{cube}}/d_{\text{octet}} = 1.208$ , and a porosity of (a) 0.95, (b) 0.9, (c) 0.85, (d) 0.8, (e) 0.75 and (f) 0.7.

The effective elastic modulus of COTC together with the other analyzed unit-cells in this work are shown in Figure 6.12 (left). As expected, COTC unit-cell has an elastic modulus between the ones from the cubic and octet-truss structures.

For the comparison between the unit-cells an equivalent Zener ratio is defined as:

$$\alpha_{Zener} = \frac{1}{3} \left[ \frac{2G_{xy}(1 + \nu_{xy})}{E_x} + \frac{2G_{yz}(1 + \nu_{yz})}{E_y} + \frac{2G_{zx}(1 + \nu_{zx})}{E_z} \right] \quad (6.26)$$

Figure 6.12 (right) demonstrates the Zener ratio at different porosities for all the unit-cells. As explained earlier, the modifications in octet-truss resulted in larger elastic anisotropies. The cubic structure had the lowest values due to its low shear modulus. Tetrakaidecahedron had a smaller anisotropy compared to octet-truss family and the cubic unit-cell. The designed COTC unit-cell showed an isotropic behavior, with a Zener ratio almost equal to unity in all porosities.

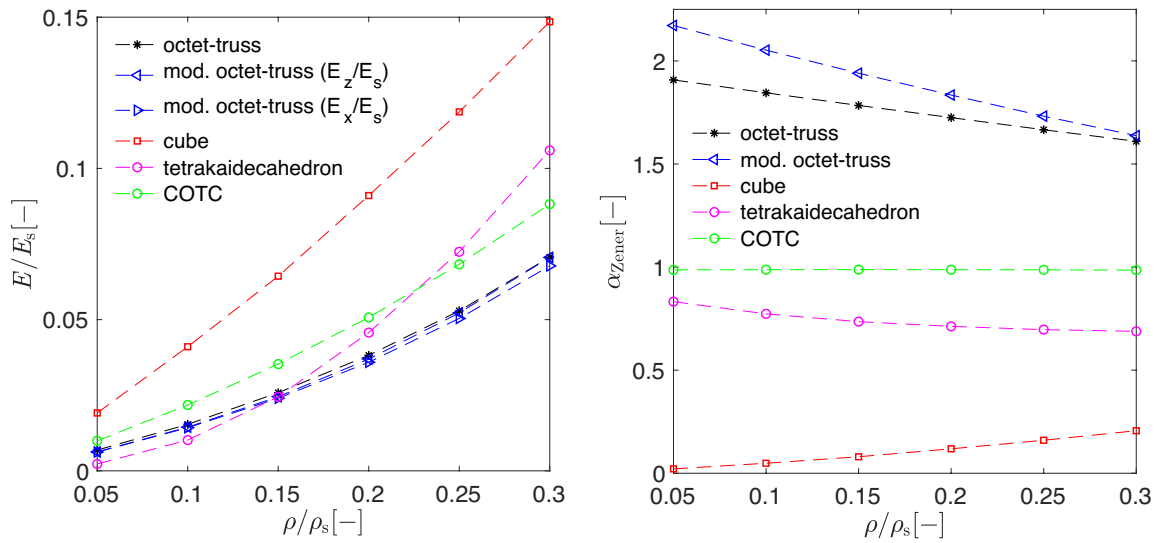


Figure 6.12. Left: the effective elastic moduli for all the analyzed unit-cells in this work. Right: the Zener anisotropy ratio for all the unit-cells with cubic symmetry.

It should be pointed out that this design strategy doesn't necessarily give a solution for any combination of unit-cells. On one side, the elastic behavior of the unit-cells must complement

each other in different spatial directions. On the other side, one needs to ensure that the obtained solution is not sensitive to the input variables such as the  $d_{\text{cube}}/d_{\text{octet}}$  and the porosity, in order to ensure the manufacturability of the structure within the production tolerances.

The calculated elastic properties in this chapter can be used in continuum models to analyze the macroscopic mechanical response of the material (see the appendix in section 6.6). Cellular ceramics are often used in high-temperature environments with large thermal fluxes, and therefore thermo-mechanical investigations are often required. Numerical studies can be implemented using multi-physics models, coupling fluid flow and heat transfer to solid mechanics. For small deformations, a sequentially coupled approach can be used, where the temperature field is firstly calculated and used as the input for the stress analysis. Direct pore-level modeling can be then used in combination with the continuum model in order to estimate the microscopic stress states in the zones of interest.

## **6.4 Conclusions**

The elastic properties of four different lattice structures (cube, tetrakaidecahedron octet-truss and modified octet-truss) were numerically calculated using a unit-cell method with periodic boundary conditions. For cube, tetrakaidecahedron and octet-truss, due to their cubic symmetry, just two cases with pure tensile and shear loadings were used. For the case of the modified octet-truss, as its properties are different in two directions, four loading cases were used to obtain the compliance tensor of the lattice. The directional elastic modulus of each unit-cell was calculated in different porosities ranging between 0.7-0.95.

The results showed that in the principal unit-cell directions, the cubic lattice has highest elastic moduli for different porosities due to its struts aligned with the loading direction. However, its elastic modulus was largely direction dependent. The tetrakaidecahedron had the lowest elastic modulus at large porosities because of its bending-dominated deformation mechanism. In those porosities, the octet-truss family is stiffer as their struts mainly undergo normal stresses due to their stretching-dominated deformation. The tetrakaidecahedron and cubic unit-cells respectively had the smallest and largest elastic anisotropy. At the porosity of 0.95, their elastic modulus reached a minimum to maximum ratio of 1.2 and 32, correspondingly. On the other side, the modifications on the octet-truss unit-cell increased its elastic anisotropy.

A new unit-cell was presented, as an assembly of the cubic and octet-truss structures. Proper strut diameters ratio of the two unit-cells was obtained in a parametric study to find a unit-cell with isotropic elastic behavior. The new unit-cell had high elastic modulus, higher than

the octet-truss family, and showed almost perfect isotropy at various porosities. The presented approach can be used to obtain unit-cells with a controlled anisotropy.

## 6.5 Reference

- [1] L. J. Gibson and M. F. Ashby, *Cellular Solids: Structure and Properties*. Cambridge University Press, 1999.
- [2] R. Brezny and D. J. Green, “Uniaxial Strength Behavior of Brittle Cellular Materials,” *J. Am. Ceram. Soc.*, vol. 76, no. 9, pp. 2185–2192, Sep. 1993.
- [3] W. Acchar, F. B. M. Souza, E. G. Ramalho, and W. L. Torquato, “Mechanical characterization of cellular ceramics,” *Mater. Sci. Eng. A*, vol. 513–514, pp. 340–343, Jul. 2009.
- [4] F. A. Costa Oliveira, S. Dias, and J. Cruz Fernandes, “Thermal Shock Behaviour of Open-Cell Cordierite Foams,” *Mater. Sci. Forum*, vol. 514–516, pp. 764–767, 2006.
- [5] R. Brezny, D. J. Green, and C. Q. Dam, “Evaluation of Strut Strength in Open-Cell Ceramics,” *J. Am. Ceram. Soc.*, vol. 72, no. 6, pp. 885–889, Jun. 1989.
- [6] V. S. Deshpande, M. F. Ashby, and N. A. Fleck, “Foam topology: bending versus stretching dominated architectures,” *Acta Mater.*, vol. 49, no. 6, pp. 1035–1040, Apr. 2001.
- [7] M. F. Ashby, “The properties of foams and lattices,” *Philos. Trans. R. Soc. Lond. Math. Phys. Eng. Sci.*, vol. 364, no. 1838, pp. 15–30, Jan. 2006.
- [8] O. Al - Ketan, M. Pelanconi, A. Ortona, and R. K. A. Al - Rub, “Additive manufacturing of architected catalytic ceramic substrates based on triply periodic minimal surfaces,” *J. Am. Ceram. Soc.*, vol. 0, no. 0.
- [9] E. C. Hammel, O. L.-R. Ighodaro, and O. I. Okoli, “Processing and properties of advanced porous ceramics: An application based review,” *Ceram. Int.*, vol. 40, no. 10, Part A, pp. 15351–15370, Dec. 2014.
- [10] V. S. Deshpande, N. A. Fleck, and M. F. Ashby, “Effective properties of the octet-truss lattice material,” *J. Mech. Phys. Solids*, vol. 49, no. 8, pp. 1747–1769, Aug. 2001.
- [11] H. X. Zhu, J. F. Knott, and N. J. Mills, “Analysis of the elastic properties of open-cell foams with tetrakaidecahedral cells,” *J. Mech. Phys. Solids*, vol. 45, no. 3, pp. 319–343, Mar. 1997.
- [12] R. M. Sullivan, L. J. Ghosn, and B. A. Lerch, “A general tetrakaidecahedron model for open-celled foams,” *Int. J. Solids Struct.*, vol. 45, no. 6, pp. 1754–1765, Mar. 2008.

- [13] M. H. Luxner, J. Stampfl, and H. E. Pettermann, “Finite element modeling concepts and linear analyses of 3D regular open cell structures,” *J. Mater. Sci.*, vol. 40, no. 22, pp. 5859–5866, Nov. 2005.
- [14] M. Smith, Z. Guan, and W. J. Cantwell, “Finite element modelling of the compressive response of lattice structures manufactured using the selective laser melting technique,” *Int. J. Mech. Sci.*, vol. 67, pp. 28–41, Feb. 2013.
- [15] S. Arabnejad and D. Pasini, “Mechanical properties of lattice materials via asymptotic homogenization and comparison with alternative homogenization methods,” *Int. J. Mech. Sci.*, vol. 77, pp. 249–262, Dec. 2013.
- [16] Z. Xia, Y. Zhang, and F. Ellyin, “A unified periodical boundary conditions for representative volume elements of composites and applications,” *Int. J. Solids Struct.*, vol. 40, no. 8, pp. 1907–1921, Apr. 2003.
- [17] Z. Fang, B. Starly, and W. Sun, “Computer-aided characterization for effective mechanical properties of porous tissue scaffolds,” *Comput.-Aided Des.*, vol. 37, no. 1, pp. 65–72, Jan. 2005.
- [18] C. D’Angelo, A. Ortona, and P. Colombo, “Influence of the loading direction on the mechanical behavior of ceramic foams and lattices under compression,” *Acta Mater.*, vol. 61, no. 14, pp. 5525–5534, Aug. 2013.
- [19] H. L. Fan and D. N. Fang, “Anisotropic Mechanical Properties of Lattice Grid Composites,” *J. Compos. Mater.*, vol. 42, no. 23, pp. 2445–2460, Dec. 2008.
- [20] Q. Zheng, S. Ju, and D. Jiang, “Anisotropic mechanical properties of diamond lattice composites structures,” *Compos. Struct.*, vol. 109, pp. 23–30, Mar. 2014.
- [21] J. B. Berger, H. N. G. Wadley, and R. M. McMeeking, “Mechanical metamaterials at the theoretical limit of isotropic elastic stiffness,” *Nature*, vol. 543, no. 7646, pp. 533–537, Feb. 2017.
- [22] R. Hill, “Elastic properties of reinforced solids: Some theoretical principles,” *J. Mech. Phys. Solids*, vol. 11, no. 5, pp. 357–372, Sep. 1963.
- [23] J. F. Nye, *Physical properties of crystals: their representation by tensors and matrices*, 1st published in pbk. with corrections, 1984. Oxford [Oxfordshire] : New York: Clarendon Press ; Oxford University Press, 1984.
- [24] C. D’Angelo, A. Ortona, and P. Colombo, “Finite element analysis of reticulated ceramics under compression,” *Acta Mater.*, vol. 60, no. 19, pp. 6692–6702, 2012.



- [25] Y. Zhang and V. Ji, “General compliance transformation relations for all seven crystal systems,” *Sci. China Phys. Mech. Astron.*, vol. 56, no. 4, pp. 694–700, Apr. 2013.
- [26] S. Xu, J. Shen, S. Zhou, X. Huang, and Y. M. Xie, “Design of lattice structures with controlled anisotropy,” *Mater. Des.*, vol. 93, pp. 443–447, Mar. 2016.
- [27] C. Zener, *Elasticity and anelasticity of metals*. University of Chicago press, 1948.

### 6.6 Appendix

Cellular ceramics are often used in applications with large thermal loadings that induce stresses in the structure. A numerical analysis of such processes with the exact geometry of the porous structures is expensive, and sometime unfeasible, due to the complex geometry of the cellular structure. To resolve this problem, homogenized macroscale approach (continuum models) can be used, where the porous structure is modeled using its volume averaged properties. The continuum model can be combined with a discrete model to capture the microscale response in the zones of interest. Here we propose a modeling guideline with a simple example, where heat transfer, fluid flow and solid mechanics are coupled.

The example is a tube filled with porous medium, radiated on the top side with a cold flow passing within the porous zone (Figure 6.13). The porous structure is made of a simple unit-cell, which is basically a cube with a spherical void in the middle. This unit cell is chosen just for simplicity and can be substituted with the desired lattice.

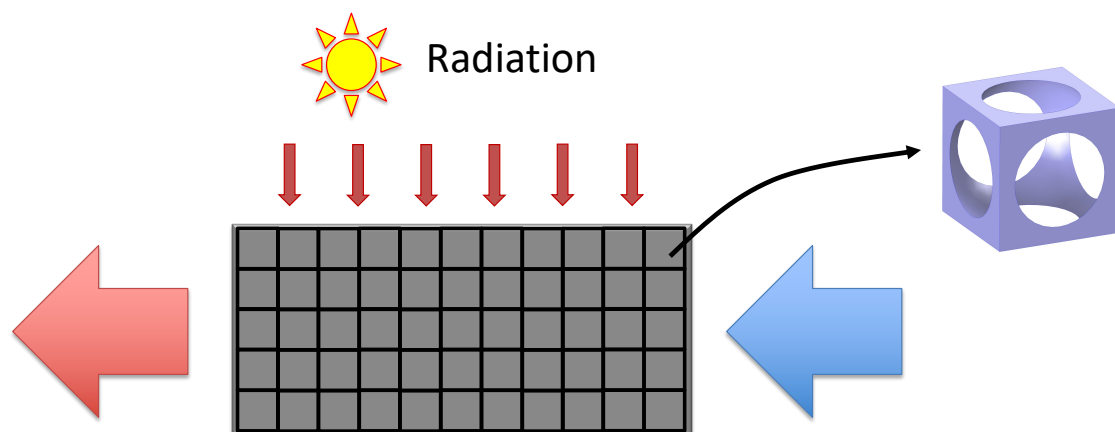


Figure 6.13. The example used for the figures in this section. A tube filled with porous media, radiated on the top and with a cold fluid flowing within the porous domain. The porous medium has a simple representative unit-cell, which is a cube with a spherical void in the middle.

A coupling between the fluid flow, heat transfer and the solid mechanics is required to obtain the response of the structure to the thermally induced stresses. For small deformations (as in many ceramics), a sequentially coupled approach can be used, where the temperature field is firstly calculated and used as the input for the stress analysis. In order to obtain the temperature distribution, a continuum model can be used coupling the fluid flow with heat

transfer equations. However these models, typically need several macroscopic parameters such as pressure-drop characteristics and volumetric heat transfer coefficient and effective thermal conductivity of the porous structure. These values can be calculated either numerically or experimentally. The calculated temperature distribution can be used for stress analysis in a continuum model. The effective elastic constant are also needed for this step. The flowchart of this process is depicted in Figure 6.14.

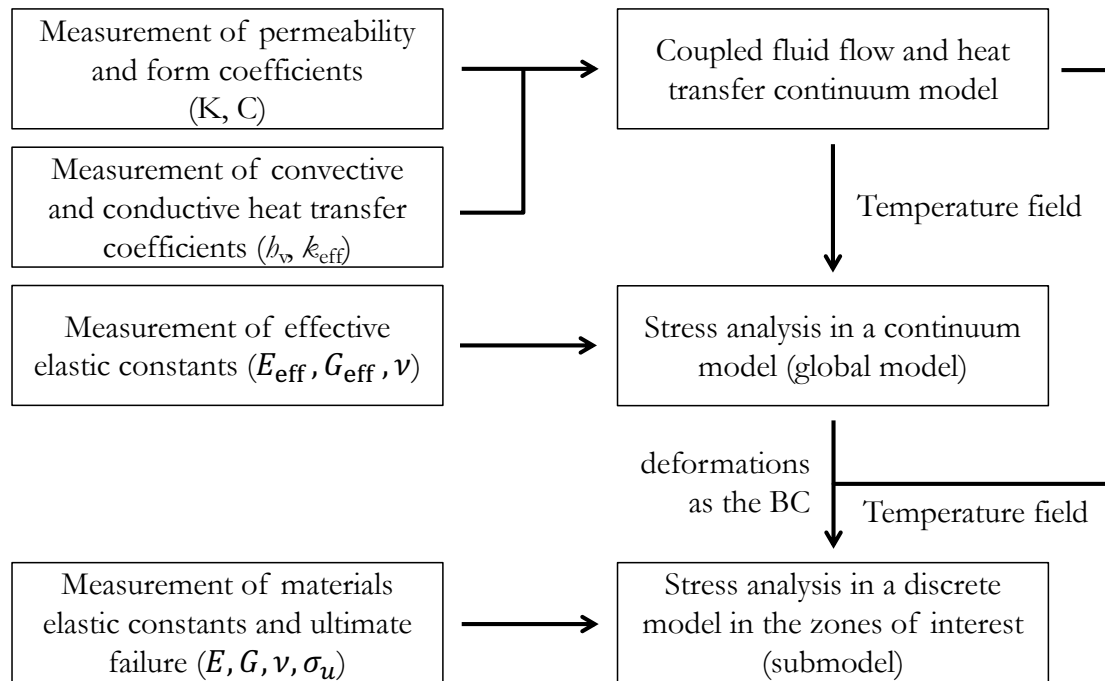


Figure 6.14. Flowchart of the proposed procedure for coupling fluid flow, heat transfer and solid mechanics and creation of a submodel in the zone of interest.

In some cases where the microscale deformation response of the structure is required, a submodel for the zone of interest can be created and solved by a discrete modeling approach. To do this, the solution of the global model (the deformation field) is prescribed as the boundary conditions on the cutting interface of the submodel. The temperature field is also obtained from the continuum thermo-fluid model. In order to use the submodeling method two considerations are to be accounted for:

- The global model should be accurate enough to give correct results for the deformations on the “cutting interface” that will be applied as the inlet BCs for the submodel. This also depends on the accuracy of the effective elastic constant.
- The submodel should be cut sufficiently far from the critical domain, where the stress responses are required.

Figure 6.15 shows the temperature distribution on the global model and the submodel and their deformation and stress results. These results are just to clarify the proposed modeling procedure and are not necessarily valid.

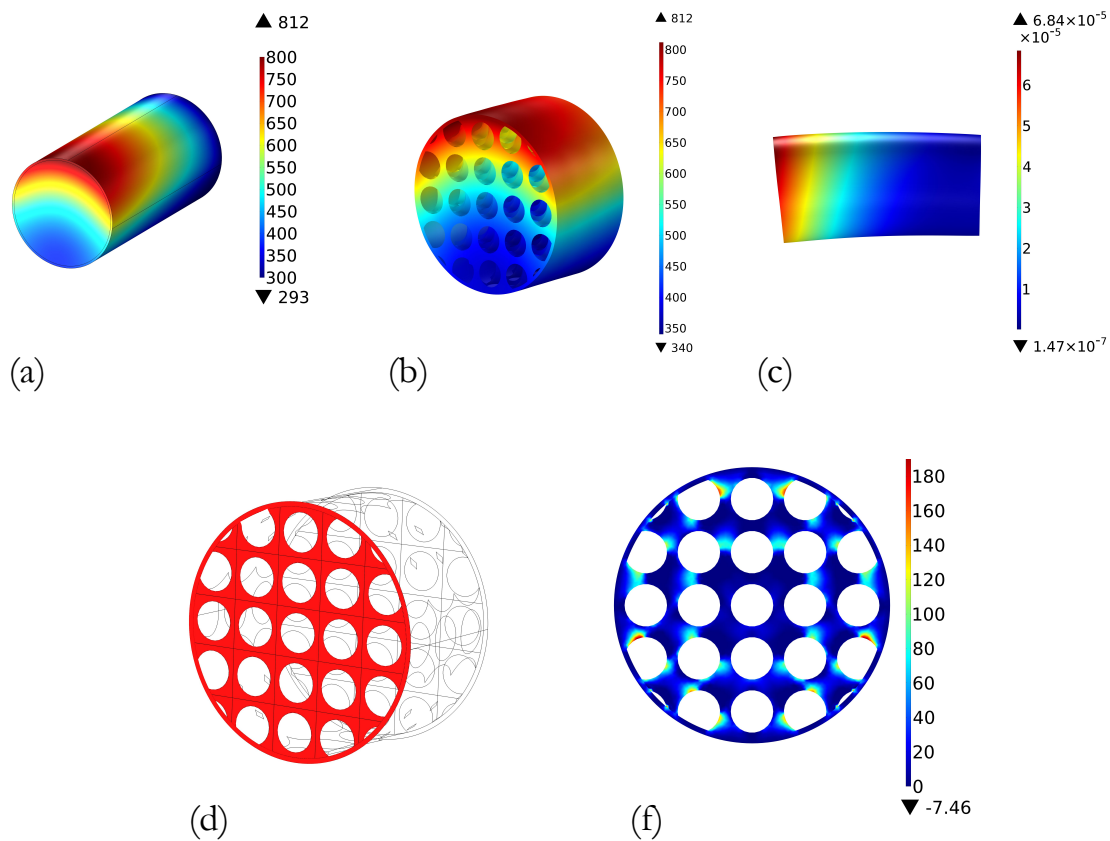


Figure 6.15. (a) Temperature distribution obtained from the continuum thermo-fluid model, (b) the temperature distribution mapped on the discrete model, (c) the deformations obtained from the continuum stress model and, (d and f) the stress results from the discrete submodel on the red surface at the end of the tube.

## 7 Conclusions and prospects

In this thesis, ceramic structures are investigated with a focus on their morphological design, their characterization and their use in a novel application, i.e. as high-temperature heat storage unit. The focus of the study was on SiSiC structures manufactured via replica technique and infiltration. However, the developed design tools, methodologies and certain findings, such as the calculated transport and mechanical properties, can be extended to porous materials made by other methods and with other materials. The choice of SiSiC structures was due to their excellent bulk properties at high-temperatures ( $>1000\text{ }^{\circ}\text{C}$ ), which makes them attractive candidates for high-temperature applications in oxidative environments with large thermal fluxes ( $\sim 1000\text{ kW/m}^2$ ). These structures are often used in environments requiring multifunctional capabilities such as: heat absorption, insulation or dissipation, structural load bearing, fluid flow percolation and enhanced mass transfer. Therefore, study of their behavior in different physics, namely, their heat and mass transport, mechanical, and oxidation behavior, is necessary for their performance prediction in the real environments.

We first studied the use of random foams as heat transfer enhancing fin structures in high-temperature latent heat thermal energy storage (LHTES) units. We investigated the link between the morphology and the multi-physical behavior in lattice structures with different unit-cells, so as to use the optimized microstructure for the heat storage application. Experimental and numerical investigations were then carried out to quantify heat transport and pressure drop characteristics, oxidation behavior and mechanical properties of the SiSiC foam structures.

In *Chapter 2*, a detailed methodology was presented to design optimized high-temperature LHTES units, employing foams as a means to enhance the heat transfer between the phase change material and the heat transfer fluid. The shell and tube model was chosen with a parallel configuration, where the flow channel area was filled with ceramic foam. The design

## Conclusions and prospects

---

procedure was based on a systematic parametric study that provided various storage systems with minimum exergetic efficiency of 0.95 and maximum discharging time of 1 h, followed by a multi-objective optimization to achieve the storage unit sizing with maximized energy density and effectiveness. The parametric study was developed using three input design variables: encapsulation diameter and length, respectively ranging between 20-100 mm and 200-1000 mm, and the pore diameter of the foam ranging 1.25-5 mm. The storage units were modeled using an analytical-numerical approach obtaining energy density and effectiveness of the systems as the output responses. LHTES units with effectiveness as large as 0.95 and energy densities as large as 810 MJ/m<sup>3</sup> were obtained within the chosen design space. Increasing the encapsulation diameter diminished the energy density and the effectiveness and, on the other side, increasing the encapsulation length or decreasing the foam's pore diameter decreased the packing factor of the LHTES unit. A trade-off must be found among these performance metrics and more practical considerations, such as manufacturability, also have to be considered. To find proper LHTES unit sizing, a multi-criteria optimization study was performed using surrogate models, which were developed based on the results of the parametric study. Finally, the optimization results were validated by performing finite element simulations of the models with the predicted design factors. For these models, the comparison between predictions and finite element simulations showed a maximum deviation of 6.4%.

Overall, it was revealed that the extended surface area, provided by employing porous media, is essential for LHTES systems with high energy densities, where a large amount of thermal energy is discharged. Additional studies are required for a complete charging/discharging process as the next step. These results were the motivation for further investigations on the behavior of SiSiC structures in such high-temperature environments and understanding the link between their morphology and multi-physical characteristics, which were addressed individually in chapters 3 to 6.

When thinking about characterization of engineered structures, the first question is about how to design these structures. Due to the large number of geometrical features presented in the structure of cellular solids, alternative design approaches are required to provide platforms able to create geometries that can be used for computer simulations or additive manufacturing. *Chapter 3* presented three alternative design methods to create cellular structures with regular and irregular arrangements. The first approach was based on creation of a single unit-cell and its repetition in different spatial directions to fill the desired enclosure. This approach, while being simple, provided the basic tool to design the specimens used in this thesis. A second approach was developed in order to create unstructured lattices within complex enclosures. The idea was based on mapping lattices with cubic symmetry within hexahedral mesh elements. This approach provides the proper tool in order to design porous structures with variable unit-cells, cell size and porosities. The third approach was based on

the creation of Voronoi structures with different input seed points. This approach is flexible, and capable of generation of cubic, tetrakaidecahedron and hexagonal lattices in any spatial orientation, and also joining different lattices by generation of a mid-layer Voronoi structure. In general, different lattice structures such as Weaire-Phelan, rotated cube, hexagonal, tetrahedral, and any other unit-cell with cubic symmetry can be generated by these approaches. Numerical tools based on these ideas were developed to design the lattices used in the experimental campaigns presented in chapter 4 and 5. Future works can be oriented toward development of a unique platform incorporating the created design tools, in order to use them in conjunction with each other.

Using the developed design tools rotated-cube, tetrakaidecahedron and Weaire -Phelan lattices were designed and manufactured. Pressure drops and heat transport characteristics of these structures were investigated in *chapter 4*. Commercial random foams with similar structural parameters (porosity and cell density) were also manufactured for comparison. Permeability and form coefficients were obtained by pressure drop experiments. A combined experimental-numerical approach was used to estimate the volumetric heat transfer coefficients of the specimens. The numerical model consisted of solving the Brinkman equations with Forchheimer corrections coupled with two homogeneous phases at local non-thermal equilibrium. It was observed that the production of the specimens using replica technique had caused undesirable cell window clogging, specifically in smaller cell windows in tetrakaidecahedron and Weaire-Phelan samples, which resulted in more flow resistance and higher tortuosity. As a result, the pressure drop of Weaire-Phelan and tetrakaidecahedron lattices was 2-3 times higher than the rotated cube and random foam. On the other side, rotated-cube lattice and the foam had slightly lower convective heat transfer, which can be mainly explained by their lower specific surface area.

It was demonstrated that the overall transport properties of the porous structures are not only a function of the cell size and porosity but also depend on the geometrical anomalies, which can deviate the flow path, increasing the flow resistance and the thermal dispersion. Correlations were proposed for prediction of the pressure drop and convective heat transfer coefficients of each structure, valid for the range of  $70 < Re < 250$ . A drawback of the manufacturing technique used in this work was the presence of undesirable geometrical anomalies such as agglomeration of material in the strut joints and pore clogging, which forms especially in structures having small cell windows. These problems can be removed by further improvements in the replication process or using direct additive manufacturing (AM) techniques. However direct AM techniques for production of SiC-based materials are still under development. The heat transfer experiments were performed with a horizontal tubular furnace. As a result, there was an asymmetric effect of the buoyancy forces on the temperature field, which had to be considered. We recommend a vertical configuration for the future

## Conclusions and prospects

---

studies, which can simplify the temperature measurements, and decrease the numerical model to an axis-symmetric case. Besides, it is advisable to tailor the experimental apparatus for the volumetric heat transfer measurements of the porous structures; for example: the temperatures and pressures must be measured right before and after the porous medium, and the inlet flow (preferably with uniform velocity and temperature) should be introduced directly into the samples. Therefore, the long tube could be excluded from the numerical domain, resulting in more economic calculations and more accurate predictions. An attractive work for the future studies is the establishment of a library containing different unit-cells with their morphological and thermo-fluid transport properties at low and high Reynolds numbers. Such a library can be readily used by engineers in order to design and optimize processes involving fluid flow and heat transfer.

Early-stage oxidation investigation of SiSiC structures was presented in *Chapter 5*. The study was performed on five different morphologies: straight cube, rotated cube, tetrakaidecahedron, modified octet and random foam. Two different tests were considered: thermal tests in calm air in an electric furnace (group I), and thermo-cyclic oxidation in a porous burner (group II). Both tests in the furnace and porous burner were performed at 1400 °C. It was revealed that at those temperatures, there are two main factors limiting the performance of SiSiC materials: silicon alloy bead formation, and combustion products such as H<sub>2</sub>O and CO<sub>2</sub>. Silicon alloy melted out of the samples, introducing more porosity in the microstructure. This resulted in decreased retention strength and rapid oxidation on the surface and inside porosities. High partial pressure of H<sub>2</sub>O in the combustion environment of the porous burner resulted in a porous silica glass layer on the hot zones of samples group II. In addition to these two phenomena, ring-shape silica layers were formed on single struts and along the fluid flow. A mechanism was proposed explaining that the ring-shape oxidation layer was made by the initial silica formation in the stagnation point of the flow and its gradual growth along the gas flow. The severity of oxidation in samples of group II was different depending on the lattice morphology. It was observed that straight cubic lattices, having more struts perpendicular to the gas flow direction, offer more stagnation zones and as well a higher oxidation rate. It was revealed that the presence of impurities such as iron, titanium and chromium decrease the melting point of the free silicon, facilitating the oxidation process. Several suggestions can be made to manufacture specimens with lower oxidation rates for the future studies such as: decreasing the free silicon content from the structures, employing a silicon-based alloy (instead of pure silicon) with higher melting point, and formation of a protecting coating layer on the structures prior to their use in high-temperature environments.

In *chapter 6*, the elastic properties of four different lattice structures (cube, tetrakaidecahedron octet-truss and modified octet-truss) were numerically calculated using a unit-cell method with



periodic boundary conditions. Cube, tetrakaidecahedron and octet-truss unit-cells have a cubic symmetry and therefore their properties were calculated using simple tensile and shear loadings in one direction. For the case of the modified octet-truss as its properties are different in two directions, four loading cases were used. The calculations were performed on unit-cells with different porosities ranging 0.70-0.95 and were then used to obtain tridimensional orientation-dependent polar surfaces to visualize the anisotropy of each structure. In general, in principal directions of the unit-cells, tetrakaidecahedron had the lowest value at a porosity of 0.95 and simple cube had the highest elastic modulus in all porosities. The tetrakaidecahedron had the lowest anisotropy, while the cubic structure showed a highly anisotropic behavior with its elastic modulus varying more than an order of magnitude between its minimum and maximum values. A new structure was created as a combination of two unit-cells (cube and octet-truss) with different strut diameters. The strut diameters ratio was calculated in a parametric study in order to achieve a quasi-isotropic structure at porosity of 0.9. The combined cubic-octet-truss unit-cell had high elastic modulus, comparable to the cubic unit-cell in its principal directions, and showed almost perfect isotropy at porosity of 0.9. The isotropy of the unit-cell was slightly decreased in other porosities. The presented approach can be successfully used in order to obtain unit-cells with controlled anisotropy. Porous parts with such unit-cells can be designed using the 3D numerical tools developed and presented in chapter 3. They can be produced via 3D printing; however, due to the complexity of the unit-cell it cannot be easily manufactured by the replication technique used in this thesis. As ceramic structures are often used in high-temperature applications, where they are often subjected to thermal loading conditions, a future study on their thermo-mechanical behavior is advisable. Such an analysis can be performed using continuum models by sequentially coupling heat transfer and solid mechanics. Direct pore-level simulations can be then used in combination with the continuum model, in order to capture microscale deformations in the critical zones.

Overall, this thesis aimed to investigate the behavior of SiSiC structures in high-temperature environments from one side, and shed light on the link between the morphology and multi-physical properties of porous structures from the other side. The methodology developed for the optimal design of the foam-enhanced LHTES unit was an example that can be extended for other similar applications. The calculated transport coefficients and elastic properties can be directly used in continuum models coupling fluid flow, heat/mass transfer or solid mechanics. On the other side, new potentials for creation of porous structures with controlled anisotropy are demonstrated. At last, the oxidation tests uncovered the limitations of the use of SiSiC structures and paved the way for further investigations on manufacturing techniques in order to diminish the oxidation rates in elevated temperatures.



# Curriculum Vitae

## Ehsan Rezaei

Email: [ehn.rezaei@gmail.com](mailto:ehn.rezaei@gmail.com)

Date of birth: Feb. 22, 1987

Nationality Iranian

### **EDUCATION**

---

- 2014-2019** Ph.D in Mechanical Engineering, Doctoral Program in Energy  
**Swiss Federal Institute of Technology Lausanne (EPFL)**  
**Thesis** Multi-physical characterization of cellular ceramics for high-temperature applications.
- 2011-2013** M.Sc. in Engineering with specialization in Industrial Technologies  
**University of Applied Sciences and Arts of Southern Switzerland**  
**Thesis** Mechanical characterization of reticulated porous ceramics under flexural loading.
- 2005-2010** B.Sc. in Mechanical Engineering  
**Isfahan University of Technology (IUT), Iran**  
**Thesis** Design and optimization of FOA compliant centrifugal clutches using Abaqus CAE.

***Journal PUBLICATIONS***

---

- E. Rezaei, M. Barbato, S. Gianella, A. Ortona, and S. Haussener, “Pressure drop and convective heat transfer in SiSiC structures fabricated by additive manufacturing and replication”, in revision, Sep. 2019.
- E. Rezaei, M. Barbato, A. Ortona, and S. Haussener, “Design and optimization of a high-temperature latent heat storage unit”, submitted, Sep. 2019.
- E. Rezaei, S. Haussener, S. Gianella, and A. Ortona, “Early-stage oxidation behavior at high temperatures of SiSiC cellular architectures in a porous burner,” *Ceramics International*, vol. 42, no. 14, pp. 16255–16261, Nov. 2016.
- D. Y. S. Perraudin, S. R. Binder, E. Rezaei, A. Ortona, and S. Haussener, “Phase Change Material Systems for High Temperature Heat Storage,” *Chimia (Aarau)*, vol. 69, no. 12, pp. 780–783, 2015.
- A. Szczurek, A. Ortona, L. Ferrari, E. Rezaei, G. Medjahdi, V. Fierro, D. Bychanok, P. Kuzhir, and A. Celzard, “Carbon periodic cellular architectures,” *Carbon*, vol. 88, pp. 70–85, Jul. 2015.
- E. Rezaei, G. Bianchi, S. Gianella, and A. Ortona, “On the nonlinear mechanical behavior of macroporous cellular ceramics under bending,” *Journal of the European Ceramic Society*, vol. 34, no. 10, pp. 2133–2141, Sep. 2014.